DEPARTMENT OF PHYSICS
UNIVERSITY OF JYVÄSKYLÄ
RESEARCH REPORT No. 2/2015

DEVELOPMENT AND APPLICATIONS OF TRANSITION-EDGE SENSORS

BY
MIKKO PALOSAARI

Academic Dissertation
for the Degree of
Doctor of Philosophy

To be presented, by permission of the
Faculty of Mathematics and Natural Sciences
of the University of Jyväskylä,
for public examination in Auditorium FYS-1 of the
University of Jyväskylä on April 17, 2015
at 12 o'clock noon

Jyväskylä, Finland
April 2015

Preface

The work presented in this thesis has been carried out at the Department of Physics in the Nanoscience Center and in the Accelerator Laboratory at the University of Jyväskylä.

I'm deeply grateful to my supervisor Prof. Ilari Maasilta for guiding me through the whole process of making a doctoral thesis. Numerous discussions about measurements and especially the theory side of things has made this thesis possible. Second, I would like to thank Dr. Kimmo Kinnunen for introducing me to the world of cryogenics, microfabrication, and transition-edge sensors. His tremendous know-how and expertise in everyday measurements has had a big impact on the work presented in this thesis. Third I would like to thank Prof. Timo Sajavaara for adopting me as a part of his research group and for his guidance that got me into accelerator based science.

I would like to thank the past and present staff at the Nanoscience Center for making it a great working place. Mr. Tarmo Suppula has also been a big help in the technical issues that always arise in experimental physics. I want to thank the accelerator based material science group, especially Dr. Mikko Laitinen and Mr. Jaakko Julin for operating the beam during measurements and Mr. Marko Käyhkö for participating in the measurements and in the analysis. A special thanks goes to my old office buddies Dr. Veikko Linko, Dr. Ville Kotimäki and Dr. Olli Herranen for keeping the atmosphere in the office perfect through the times spent at the YN251.

I would like to thank the people that we have collaborated with. People at NIST Boulder, most importantly Dr. Randy Doriese and Dr. Joel Ullom, for discussions and guidance, and for hosting me during my visit to Boulder. People at VTT, Mr. Leif Grönberg, Dr. David Gunnarsson and Dr. Mika Prunnila.

I want to thank my parents for supporting me with my goals, although I didn't become an airplane pilot. Most importantly, I want to thank the love of my life, my wife Suvi, for the support and patience that she's given me through out the years. I would also like to mention my children Saara and Santeri who have not contributed to the work done in this thesis at all, but instead they have given me motivation, joy and love.

Jyväskylä, April 2015
Mikko Palosaari

Abstract

Palosaari, Mikko
Development and Applications of Transition-Edge Sensors
Jyväskylä: University of Jyväskylä, 2015
Department of Physics Research Report No. 2/2015
ISBN paper copy: 978-951-39-6160-2
ISBN PDF: 978-951-39-6160-2
ISSN: 0075-465X

This thesis focuses on the theory, development and applications of Transition-Edge Sensor (TES) arrays. The main results are the design and development of a fabrication process for a 256 pixel X-ray TES detector with a novel geometry and the development of a measurement setup for TES detectors used in elemental analysis with Particle Induced X-ray Emission (PIXE) measurements.

In the early stages of this thesis we fabricated a small scale 32 pixel TES array, but for an actual application purposes the pixel count and the consistency of the fabrication needs to be higher. The cleanroom facilities in the Nanoscience Center are well suited for basic research but they are not suitable for a wafer scale processing. To make the fabrication of a large scale TES array possible we collaborated with VTT (Technical Research Centre of Finland) and used their Micronova clean room facilities for the fabrication of the detectors.

We've shown a setup consisting of 12 pixels being used in a PIXE measurement with the best pixel having a remarkable 3.06 eV energy resolution at 5.9 keV. This kind of resolution has not been reported before for a wide band energy dispersive detector used in a PIXE system. The thesis will also show experiments done with an updated measurement system capable of analyzing the elemental contents of thin film samples with 60 pixels. Also the energy efficiency of the setup is reported.

Keywords Transition-Edge Sensor, X-ray detector, Particle Induced X-ray Emission

Author's address Mikko Palosaari
Department of Physics
Nanoscience Center
University of Jyväskylä
Finland

Supervisor Professor Ilari Maasilta
Department of Physics
Nanoscience Center
University of Jyväskylä
Finland

Reviewers Dr. Luciano Gottardi
SRON Netherlands Institute for Space Research
Utrecht
The Netherlands

Dr. Juha Hassel
Technical Research Centre of Finland
VTT
Finland

Opponent Dr. Michael Rabin
Los Alamos National Laboratory
Los Alamos, New Mexico
USA

List of Publications

This thesis is based on the work contained within the following publications:

A.I. M. R. J. Palosaari, K. M. Kinnunen, M. L. Ridder, J. van der Kuur, H. F. C. Hoevers and I. J. Maasilta, *Analysis of Impedance and Noise Data of an X-ray Transition-Edge Sensor Using Complex Thermal Models.* J. Low Temp. Phys. **167**, 129-134 (2012).

A.II. M. R. J. Palosaari, K. M. Kinnunen, J. Julin, M. Laitinen, M. Napari, T. Sajavaara, W. B. Doriese, J. Fowler, C. Reintsema, D. Swetz, D. Schmidt, J. Ullom and I. J. Maasilta, *Transition-Edge Sensors for Particle Induced X–ray Emission Measurements.* J. Low Temp. Phys. **176**, 285-290 (2014).

A.III. M. R. J. Palosaari, L. Grönberg, K. M. Kinnunen, D. Gunnarsson, M. Prunnila and I. J. Maasilta, *Large 256 Pixel X-ray Transition-Edge Sensor Arrays with Mo/TiW/Cu Trilayers.* IEEE Trans. Appl. Supercond. **25**, 3, 1–4 (2014).

A.IV. M. R. J. Palosaari, K. M. Kinnunen, J. Julin, M. Laitinen, J. Malm, T. Sajavaara, W. B. Doriese, J. Fowler, C. Reintsema, D. Swetz, D. Schmidt, J. Ullom and I. J. Maasilta, *Wide-Energy-Range High-Resolution Particle Induced X-ray Emission Spectroscopy with Superconducting Microcalorimeter Arrays.* Manuscript

Other publications to which the author has contributed

B.I. K. M. Kinnunen, M. R. J. Palosaari and I. J. Maasilta, *Normal Metal – Superconductor Decoupling As a Source of Thermal Fluctuation Noise in Transition-Edge Sensors*. J. Appl. Phys. **112**, 034515 (2012).

B.II. K. M. Kinnunen, M. R. J. Palosaari and I. J. Maasilta, *Effect of a Thin AlOx Layer on Transition-Edge Sensor Properties*. J. Low Temp. Phys. **167**, 141-145 (2012).

Author's contribution

The author of this thesis has written articles A.II and A.IV. The author participated in writing A.I, and A.III. The author had a contribution in characterizing the samples for A.I and analyzed the data. The author has participated in the development of the setup used in A.II and A.IV and the author conducted the measurements. The data analysis in A.II was done by the author and partially in A.IV. The author participated in designing of the detector array in A.III and did the measurements and the analysis. In B.I and B.II the author fabricated the samples and participated in the measurements.

Contents

Chapter 1

Introduction

In 1895 X-rays were discovered by Wilhelm Röntgen[1] [1], which awarded him the first ever Noble price in physics in 1901. X-rays are a powerful tool that have numerous applications. Thanks to their penetrating ability X-rays are used in medical industry and in security to see inside of objects. In X-ray crystallography the structural information, distances between atoms and the angles between bonds of a material, can be measured by analyzing how the material diffracts X-rays [2]. X-ray absorption spectroscopy is a structural method that allows one to investigate the neighborhood of a particular element embedded in a condensed medium [3].

Soon after the discovery of X-rays it became clear that the energy of X-rays are intimately related to the atomic structure of the element that emits them. Each element has its own characteristic X-ray spectrum, which is a fingerprint of the material. By measuring an X-ray spectrum from a sample the elemental content of it can be solved.

Characteristic X-rays of a material can be excited by photons or by particles, whose energy has to be high enough to ionize the target material. In 1913 Moseley measured the frequency of the characteristic X-rays of many elements by irradiating them with electrons and by interpreting the data he even found three new elements that were later added to the periodic table [4]. The main technique to excite X-rays used in the experiments of this thesis is Particle Induced X-ray Emission (PIXE), which was first demonstrated in 1970 by S. Johansson *et al.* [5]. In PIXE, accelerated proton or other light ion beam is used to ionize material to excite its characteristic X-rays. The technique is nowadays used in many fields including material science [6], medical diagnostics [7], geology [8], archeology [9] and art conservation [10]. These are fields, where the sensitivity of PIXE (parts per million in many cases), quantitative accuracy and a multielemental analysis run is needed. Typical research done with PIXE is trace element studies [11].

Superconductivity was discovered in 1911, when H. Kamerlingh Onnes measured the sudden total vanishing of electrical resistance in mercury when cooled

[1] in Finnish like in many other languages X-rays are still called *Röntgen rays.*

below liquid helium temperatures [12]. This discovery and the advances he made in cryogenics earned him the Nobel prize in physics in 1913. Another trademark feature of superconductivity is the expulsion of magnetic field from a superconductor making them perfect diamagnets [13] (Fig. 1.1).

Figure 1.1: A permanent magnet levitating on top of a superconductor, the Meissner effect.

To measure X-rays one needs a detector. The main topic of this thesis is the Transition-Edge Sensor (TES), which is an extremely sensitive energy dispersive detector that is operated at temperatures near absolute zero. The TES utilizes the sharp transition between the normal and the superconducting state. The device is biased between the two states, and when a photon hits the detector it warms up the device and the resistance of it changes. From the resistance change the energy of the incident photon can be deduced.

A TES was first demonstrated in 1941, when a tantalum wire was operated in its superconducting transition and the increase of resistance caused by infrared signal was measured [14]. It took more than 50 years for the read out technology to mature enough so that TES devices could be effectively used in applications. The TES can be used as a bolometer, where the power of the radiation is measured or as a microcalorimeter, where the energy of the individual photons are measured. This thesis focuses on the latter.

Nowadays TES devices are used in numerous experiments. TESs are used in search for evidence of the inflationary gravitational waves [15],[16],[17], addressing key questions relating to the origins of galaxies [18], in energy dispersive X-ray microanalysis [19], in quantum information research [20], in nuclear materials characterization [21], in neutrino mass detection [22] and in X-ray absorption spectroscopy [23] to name a few.

In this thesis the development of a large scale 256 pixel TES X-ray detector array and the characterization of the detectors will be covered. Another focus point is the applications, mainly PIXE measurements done with TES detectors.

Chapter 2

Microcalorimeters

2.1 Transition-Edge Sensor 101

Transition-edge sensor is a type of microcalorimeter that can be tailored to measure photon energies from the near infrared to γ-rays [24]. In its heart there is a superconducting thin film that is biased between the superconducting state and the normal state. The superconducting film is connected to an absorber with a heat capacity C, where the energy of the incident photon is deposited. The absorber is connected to a heat sink with a weak thermal link that has thermal conductance G (Fig. 2.1).

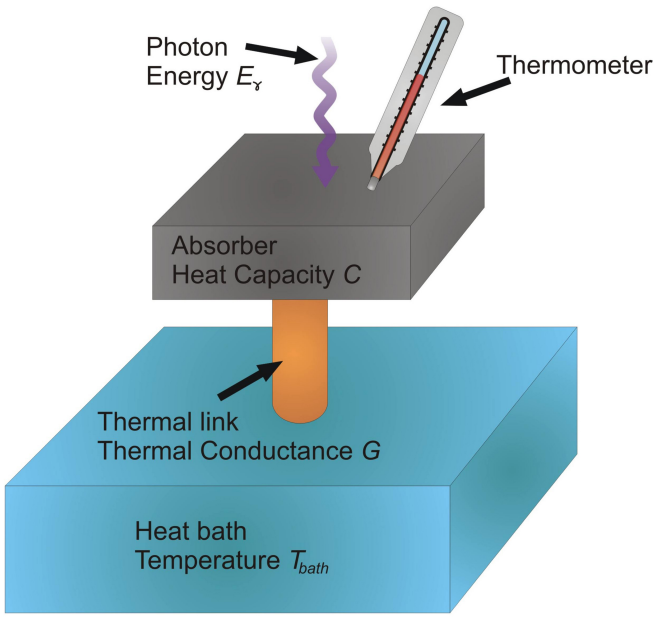

Figure 2.1: Schematics of a microcalorimeter.

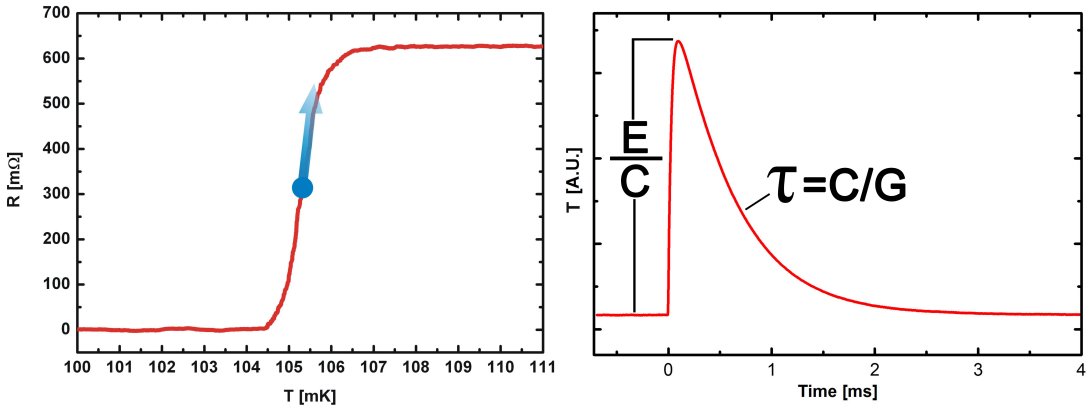

Figure 2.2: Left: The transition. Right: The pulse.

When a photon with an energy E hits the detector, the temperature of the TES will rise by $\Delta T = E/C$, after which it will cool back to the steady state temperature with a natural time constant $\tau = C/G$ if no electrothermal feedback is present [25]. In the case of a TES the change in the absorbers temperature is measured with the very steep resistance vs. temperature $R_{TES}(T)$ behavior of the superconducting film operated at the transition.

The transition between the superconducting and the normal state is described with the temperature sensitivity parameter

$$\alpha = \frac{\partial \log R_{TES}}{\partial \log T}, \tag{2.1}$$

and the current sensitivity parameter

$$\beta = \frac{\partial \log R_{TES}}{\partial \log I}. \tag{2.2}$$

In a small signal limit the resistance of a TES can be written as

$$R_{TES}(T, I) \approx R_0 + \alpha \frac{R_0}{T_0}\delta T + \beta \frac{R_0}{I_0}\delta I, \tag{2.3}$$

where R_0, I_0 and T_0 are the steady state TES resistance, current and temperature respectively. The α of a TES can be two orders of magnitude higher than with a semiconductor thermistor thermometers [24].

With a constant power P_{in} applied, the temperature of the TES detector will rise above the bath temperature T_{bath} until the power flowing into the detector equals the out flowing power P_{out} to the heat bath. In general a thermal equation can be used to describe the system [26]

$$C\frac{\mathrm{d}T(t)}{\mathrm{d}t} = -P_{out} + P_J + P_{in}, \tag{2.4}$$

where P_J is the Joule heating power. Let's assume the P_{out} has the form

$$P_{out} = K(T^n - T^n_{bath}). \tag{2.5}$$

The differential thermal conductance is defined as

$$G = \frac{\mathrm{d}P_{out}}{\mathrm{d}T} = nKT^{n-1}. \tag{2.6}$$

The bias circuit for a TES and it's Thevenin equivalent circuit [27] are depicted in Fig. 2.3 and its electrical differential equation is

$$L\frac{\mathrm{d}I}{\mathrm{d}t} = V_{TH} - I_{TES}R_L - I_{TES}R_{TES}(T, I). \tag{2.7}$$

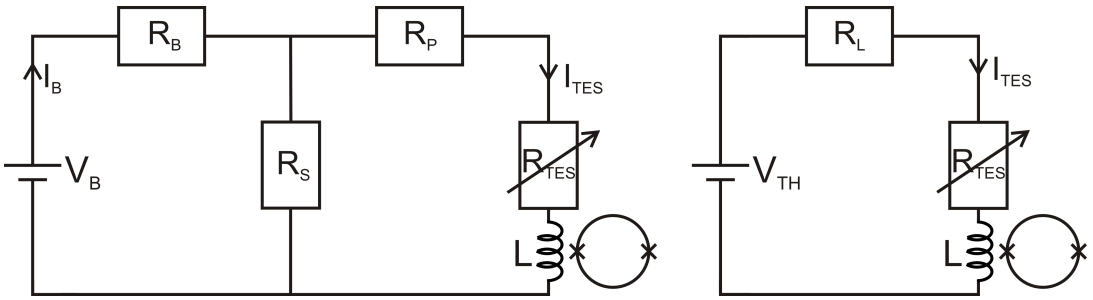

Figure 2.3: Left: Voltage bias circuit for a TES. R_B is the front resistor, R_S the shunt resistor and R_P is the parasitic resistance of the circuit. L is the inductance of the circuit to couple the current change through the TES to a Superconducting QUantum Interference Device (SQUID, see Section 4.3). For the circuit to work as a voltage bias $R_S < R_{TES} << R_B$. Right: the Thevenin equivalent of the circuit, where $R_L = R_S + R_P$ and $V_{TH} = V_B R_S/R_B$

Solving the two connected linear equations 2.4 and 2.7 will give the current response of a TES. The derivation will be skipped here as it has been done by many authors [24], [26], [28], [29]. The power to current responsivity is then defined as

$$s_I(\omega) = \frac{\mathrm{d}I}{\mathrm{d}P}. \tag{2.8}$$

Negative Electrothermal feedback (ETF) is a way to make the operation of a TES more stable and to impose its characteristics. It was first proposed by Irwin [28] and it's achieved by voltage biasing the TES. When the detector is voltage biased the Joule heating keeps the TES in its transition. With a constant voltage the Joule power is

$$P_J(T) = \frac{V^2}{R_{TES}(T)}. \tag{2.9}$$

When the TES is in the transition a temperature increase will cause a resistance increase decreasing the heating power, which then cools down the TES. This effect is the negative ETF. Besides stability, the ETF *e.g.* shortens the duration of pulses, which increases the possible count rates [26]. With ETF the effective thermal time constant is

$$\tau_{eff} = \tau \frac{1+\beta}{1+\beta+\mathscr{L}}, \tag{2.10}$$

where

$$\mathscr{L} = \frac{\alpha I_0^2 R_0}{G T_0}, \tag{2.11}$$

is the loop gain.

2.1.1 Complex impedance

By measuring response of the detectors to voltage signals applied to the bias line, the complex impedance can be measured as a function of frequency [24]. The complex impedance is a useful tool to examine the circuit parameters of a TES [30].

The Thevenin equivalent circuit in Fig. 2.3 has a frequency dependent complex impedance

$$Z_{circ}(\omega) = Z_{TES} + R_L + i\omega L. \tag{2.12}$$

In the case of the simple block model (Fig. 2.1) the TES impedance is [24]

$$Z_{TES}(\omega) = R_0(1+\beta) + \frac{R_0\mathscr{L}}{1-\mathscr{L}} \frac{2+\beta}{1+i\omega\tau_I}, \tag{2.13}$$

where $\tau_I = \tau/(1-\mathscr{L})$. By measuring the complex impedance, parameters such as β, $\mathscr{L}$, τ_I, L and C can be extracted.

2.1.2 Noise

Four noise sources are always present in a TES: the Johnson noise of the TES, Johnson noise of the resistors, amplifier noise and thermal fluctuation noise between the TES and the heat bath (phonon noise)[31]. The power spectral density of the current noise due to Johnson noise is [24]

$$S_{I_{TES}} = 4k_B T_0 R_0 \xi(I)(1+\omega^2\tau^2)|s_I(\omega)|^2/\mathscr{L}^2, \tag{2.14}$$

where $\xi(I) = 1 + 2\beta$ [32] and k_B is the Boltzmann constant. The thermal fluctuation current noise has power spectral density

$$S_{I_{ITFN}} = 4k_B T_0 G F(T_0, T_{bath})|s_I(\omega)|^2, \tag{2.15}$$

where $F(T_0, T_{bath})$ depends on the thermal link and typically has values between 0.5 and 1[24].

2.1.3 Energy Resolution

The energy resolution, ΔE, of a TES is the main attraction why one would want to use complex detectors operated near absolute zero. ΔE of 1.8 eV at 5.9 keV has been reported for a TES [33]. The full width at half maximum (FWHM) energy resolution of a TES detector is [24]

$$\Delta E_{FWHM} = 2\sqrt{2\ln 2}\left(\int_0^\infty \frac{4}{S_{P_{tot}}}(f)df\right)^{-1/2}, \tag{2.16}$$

where $S_{P_{tot}}$ is the total total power referred noise that includes all noise sources

$$S_{P_{tot}}(\omega) = \frac{S_{I_{tot}}(\omega)}{|s_I(\omega)|^2}. \tag{2.17}$$

In the case of strong electrothermal feedback ($\mathscr{L} >> 1$) and with no load resistance R_L, the energy resolution can be written as [24]

$$\Delta E_{FWHM} = 2\sqrt{2\ln 2}\sqrt{\frac{4k_b T_0 C}{\alpha}\sqrt{\frac{nF(T_0, T_{bath})}{1-(T_{bath}/T_0)^n}}}, \tag{2.18}$$

where *e.g.* in a ballistic case with the simple thermal model the term F depending on the thermal link becomes $F = 1/2[1+(T_{bath}/T_0)^{n+1}]$. From Equation 2.18 one can see that by operating the detectors in as low temperature as possible is beneficial in regards to the energy resolution. By having a C as small as possible and the α as large as possible enhances the energy resolution also. On the other hand the heat capacity and the sensitivity α set the saturation energy of the detectors, which is the upper limit for the photon energy that can be measured, and they behave inversely in the case of saturation energy compared to the energy resolution. For practical reasons the α can not be too high as too fast detectors are hard to read out and multiplex. For these reason the parameters need to be engineered for the particular application in hand mostly depending on the energy of interest.

2.2 Other Low Temperature Detectors

There exist many type of X-ray microcalorimeter low temperature detectors. Here a few major competitors for TESs are introduced.

2.2.1 Microwave Kinetic Inductance Detectors

Microwave kinetic inductance detectors (MKIDs) are Cooper pair breaking devices. In a superconductor the supercurrent is carried by bound electrons, known as Cooper pairs. The electrons are bound together with an energy $2\Delta \approx 3.5 k_b T_c$, where T_c is the critical temperature of the superconductor. A DC current flows in a superconductor with zero resistance but superconductors have a nonzero impedance for AC currents [34]. The Cooper pairs near the surface can be accelerated with an electromagnetic field. This energy can be stored in the form of kinetic energy. By reversing the field, this energy may be extracted. The overall effect is that a superconductor has a surface inductance due to the reactive energy flow between the superconductor and the electromagnetic field [35].

Photons with energy higher than 2Δ can break Cooper pairs into quasiparticles (Fig. 2.4). When the quasiparticle density in the superconductor changes, the surface impedance changes too. This change can be accurately measured using a thin film superconducting resonant circuit, resulting in a measurement of the energy and arrival time of the incident photon for the case of near-IR to X-ray photons (Fig. 2.5). Detectors designed for different wavelengths differ only in the way how the photon energy is coupled into the MKID. The detectors themselves and the readout are nearly identical [36].

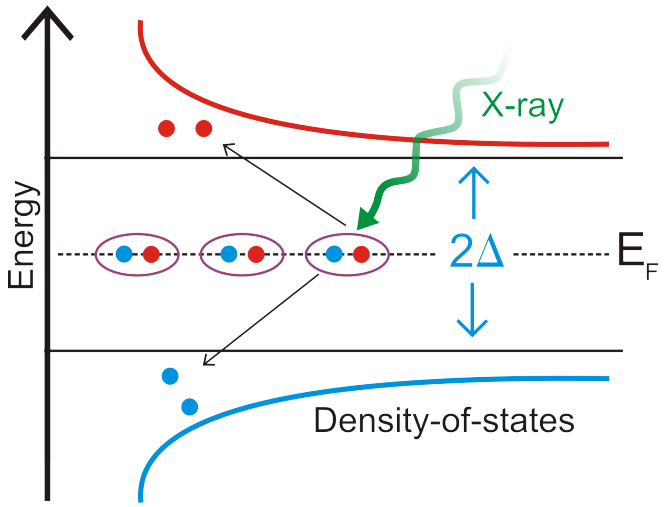

Figure 2.4: Photons with higher energy than the energy gap of the superconductor are absorbed in the superconducting film and thus breaking a Cooper pair.

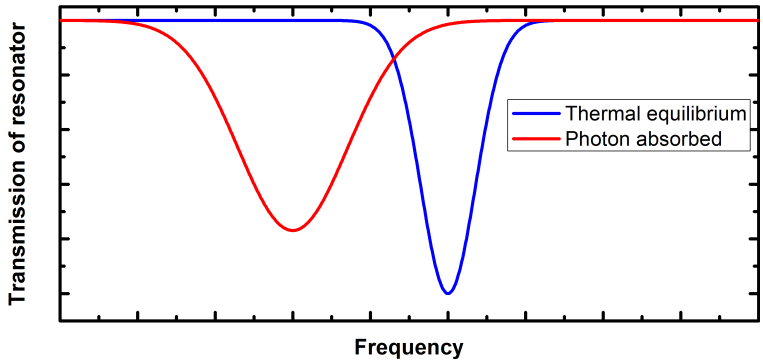

Figure 2.5: After a photon hits and changes the surface impedance of the device the resonance frequency shifts and the dip also gets shallower. From this the energy of the photon can be deduced.

The primary attraction of MKIDs is that they are easy to multiplex [37] so that large arrays are feasible. The resonance circuit with a high quality factor for each detector in an array can be easily be made such that every detector has its own resonance frequency. This way the whole array can be read simultaneously with out the need of time-division multiplexing, for example. Passive frequency domain multiplexing allows up to thousands of resonators to be read out through a single coaxial cable and a single low noise, high bandwidth cryogenic amplifier [38]. This simplifies the read-out tremendously compared to TES detectors. Also the structure of an MKID array is simpler compared to a TES and thus it's easier and cheaper to fabricate.

MKIDs are not on par with TESs energy resolution wise, though progress is being made. One issue that is poorly understood is the interaction of MKIDs with magnetic fields. MKIDs show significant frequency response to changes in the magnetic field normal to the metal surface. This can be a significant problem in some applications [36].

2.2.2 Superconducting Tunnel Junctions

The superconductor-insulator-superconductor sandwich structure of a Superconducting Tunnel Junction (STJ) detector is a Josephson junction [39]. Normally Al is used as the superconducting layer material and AlO_X as the insulating layer.

After the energy deposition at a certain position in either superconducting electrode forming the tunnel junction, quasiparticles created at that position diffuse, tunnel to the other electrode and possibly tunnel back, and finally recombine to form Cooper-pairs producing 2Δ phonons [40]. The number of quasiparticles is proportional to the energy of the absorbed photon. The number of quasiparticles is measured by measuring the amplitude of a current pulse caused by tunneling of quasiparticles through the tunnel barrier.

The optimum energy range for STJs is typically below few keV for a good energy-linearity with energy resolution of 8-16 eV [41].

2.2.3 Metallic Magnetic Calorimeters

The basic working principle of a Metallic Magnetic Calorimeter (MMC) is quite similar to a TES (Fig. 2.6). However, instead of measuring resistance change it measures the change in the magnetization of the detector caused by a temperature change due to absorbed photon. The sensing element is paramagnetic and usually Au with low concentration of Er is used [42]. The MMC is placed in an external field, and when a photon is absorbed the magnetization of the sensor is reduced. A SQUID is used to read out this change, which correspond to the energy of the photon. 2 eV at 5.9 keV energy resolution for MMCs have been reported [43].

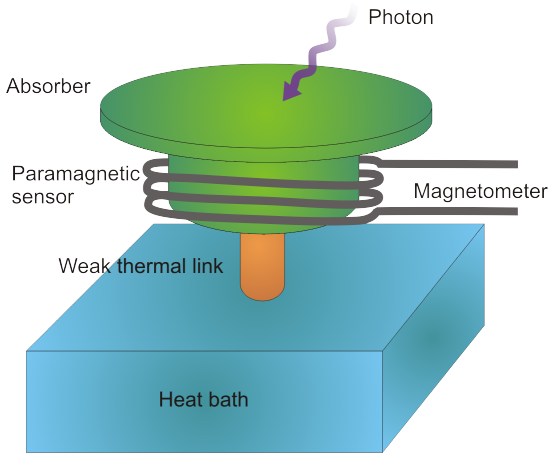

Figure 2.6: Schematics of a MMC.

Chapter 3

Complex Thermal Models

When one starts to analyze characteristics of a TES, it can happen that the simple one block model is not sufficient to describe the behavior of it. The simplest thermal model lumps together all the thermal masses of the detector into one. It's often too simple and it does not necessarily describe the measured noise or complex impedance (Fig. 3.1.

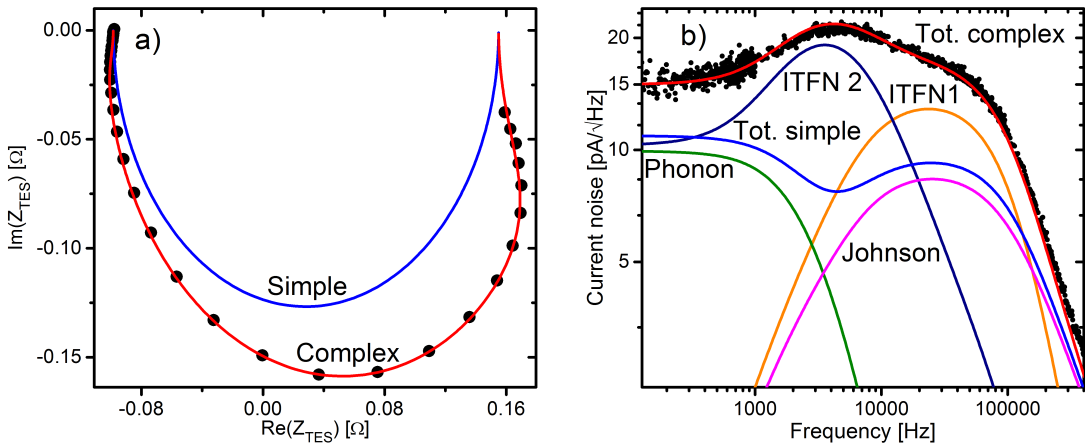

Figure 3.1: a) The measured (black dots) and fitted complex impedance with a simple and a complex thermal model. b) The measured (black dots) and fitted current noise with a simple and a complex thermal model. Also the individual noise sources are plotted. The simple noise total consist of the Johnson, SQUID, shunt and phonon noise. The complex total consists of additional two internal thermal fluctuation noise sources. From article B.I.

The theoretical thermal model of the detector needs to be expanded. The straightforward way is to divide the one lump of mass into more parts connected together thermally. When the device consists of several blocks of heat capacity there will be more thermal fluctuation noise [44]. It has turned out that a model with one additional thermal block is insufficient to fully fit measured noise and impedance data in some detectors [45], [46].

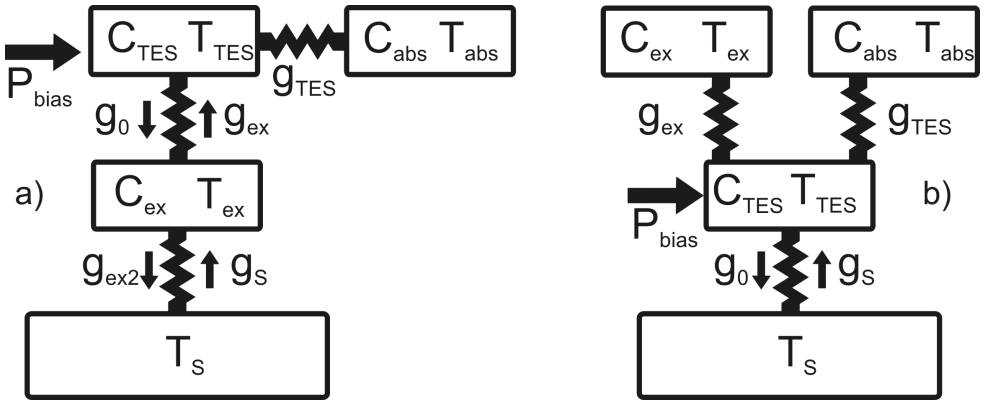

Figure 3.2: a) A model with one hanging and an intermediate block between the TES and the bath (IH model). b) A model with two hanging thermal blocks (2H model). From article A.I.

By using three thermal blocks (Fig. 3.2) we have been able to explain both the measured noise and complex impedance data successfully (see Fig. 3.1). Adding additional bodies into the thermal model introduces new thermal fluctuation noise sources to the system. The noise arising from these internal bodies are referred to as internal thermal fluctuation noise (ITFN). ITFN1 noise plotted in the Fig. 3.1 is caused by the thermal mass C_{ABS} and the ITFN2 by the thermal mass C_{EX}, when using the IH model in Fig. 3.2. Thermal conductance between different bodies can be via electron or phonon system. With these three block thermal models we usually don't need to include the M-parameter for the excess noise [47]. More detailed information about different noise mechanisms and modeling of them can be found for example in K. Kinnunen's thesis [31] and in the article B.I. Derivation of the responsivity and the complex impedance for the models expressed in Fig. 3.2 has been analytically done by I. Maasilta [48]. In articles A.I. and A.III. the modeling is done with these complex thermal models.

Naturally, the additional blocks need to have a physical origin to make the use of more complex models justifiable. We have seen evidence that two of the heat capacities are actually the superconducting and the normal phase of the TES decoupling thermally at the transition and fluctuations in the energy exchanged between thermal bodies is observed as a thermal fluctuation noise, which is discussed in article B.I.

In article A.I. we studied the complex impedance and the noise characteristics of a TES pixel from an X-ray array fabricated at Netherlands Institute for Space Research (SRON). The device had a 1 μm thick Cu absorber, which was coupled to the Ti/Au bilayer through seven rectangular vias. The device had a normal state resistance of about 300 mΩ and a critical temperature of 125.5 mK.

The measured data could not be fitted with a two block model but a three block model was needed in order to fit the complex impedance and the noise

simultaneously without the use of M-parameter as can be seen in Fig. 3.3. The

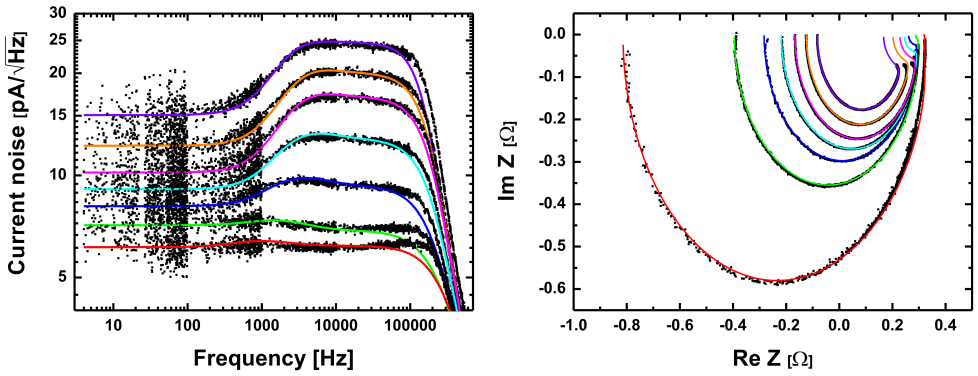

Figure 3.3: Left: the measured and fitted current noise of the device. Right: the measured and fitted complex impedance of the TES. Bias points between 20% – 80% of the normal state resistance in 10% intervals are presented. The higher bias points correspond to the lower noise levels and bigger semicircles. The model used in the analysis was the IH model shown in Fig. 3.2. The 2H fits look identical.

heat capacities and the thermal conductances used as free parameters in the fittings are plotted in Fig. 3.4 as well as the α and β as a function of the bias point.

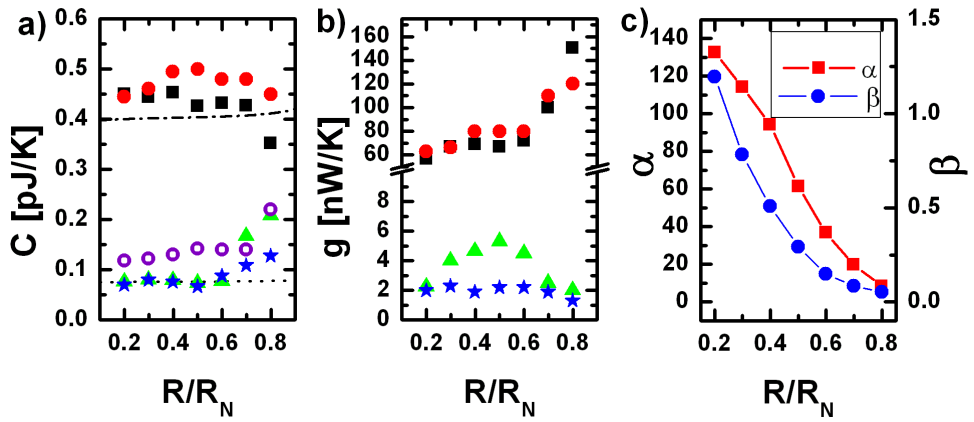

Figure 3.4: Some of the parameters from both IH and 2H models vs. bias point. a) C_{TES} (IH triangles, 2H stars), C_{ABS} (IH squares, 2H circles) and C_{EX} (IH open circles) and the estimated theoretical values as dashed lines. b) g_{TES} (IH squares, 2H circles), g_0 (IH triangles) and g_{Ex} (2H stars). c) α and β.

Chapter 4

Experimental Methods

4.1 ^{3}He-^{4}He Dilution Refrigerator

^{3}He-^{4}He dilution refrigerator works on the principle of phase separation between the two isotopes at low enough temperatures [49] and it was first proposed in 1962 [50]. ^{3}He-^{4}He dilution refrigerator is the only continuous refrigeration method for temperatures below 0.3 K [51].

Below 0.87 K the two phases separate to a normal fluid rich in ^{3}He on top of a superfluid phase rich in ^{4}He. With a controlled cycle of mixing, diffusion, and condensing the mixture cools beyond the temperature of the surrounding bath, which is usually a liquid He at 4.2 K. When ^{3}He atoms are pumped away from the dilute phase ^{3}He atoms re-enter the dilute phase from the concentrated phase through the phase boundary. Cooling will result according to the enthalpy difference of the two phases [51]. The schematics of a dilution refrigerator is shown in Fig. 4.1.

^{3}He gas coming from room temperature is precooled by the liquid He bath at 4.2 K. Then, it is condensed at the pot, to which liquid ^{4}He flows through a siphon from the surrounding He bath, cooling it to about 1.5 K. Below this ^{4}He refrigerator, a main flow impedance is needed to establish sufficient pressure to condense the incoming ^{3}He gas. Next the ^{3}He gas will flow through heat exchangers that are in thermal contact with the still at 0.7 K. Below the still there can be a secondary impedance to prevent re-evaporation of ^{3}He. After flowing through heat exchangers to precool the He liquid it enters the upper, concentrated phase in the mixing chamber. A wider tube for the dilute phase in the refrigerator leaves the lower dilute mixture phase of the mixing chamber, and through the heat exchanger to precool the incoming ^{3}He. Then it enters the dilute liquid phase in the still. Vapor above the liquid phase in the still has concentration of about 90 % of ^{3}He. Now, if the still is pumped and the condensation line is resupplied continuously with ^{3}He gas a closed ^{3}He circuit is formed where ^{3}He is forced down the condensation line. By continuously pumping the closed circuit from the still the ^{3}He will eventually cross the phase boundary and by doing so it will cool down the system. State of the art dilution

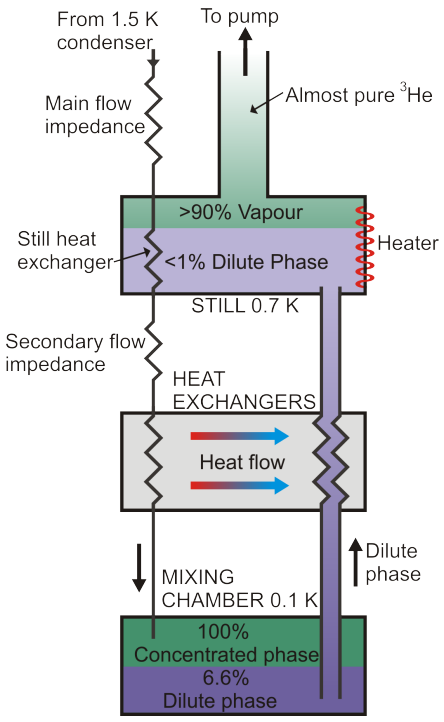

Figure 4.1: Schematical image of a dilution refrigerator.

refrigerators can reach temperatures below 2 mK [52].

4.2 Adiabatic Demagnetization Refrigerator

In 1926 P. Debye [53] and W. F. Giauque [54] proposed independently that the magnetic disorder entropy of electronic magnetic moments in paramagnetic salts could be used for cryogenic cooling. A decade later a group in Berkeley reached 0.53 K with the method and little later a group in Leiden reached 0.27 K. Nowadays this technique can be applied to experiments in the temperature range from 2 mK to 1 K.

After the 1950s the ADR technique was replaced by the continuous ^{3}He-^{4}He dilution refrigeration. Nowadays thanks to their cryogen free nature due to pulse-tube precooling, the ADR devices have again gained ground in research.

In the heart of the ADR cryostat is the paramagnetic salt pill. When the temperature is decreased, the interactions between the magnetic moments become comparable to the thermal energy (k_bT) which causes spontaneous magnetic ordering and lowering of the entropy. An external magnetic field will interact with the magnetic moments orienting them to form a magnetic state of higher order. So, when an external magnetic field is applied the entropy of the system will decrease at a higher temperature than without the field.

In Fig. 4.2 the entropy curve as a function of temperature during a mag-

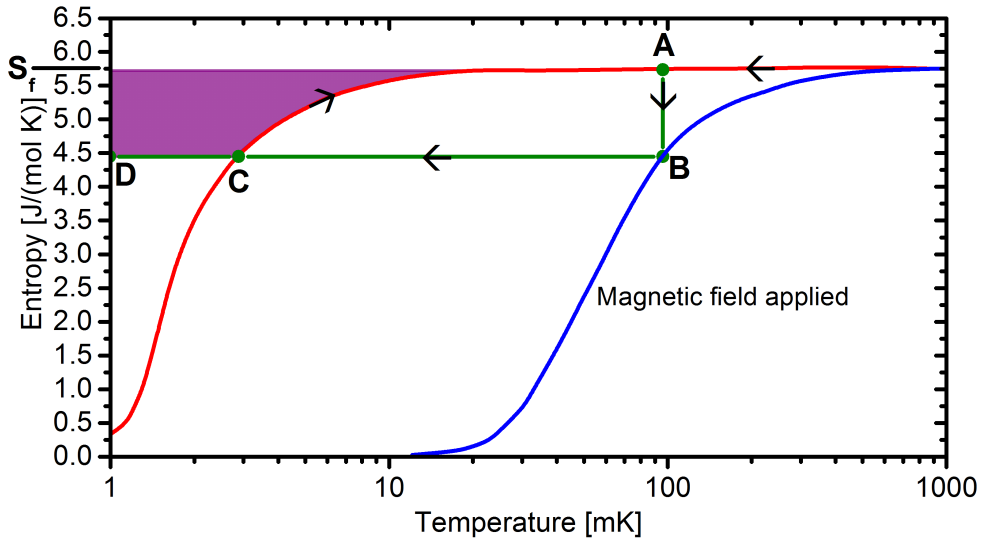

Figure 4.2: Entropy as a function of temperature during a magnet cycle. Graph based on [51].

netic cycle is shown. In the refrigeration process the salt is first isothermally (meaning that the temperature stays constant) magnetized (AB). Next the salt is thermally isolated and it's adiabatically demagnetized (BC) leading to cooling. Eventually the salt will warm up along the red entropy curve at the final demagnetization field. The rectangle $ABDS_F$ is the heat of magnetization during the magnetization and the cooling energy of the salt after demagnetization is given by the purple area.

The properties of the ADR are mainly determined by the initial starting conditions (temperature and the applied magnetic field), heat leaks and the properties of the paramagnetic salt [51]. The salt should have a low magnetic ordering temperature and a large magnetic specific heat in order to achieve a large cooling power. The paramagnetic salts suitable for magnetic cooling must contain ions with only partly filled electronic shells meaning either 3d transition elements or 4f rare earth elements. One example of a salt used is the FAA ($Fe_2^{3+}(SO_4)_3 \cdot (NH_4)_2SO_4 \cdot 24H_2O$).

4.3 Superconducting QUantum Interference Device

In 1969 the magnetic field of a human heart was measured with a SQUID [55]. Since then the device has found numerous applications, where the detection of very weak magnetic fields is needed. SQUID is a device that utilizes flux quantization [56], [57] in a closed loop with Josephson junctions [39] and combines the two phenomena [58]. The flux contained in a superconducting loop is a multiple

of the flux quanta $\Phi_0 = \frac{h}{2e}$, where h is the Planck constant and e is the electrons charge. The quantization of the flux arises because the macroscopic wavefunction needs to be single valued going around the loop. Josephson current is a tunneling current between two superconductors that have been separated with an insulator or a metal [58]. The current across the junction is $I = I_0 \sin \delta$, where δ is the phase difference between the two superconductors and I_0 is the critical current. When a bias voltage U is applied over the junction the phase evolves as $\frac{d\delta}{dt} = \frac{2\pi U}{\Phi_0}$.

In the early days of TES development the sensor were read out with a FET amplifiers [24]. The difficulty was matching the noise of low impedance TES to the FETs. Cross-correlation circuits [59], step-up transformers [60] and resistive meander lines [61] were used to try to solve the issue, but switching from FETs to SQUIDs to read out the TES eliminated this problem. SQUIDs are sensitive enough to measure fields as low as $5 \cdot 10^{-18}$ T with a few days of averaging [62] (Earth's magnetic field is about 40 μT [63]).

A SQUID current amplifier consists of a SQUID and an input coil which converts an applied current to a magnetic flux, which in turn causes the SQUID voltage output to vary. Due to the nonlinear response of the SQUID it is usually linearized by applying a feedback flux [64]. When a SQUID current amplifier is used to read out the change in the current through a TES array consisting of many devices, the number of wires running to room temperature needs to be minimized. This can be done by connecting the outputs of many SQUIDs in series and turning the SQUIDS on one at a time. This is called time division multiplexing (TDM). TDM has been demonstrated with over 10000 pixels for bolometers [65], where instead of energy quanta the power of radiation is measured. For calorimeters such high pixel number is not yet feasible for multiplexing because of the faster current changes [66]. Other types of multiplexing methods are code division multiplexing [67],[68] and frequency domain multiplexing [69]. SQUIDs are well suited for reading out TESs thanks to their low noise, low power dissipation, and low input impedance [70].

4.4 Particle Induced X-ray Emission

Particle Induced X-ray Emission (PIXE) is a method of determining the elemental composition of a material. The basic principle behind PIXE is to knock off inner shell electrons from a material by irradiating it with particles, usually 2–3 MeV protons. This energy range is used because the X-ray production has maximum cross section at about 3 MeV. When an outer shell electron relaxes back to fill the void a characteristic X-ray photon of the given element is emitted (Fig. 4.3).

Due to the fact that the electron shell structure is unique for every element the resulting spectrum will give information about what elements the radiating material consists of [71].

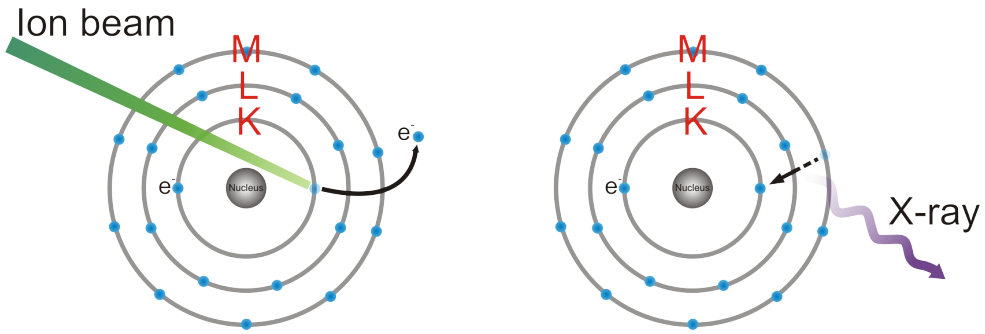

Figure 4.3: Basic principle of PIXE.

Some X-ray transitions between different shells are labeled In Fig. 4.4.

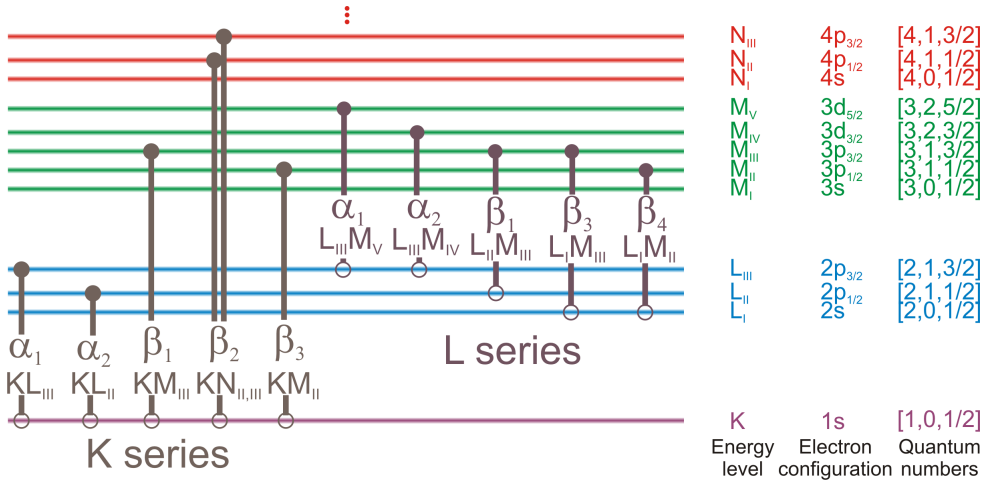

Figure 4.4: Some of the energy levels and X-ray transitions in medium-heavy element. The Siegbahn and the corresponding International Union of Pure and Applied Chemistry (IUPAC) notation [72] are labeled for the transitions as well as the naming of the levels by energy level, electron configuration and quantum numbers [n,l,j].

There are some transitions that have a very low probability although they are energetically possible, such as from L_1 to K shell, due to quantum mechanical rules involving the angular momentum properties between the two states [73].

The most common case in PIXE analysis is the determination of trace elements in a matrix of light elements. The highest sensitivity for detecting elements is obtained at rather low proton energies (2–3 MeV) as can be seen in the contour plot in Fig. 4.5. This means that relatively low cost and small accelerators are suitable for PIXE. From Fig. 4.5 it can also be seen that the elements with atomic number between 20–40 and over 75 have the highest sensitivity, which coincidentally are the elements that are usually most interesting in many

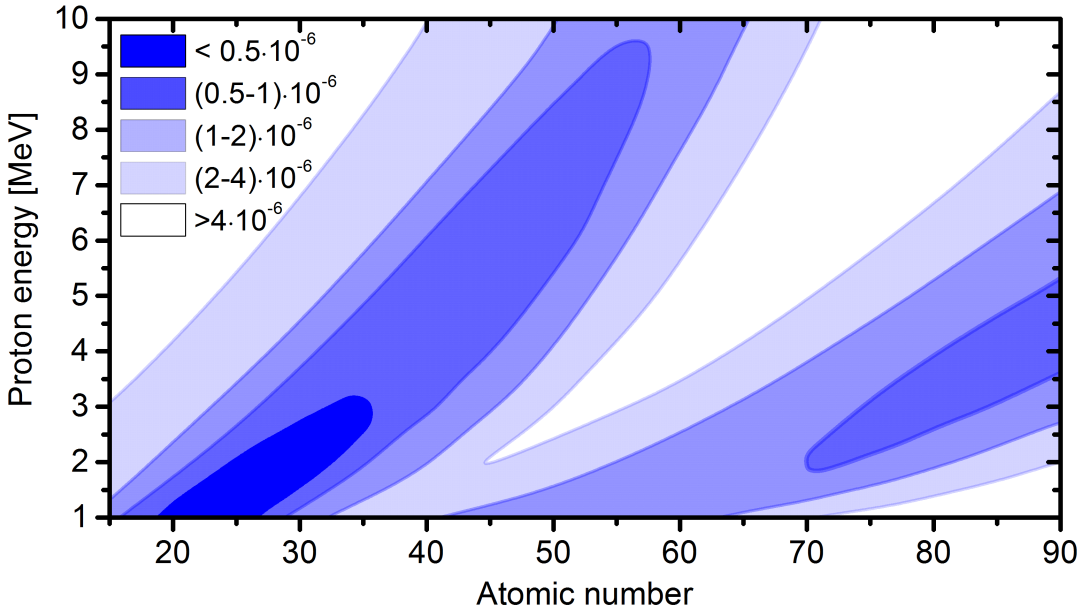

Figure 4.5: Minimum detectable concentration as a function of atomic number and proton energy in a typical PIXE arrangement. Adapted from Ref. [71].

analytical applications [71].

Use of heavy ions like ^{12}C, ^{16}O or ^{28}Si can limit PIXE analysis, because the interaction of heavy charged particles can destroy the sample by sputtering. Also projectile X-rays, which are characteristic X-rays of the ion beam itself, are produced, which may interfere or overlap with the sample X-rays.

In Scanning Electron Microscope Energy-dispersive X-ray spectroscopy (SEM-EDX), where the sample X-rays are excited with electrons, the brehmsstrahlung from the deceleration of electrons results in greater background levels compared to PIXE. This of course limits how small quantities can be detected. In PIXE the brehmsstrahlung from protons is negligible as the amount of radiation emitted by a particle is proportional to the square of its deceleration[71]. This is because the proton electron mass ratio differs by a factor of 1836 and the Coulombic forces are the same. The main cause of background in PIXE produced spectrum is due to brehmsstrahlung from secondary electrons produced by the proton beam [71]. In X-ray Fluorescence (XRF) instead of protons X-rays are used to ionize sample material. Either radioactive sources or X-ray tubes are used as an exciter. The smallest detectable limits for PIXE have been shown to be as low as 0.02 ppm, where for the XRF the corresponding limits are 1-10 ppm [71].

Chapter 5

Large Scale X-ray Detector Array Development

5.1 Motivation

Low temperature detectors have sparked interest outside their original use in cosmology research, thanks to their excellent energy resolution and broad energy range. There have been only a handful of places in the world capable of making large arrays of over hundred pixels namely National Institute of Standards and Technology (NIST) Boulder, Jet Propulsion Lab, National Aeronautics and Space Administration (NASA) Goddard and SRON in the Netherlands. Then we added NSC/VTT to this list by making 256 pixel arrays.

Our group has been studying the physics of TES detectors for a decade. We've been interested in the noise properties of the detector and what is their physical origin. We've also developed an unconventional detector geometry, the so-called Corbino TES named after an Italian physicist Orso Mario Corbino who first used the geometry to observe the Hall effect-based magnetoresistance without the associated Hall voltage. We have studied extensively the responsivity and noise of these detectors [74]. In the Corbino geometry the supercurrent flows radially in the superconducting film, which means that there is no edge effects. This means that we don't need to use any normal metal edge banks, which is typical for a square design [75].

We have mostly been fabricating single pixel detectors with electron beam lithography (EBL) [76], which is discussed in articles B.I. and B.II. In Fig. 5.1 four samples are being loaded into an EBL machine. EBL is very versatile and flexible way of fabrication, but it's also a slow method compared to UV lithograhy (UVL) [77]. The smallest features in a TES detector is in the order of few micrometers so there really is no benefit of the superior line width resolution of the EBL compared to the UVL. One other drawback to EBL is that a TES detector array chip consisting of hundreds of pixels can easily cover over a 1 cm^2 of area and usually the working area of EBL exposure is smaller than few mm^2. This means that stitching of the different working areas has to be done

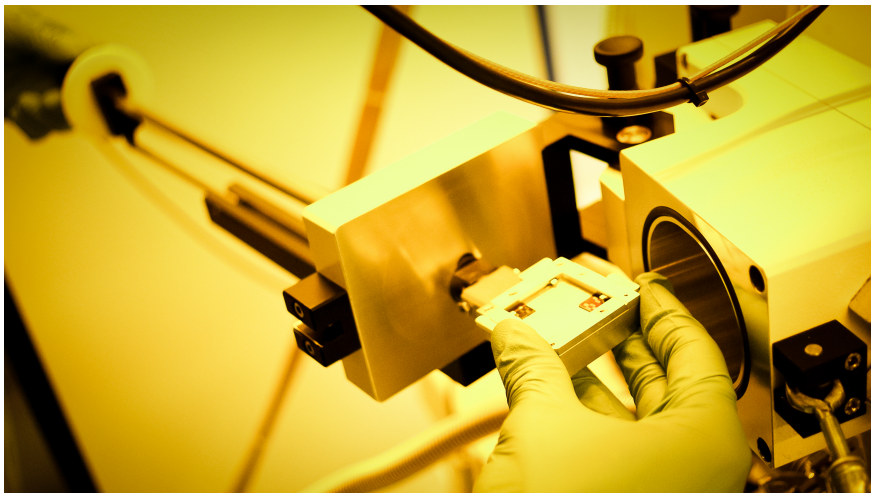

Figure 5.1: Samples being loaded into Raith E-line SEM.

very precisely so that *e.g.* long leads are continuous. When doing wafer scale processing and multiple chips at a time, the EBL method becomes unbearably slow and the stitching and aligning different pattern layers becomes very hard, if not impossible. Also, we can not fit anything bigger than few centimeters in diameter inside our EBL Scanning Electron Microscopes. So all in all UVL is much better suited for fabricating arrays of TES detectors.

Nevertheless, we have made a one prototype consisting of 32 Ti/Au square TES devices (Fig. 5.2). The critical temperature from halfway between the 10%

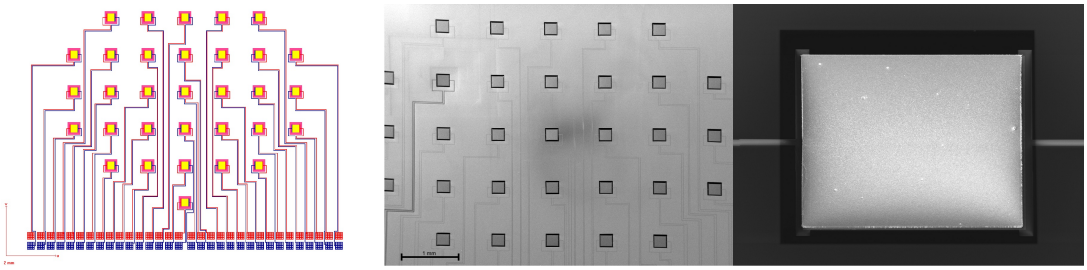

Figure 5.2: Left:CAD image of the array. Center: SEM image from the center of the array. Right: SEM image of one detector.

and 90% of normal state was T_C=(105.2±1.2) mK and the normal state resistance was R_N= (621.0 ± 4.8) mΩ, where the errors are the standard deviation of the data points. This tells that the especially the T_C spread across the chip was very small. A T_C spread of less than a few mK is needed in order to bias many detectors with the same voltage [66].

The fabrication was done with a Raith E-line electron microscope and with lift-off process. The materials were evaporated, and the Si_3N_4 membranes were

wet etched in KOH [78]. We evaporated a 2 μm Bi as the absorber material right on top of the superconducting bilayer with out any normal metals [75] or any mushroom shaped structure [33]. After the deposition of the Bi the T_C was lowered and also the transition steepness was decreased considerably.

As we do not have the UVL infrastructure to do wafer scale processing a joint project with VTT (Technical Research Centre of Finland) was started. The aim of the project was to fabricate TES arrays to be used in X-ray material analysis discussed more in Chapter 6. The main energy range of interest would be 1-15 keV. We also wanted optimize detectors capable of measuring harder X-rays upto 70 keV. We wanted to fabricate detectors with different heat capacities on a single wafer and with the Corbino design this can done by varying the radius of the absorber. The main results of the project are in article A.III.

5.2 Designing the Detector

First, we decided what materials we would be using in our detector array. We opted to chose molybdenum and copper as the superconducting thermal sensing element. This change from titanium and gold was done to lower the normal state resistance. A normal state resistance of less than 10 mΩ is needed in order to couple well with the NIST read out that is used in our measurement setup. The critical temperature of bulk Mo is 920 mK [79]. As the energy resolution of a TES scales down as a function of temperature [24] the T_C of the superconducting film should be as low as possible. On the other hand we have to cool down the detectors and the read out with reasonable cost so the typical critical temperature is engineered usually to around 100 mK. The critical temperature of a superconductor can be lowered with the so-called proximity effect [80], where a normal metal in contact with the superconductor lowers the T_C when the thickness of the superconducting film is less or of the same order of magnitude than the coherence length $\xi(T)$ [24].

The initial CAD designs are shown in Fig. 5.3. Some alterations were done later to better suit for etching processes *e.g.* overlaps between layers were optimized.

With the Corbino geometry, the resistance of the device can be tuned by changing the size of the inner or the outer contact. The circumference of the superconducting layer was kept the same as it's been with our previous single pixels devices – 320 μm. Three different size inner contacts were designed. This way we can fabricate three different normal state resistance devices with the same layer thickness.

The absorber material was chosen to be gold due to its thermal conductance and good stopping power. Thanks to the structure of the Corbino TES, there's no need for a mushroom like hanging structure, especially since we did not aim at 100% coverage of the chip area. The absorber sits on top of the detector with electrical contact only at the center. The rest is separated with a thin

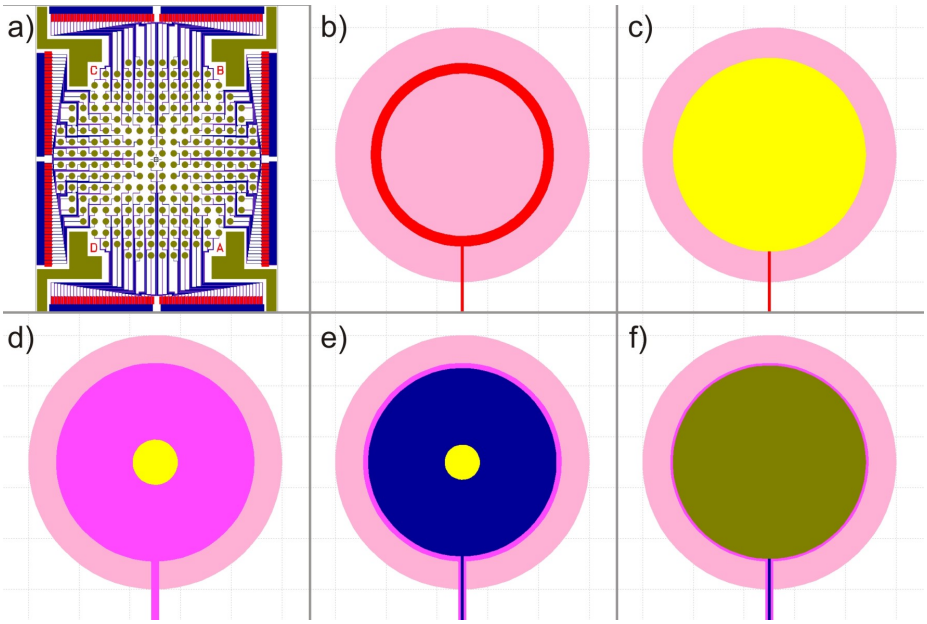

Figure 5.3: a) CAD image of a 256 pixel array. b) Outer Nb bias contact on Si_3N_4 membrane. c) Mo/Cu layer ϕ=320µm. d) Insulating SiO_2 layer. By changing the size of the inner hole the resistance of the device can be tuned. e) Inner Nb contact with a via for the absorber. f) Absorber covering the whole TES. By changing the diameter of the absorber the C can be tuned.

layer of insulator (SiO_2). Bismuth is used regularly as an absorber material by other groups. It's fairly heavy material and so it absorbs X-rays well. Being a semi-metal it has quite a low heat capacity due to low number of electrons. Bi was not available at VTT at this stage.

The lead material was selected to be Nb as it's a superconducting material with high a T_c of 9.5K for bulk material. This way there is no electrical losses in the leads.

5.2.1 Modeling of the Device

The absorption of X-rays for different thickness Au layers were calculated (Fig. 5.4). We see that by choosing Au thickness of 2 µm we can reach good stopping power up to 10 keV and even above.

A dummy square Ti/Au TES was also fabricated at the NSC on a Si_3N_4 membrane fabricated by VTT. The device was done so that the thermal conductivity of the membrane could be extracted. A square device was selected as it's easier to fabricate and the device was only fabricated to probe the thermal properties of the membrane. The Si_3N_4 membrane on Si frame would be the same as we would use on the actual array. A set of current-voltage (I-V) measurements were carried out in similar way as described in Section 5.4. The

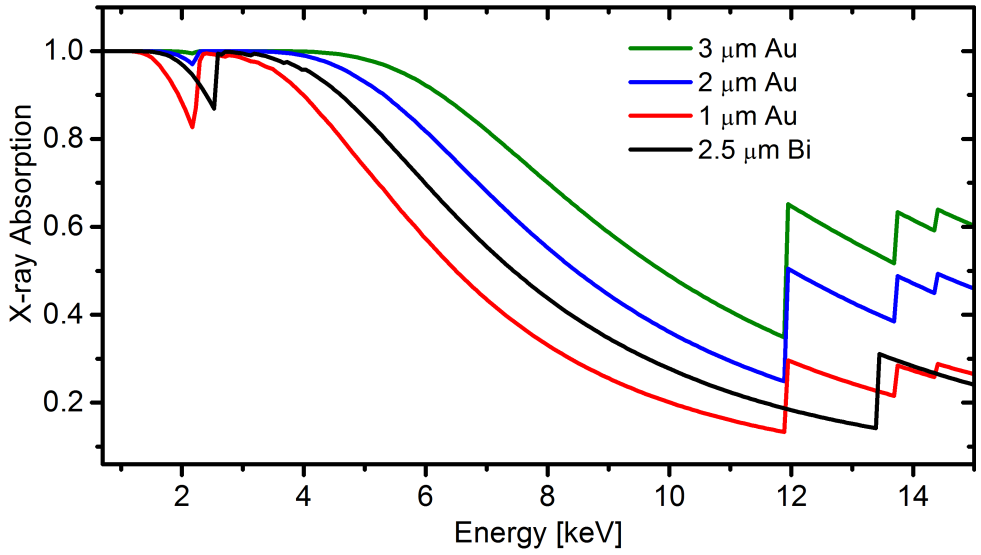

Figure 5.4: Absorption of X-rays for different thickness Au films. For comparison a 2.5 μm Bi is also plotted for reference. Data from online database [81].

result was that the thermal conductance G was 0.404 nW/K at 100 mK and the exponent of thermal conductance was obtained to be $n = 3.6$ (Fig. 5.5)

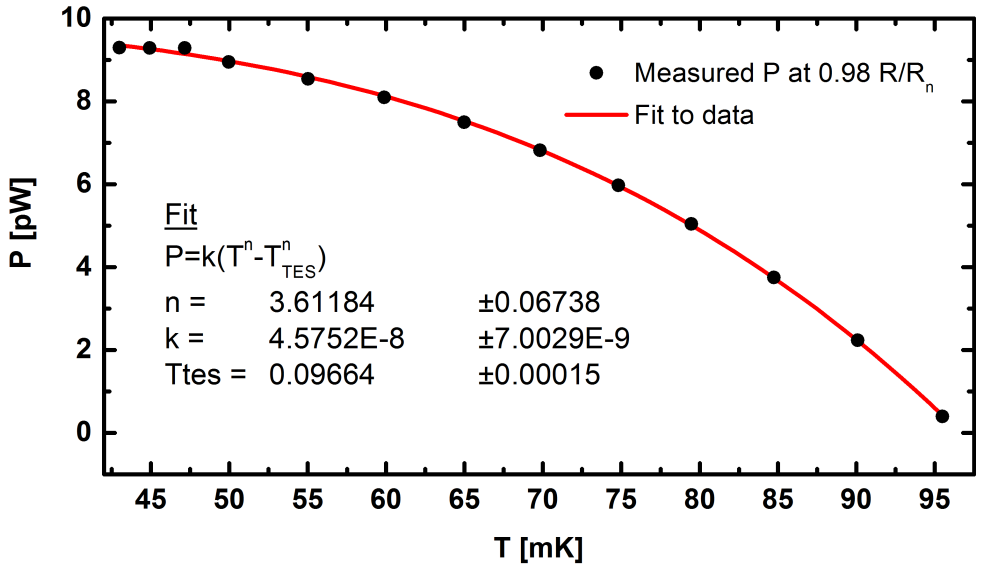

Figure 5.5: Power at 98% R/R_N as function of temperature for the test sample on VTT Si_3N_4.

After the thermal conductance was measured, other parameters could be evaluated. First the C of Corbino pixels were calculated by using literature

values for materials [79],[24]. The specific heat of a material is $c = \gamma T + AT^3$, where the first term comes from electronic contribution and the second from phonons. At low temperatures for metals the phonon part can be neglected. By knowing the volume of each contributing element the heat capacity of the detectors could be calculated. Three different size absorber were evaluated with diameters 190 μm (large, L), 122.5 μm (medium, M) and 55 μm (small, S). The TES film was also taken into account, when calculating the total C of the devices. Of course by decreasing the absorber diameter the active detector area decreases lowering the amount of absorbed X-rays in actual measurements.

The energy resolution in an ideal case can be approximated with the equation [24]

$$\Delta E_{FWHM} = 2.36\sqrt{4k_B T_0^2 C \frac{1}{\alpha}\sqrt{\frac{n}{2}}}. \tag{5.1}$$

By using a typical value for the transition steepness, α=100, a theoretical energy resolution for different thickness absorbers was obtained (Fig. 5.6).

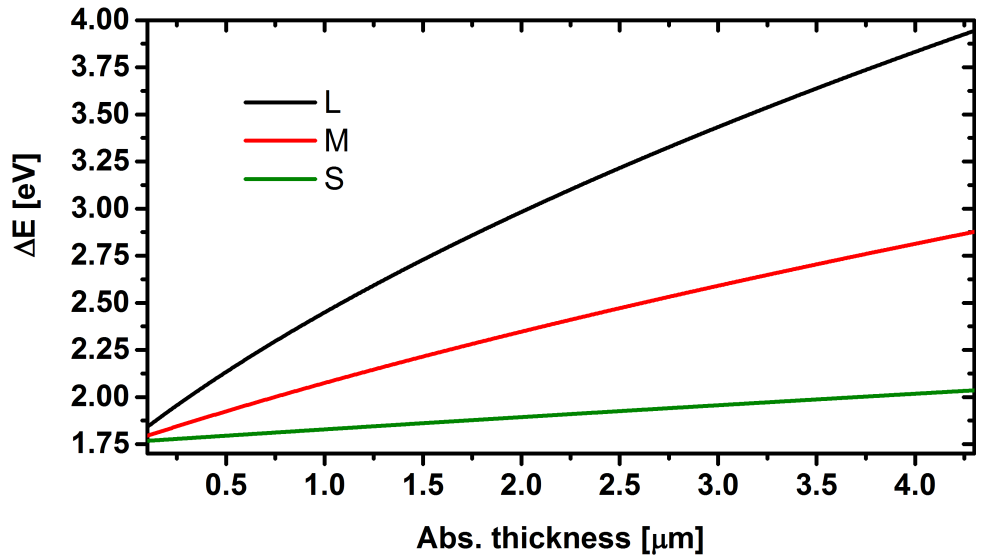

Figure 5.6: Energy resolution for different size absorbers as a function of absorber thickness.

For a TES to operate stably, the solution for its response needs to be stable and usually critically damped [25], which means that the signal has the fastest decay without oscillations. The stability was modeled with a formula [24]

$$\tau > (\mathscr{L} - 1)\tau_{el} = (\mathscr{L} - 1)\frac{L}{R_L + R_0(1 + \beta)}. \tag{5.2}$$

The inductance used in the TES circuit of the NIST SQUID system used here is $L = 275$ nH, which was used in the calculation. Values for other parameters used in the calculations were R_L=0.3 mΩ (shunt resistance), R_0=1 mΩ

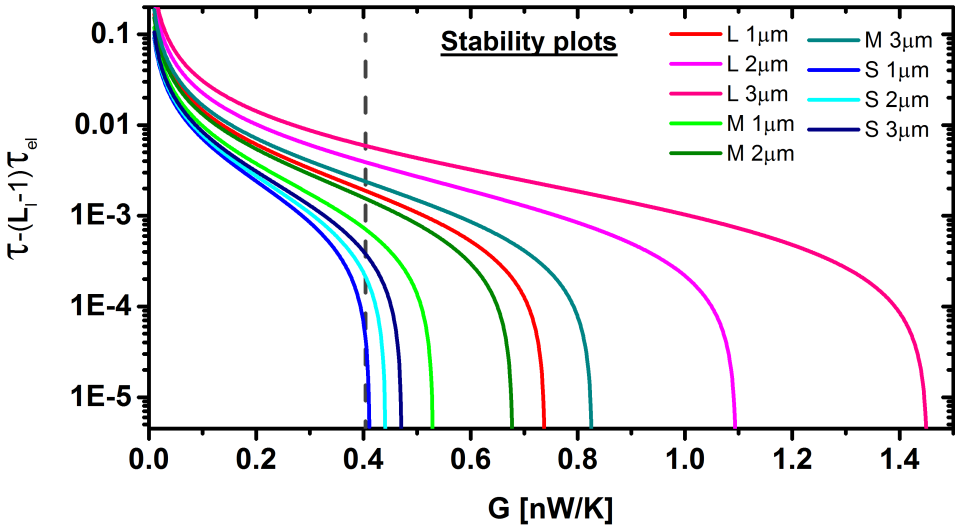

Figure 5.7: Positive values of $\tau - (\mathscr{L} - 1)\tau_{el}$ (stable operation) plotted as a function of G. The dashed line is the measured value of G at 100 mK for the 500nm thick Si_3N_4

(approximate TES resistance when biased low in the transition) and β was approximated to be 1. A set of curves were calculated that are plotted in Fig. 5.7.

Conclusion from the stability analysis is that at least with this naive calculation all of the detector geometries should be stable with the measured G.

The saturation energies as function of α for each TES with a different size absorbers were evaluated with an approximative formula calculated by Ullom [82]

$$E_{sat} = 0.8CT_C/\alpha. \tag{5.3}$$

In the graph in Fig. 5.8 is the evaluated saturation energies as function of the transition steepness for different heat capacity detectors. For the detector to be able to measure X-rays near 10 keV one can see that the α can not be much higher than 200 for any of the designs.

From the modeling the outcome was that we decided to use 2 μm thick Au as the absorber. We decided to make 9 different Corbino designs. Absorber diameters were designed to be 190 μm, 122.5 μm and 55 μm. Each of these would have three different size inner contacts 35 μm, 45 μm and 55 μm by varying the diameter of the middle hole in the insulator layer. This way we could ensure to have normal state resistance, R_N, value that would couple well with the read out.

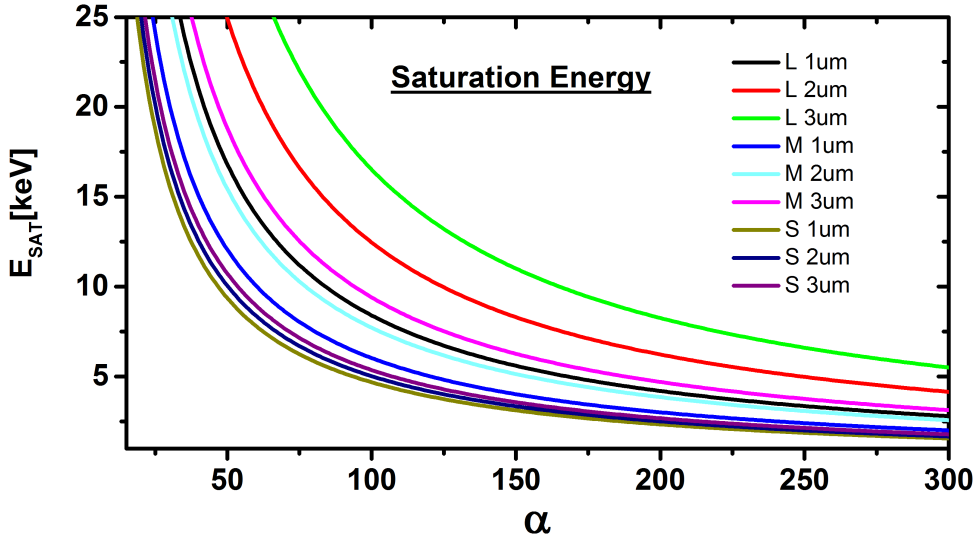

Figure 5.8: Saturation energy estimate as a function of α. L refers to the largest diameter absorber, M for the medium and S for the smallest.

5.3 Fabrication of 256 Pixel TES Arrays

5.3.1 Hunt for the Critical Temperature

The Molybdenum-Copper bi-layers have been used extensively and other groups have reported [66] that Mo/Cu thickness' of 100nm/200nm have given them a critical temperature around 100mK. As the T_C of a proximized superconductor is highly sensitive to the film properties, calibration of the thickness monitors, processing temperature and pressure, the processing parameters differ from lab to lab and thus we had to find the best film thicknesses for our process. In principle the T_C of a bilayer can be evaluated from the Usadel theory [83].

For our first test wafer, we chose to fabricate a film with 100 nm of Mo with 200 nm of Cu on top, which yielded a T_C of 240 mK. Between the Mo and Cu we also used a 10 nm layer of TiW as a diffusion barrier. TiW has been seen to act as an interdiffusion barrier [84] and it's purpose was to keep the interdiffusion minimal in the later processing stages, especially with higher temperature processing steps. After a few fabrication iterations we got the T_C close to 100 mK with 75nm of Mo and 240nm of Cu.

The samples for T_C-tests were unpatterned chips (about 10 mm $\times$ 2mm) cut from 6 inch wafers. The $R(T)$ curves were four-probe measured with a lock-in amplifier with about 10 μA AC current. Data from the measured T_C-tests is shown in Fig. 5.9. By knowing the dimensions of the chip, the resistivity of the Mo/TiW/Cu films could be also calculated from the measured resistance. The sheet resistance was measured to be 20–30 μΩ. For Corbino devices the resistance has a logarithmic dependence on the ratio of the inner and the outer

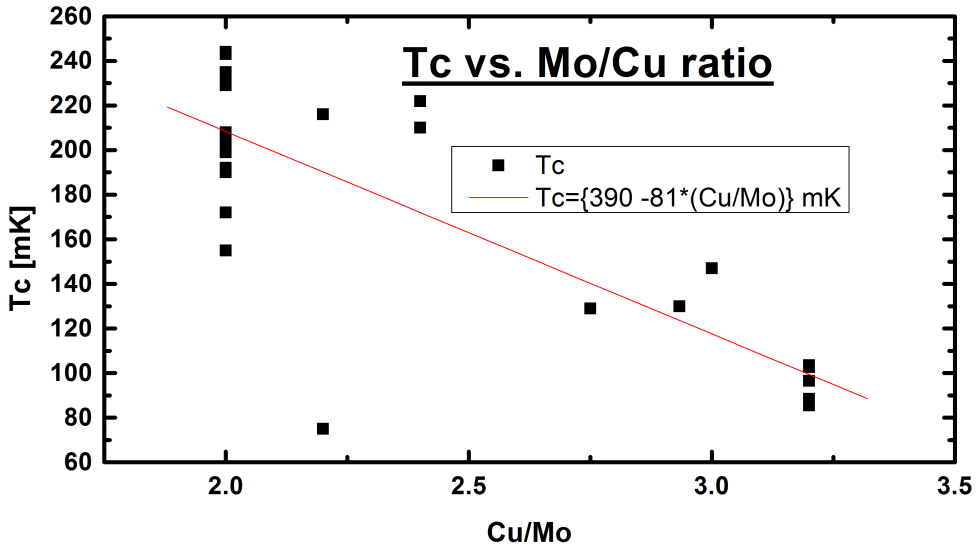

Figure 5.9: Critical temperature as a function of Mo/Cu ratio.

electrode radius

$$R = \frac{\rho}{2\pi h} \ln \frac{r_2}{r_1} = \frac{R_\square}{2\pi} \ln \frac{r_2}{r_1}. \tag{5.4}$$

From Equation 5.4 it can be seen that by changing the size of the inner radius the resistance of the pixel can be tuned [85]. Plugging in the measured sheet resistance and the radii (35 µm and 170 µm) to the Equation 5.4 one gets a device resistance of 6–8 mΩ, which is value that's well coupled with the read out electronics. Square Ti/Au devices that we've made at the NSC have had over 20 times larger resistances [86], which is the main reason why we opted to use Mo/Cu and the Corbino design.

5.3.2 The Process Steps

After the correct parameters to produce the desired T_C were found the masks for the optical lithography process were designed and ordered. In total 8 masks were used. As the processing was done on 6 inch wafers a total of 36 chips (15 mm×19 mm) could be fitted on one wafer. The size of the chips were chosen so that it would fit to the existing detector read out unit designed by NIST.

Different chip designs were made by varying the dimensions of the detectors. Three different sizes of center contacts were used to vary the normal state resistance. Also three different sizes for the absorber diameter were used to make detectors suitable for different energy ranges.

380 µm thick Double Side Polished (DSP) silicon wafers were used as a substrate. Standard UV-photolithography [76] and a contact mask aligner were used.

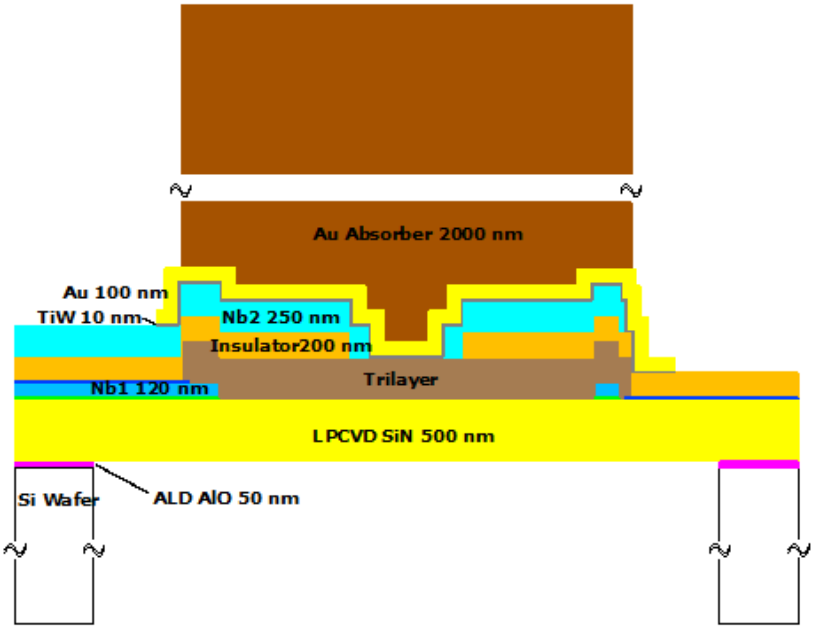

Figure 5.10: A schematic cross section of a pixel where absorber covers the whole TES area.

The fabrication was done by L. Grönberg at VTT Micronova facilities. Next the processing steps are covered in detail. The sideview schematic of a finished detector is shown in Fig. 5.10.

As a first step a 50 nm AlO_x layer was deposited by Atomic Layer Deposition (ALD) [87] after which a 500 nm thick low stress silicon nitride by Low Pressure Chemical Vapor Deposition (LPCVD) [88]. The purpose of the AlO_x was to act as an etch stop layer when etching through from the back of the wafer as a final step to release the Si_3N_4 membranes on top of which the single devices sit on.

A 10 nm ALD AlO_x was deposited on top of the LPCVD Si_3N_4, followed by sputtering [77] the first 120 nm superconducting niobium layer (Nb1), which will form the outer annular bias contact for the trilayer. The Nb1 was patterned by plasma etching and the 10nm AlO_x acted as an etch stop layer. After the patterning of the Nb1 layer the 10 nm AlO_x was wet etched [77] by using the Nb1 wiring as the mask. A third 10 nm ALD AlO_x was then deposited and patterned to act as an etch stop layer when patterning the superconducting trilayer. The AlO_x was removed from the areas that will be under the trilayer.

In the next phase the Mo/TiW/Cu trilayer was deposited by sputtering. The top Cu layer was Ion Beam Etched (IBE) [89] and the TiW and Mo layers were Reactive Ion Etched (RIE) [76]. The third AlO_x was then wet etched. An insulating SiO_2 layer was then grown by Plasma Enhanced Chemical Vapor Deposition (PECVD) [77] and the contact openings were wet etched. After

this the second superconducting niobium lead layer (Nb2) was sputtered and patterned. The Nb2 layer acts as bias leads, forms the upper contact to the trilayer and also acts as a magnetic shield to it. After patterning the Nb2, the areas where the absorber will contact the trilayer will be exposed.

The 2 μm gold absorber was electrodeposited with a help of 10/100nm TiW/Au seed layer. The absorbers were patterned with a thick photoresist, and after the electrodeposition another layer of photoresist was applied to protect the absorber, and the seed layer was etched from areas outside the absorber. Gold was chosen over *e.g.* bismuth, because fabrication of high quality Bi films is not trivial [90], and because the fabrication facility at the Micronova is not suitable for production of Bi films without investments in a dedicated system.

After all the patterning was done on the frontside of the wafer, the patterning on the backside could be done to release the Si_3N_4 membranes. First a protective photoresist was applied on the front side of the wafer. Then circular holes to the LPCVD Si_3N_4 film on the backside were patterned with RIE. Next by using the holes in the Si_3N_4 as a mask the AlO_x was wet etched. After this the wafer was etched through to free the membranes by using an Inductively Coupled Plasma (ICP) etcher, where the Si_3N_4 and AlO_x layers were used as an etching mask. The AlO_x under the Si_3N_4 on the frontside of the substrate acted as an etch stop layer for the Si etch. As a final step the AlO_x under the released membrane was removed by using chlorine based ICP etching. In Fig. 5.11 is a photograph of a finished detector array and in Fig. 5.12 are Scanning Electron Microscope (SEM) images of a chip.

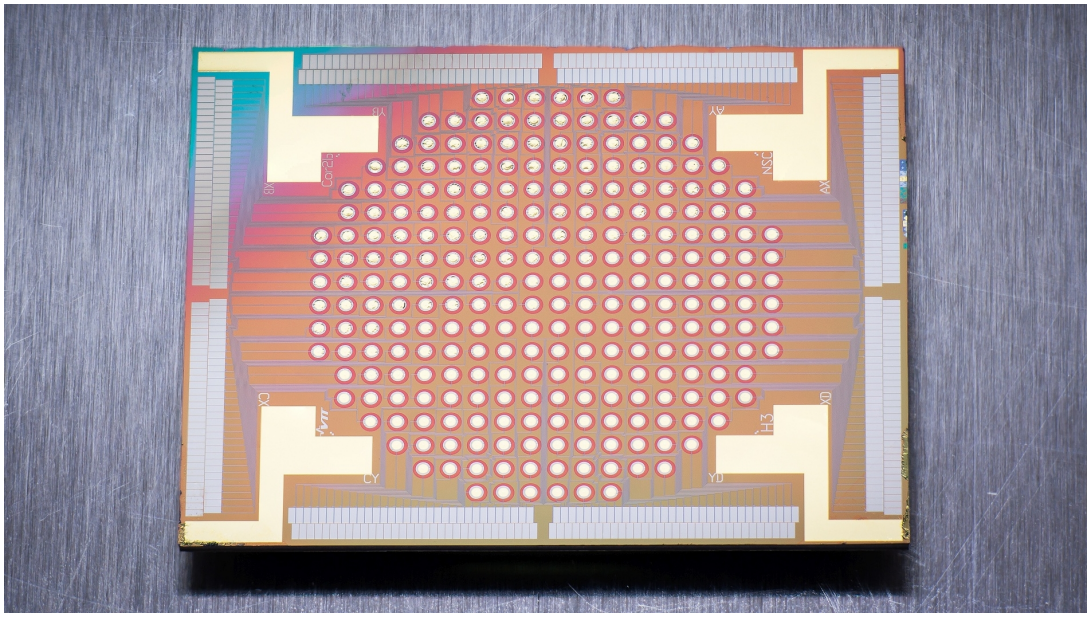

Figure 5.11: Macro photograph of a finished detector array with the largest absorber (covering the whole trilayer).

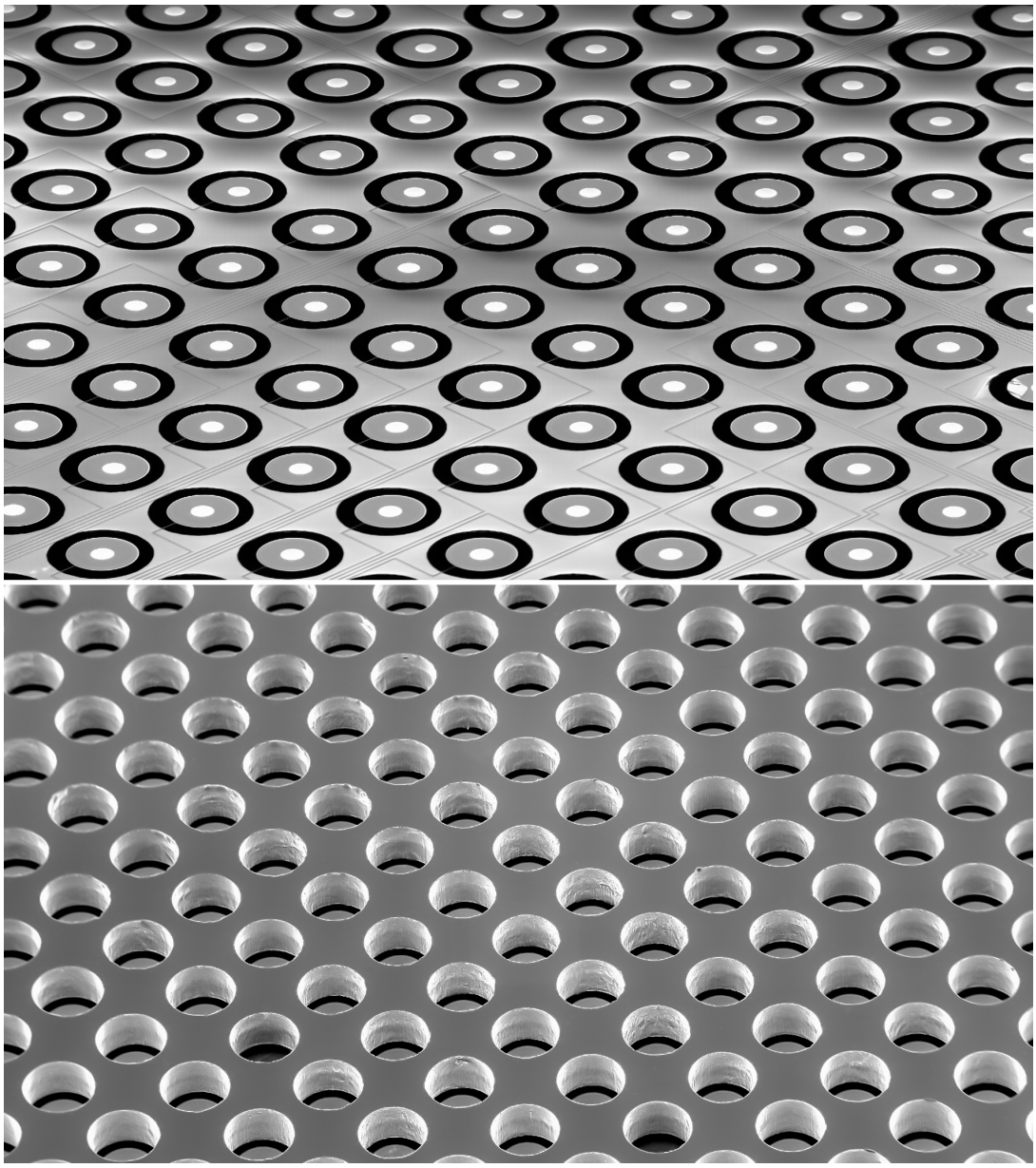

Figure 5.12: Top: SEM image taken in 60° angle of a Corbino array with the smallest diameter absorber. Bottom: SEM image from the backside of the chip after the membrane release.

5.4 Characterization of a TES Array

5.4.1 Cryogenics and the Electrical Measurement Setup

To cool down the detectors below their critical temperature requires sophisticated cryogenics. The electrical characterization measurements were done in a in-house built ^{3}He-^{4}He dilution refrigerator [91]. Our cryostat is built in a such way that it fits into a standard liquid ^{4}He-dewar (Fig. 5.13), which makes the cool down rather fast and low cost, with temperatures below 50 mK reached routinely.

Figure 5.13: A ^{4}He-dewar

The downside of a small cryostat is that there is not much room for samples and the cooling power is also quite small. This limits the number of electrical wires that can be connected to the coldest parts of the cryostat due to heat flow from room temperature, which means that only a few samples can be measured simultaneously.

Our cryostat has 12 unfiltered measurement lines that can be used for electrical measurements. The cryostat is equipped with a heater resistor at the still to control the amount of cooling. Usually a constant voltage is held over the still heater to achieve maximal cooling, and the temperature is controlled with a another heater at the sample stage. The temperature of the sample stage is measured with a RuO_x resistor that is located right next to the samples. The RuO_x is calibrated with a commercially calibrated Ge thermistor. To read out the resistance of the thermometer a Picowatt AVS-47 resistance bridge is used. To control the temperature a Picowatt TS-530 temperature controller was used in most measurements. However, it causes unwanted noise in the SQUID

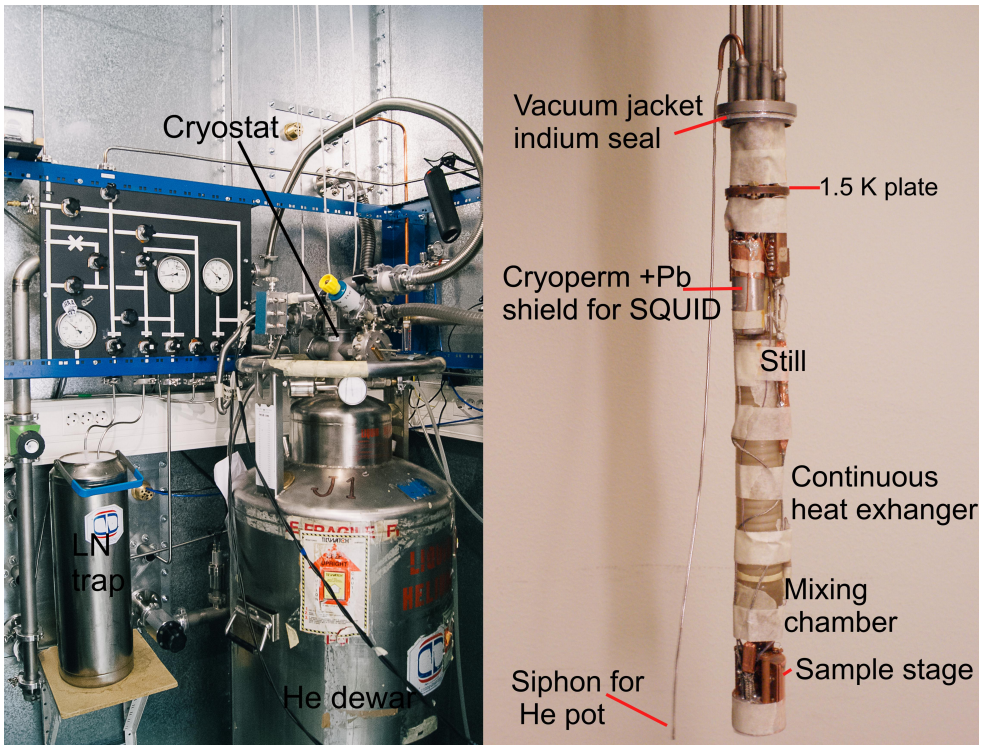

Figure 5.14: Left: A photograph of our shielded measurement room with the He dewar and the cryostat in it. Right: Photograph of the cryostat without the vacuum jacket.

measurements, and in those cases a less noisy LabVIEW based software PID controller with the output of the DAQ card was used.

SQUID Readout

Our dilution refrigerator is equipped with a two-stage SQUID from NIST. It has eight input channels, only one of which is wired to the sample stage. The second stage consists of 100 SQUID series array and it's on the same chip as the first stage. The SQUID chip needed to be installed at the 1.5 K stage due to the power consumption of the SQUID array, which makes the setup somewhat sensitive for noise pickup and also the input inductance is increased due to length of the wires running from the sample stage to the 1.5 K stage.

The room temperature readout and control electronics for the SQUID was designed at SRON (Netherlands Institute for Space Research). The electronics consists of a preamplifier module that attaches at the cryostat and a remote control system for SQUID biasing. More information and details about the readout can be found in K. Kinnunen's thesis [31].

5.4.2 Critical Temperature Measurements

To study the film uniformity critical temperatures were measured from seven different chips from two different wafers. The electrical contacts to the samples were wire bonded with a 50 µm Al wire. Because of the limited number of measurement lines, all the samples had a common current line and the voltage was measured over each pixel (Fig. 5.15). This way with 12 measurement lines 9 samples could be T_C checked in one cooldown. T_c measurements were done in a four-probe lock-in measurement with a 10–25 µA (rms) 17 Hz AC current with SRS 830 digital lock-in amplifier and Ithaco 1201 voltage amplifier.

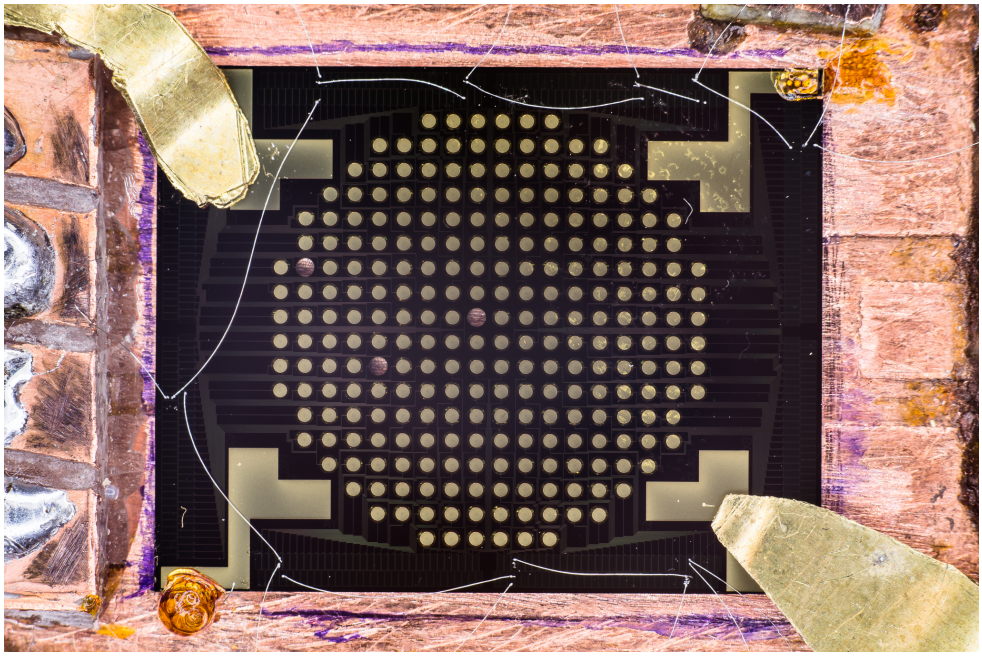

Figure 5.15: Photograph of an array bonded and ready for a T_C test.

For the most chips the T_C:s were between 80–200 mK with about 10 mK standard deviation. In one chip with no absorber, the spread was quite large being 150–500 mK.

One of the chips was chosen to be used in further characterization. The detector array chosen was the one with the biggest absorber and the smallest inner bias radius – largest heat capacity and highest resistance. In total 26 T_C:s were measured from this chip (Fig. 5.16) The standard deviation of the T_C from different pixels was quite large. This makes it hard or even impossible to bias multiple pixels reasonably with one bias voltage. This is needed in multiplexing, when typically 20 pixels are biased with same voltage in order to limit the number of wires going to the coldest part of the cryostat. The double transition or the knee structure is not typical for Corbino detectors and it was also visible in I(V)-measurements. To rule out the possibility of the absorber proximising

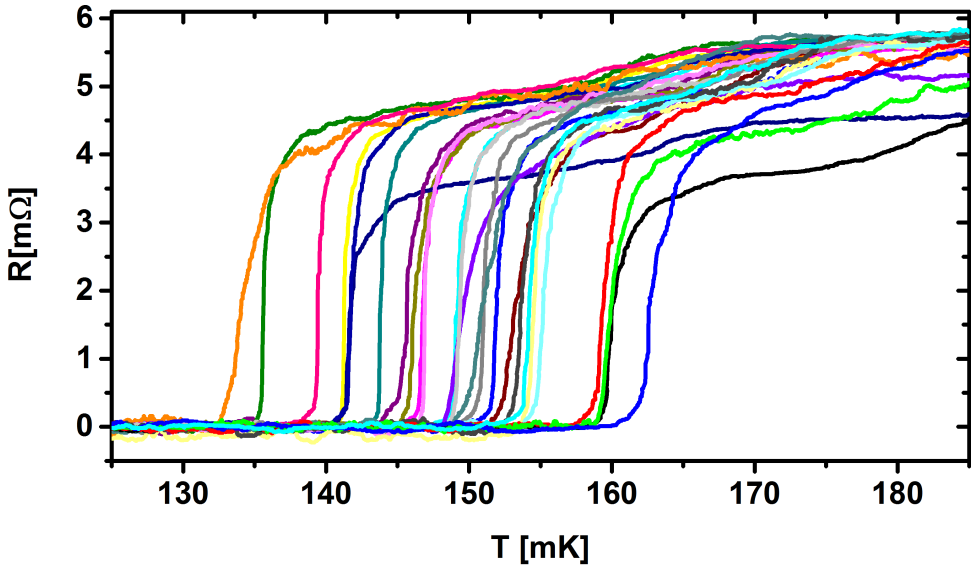

Figure 5.16: Critical temperatures measured from one chip that was more extensively studied. The Standard deviation was 7.5 mK and the normal state resistance around 5.5 mΩ with a couple of outliers.

the bilayer locally and maybe longitudinally [92], an array without the absorber was also T_C checked. The critical temperature of a couple of detectors from an array without absorbers were measured in order to see if the absorber is the cause of the double transition (Fig. 5.17). Because even without the absorber some pixels showed the double T_C behavior, the reasonable conclusion is that the patterning and the Mo/TiW/Cu material is the origin of the feature. Some pixels without absorbers did, however show nearly ideal transition shapes. No double T_C features have been seen in either Ti/Au Corbino devices or plain Mo/TiW/Cu thin films.

5.4.3 Noise and Impedance Measurements

A few of the pixels shown in Fig. 5.16 were selected for more extensive electrical measurements. Current-Voltage (I-V), complex impedance [30] and noise measurements were carried out. By measuring I-Vs at different bath temperatures (Fig. 5.18 a) the exponent of thermal conductance n, was obtained to be $n = 3$ (Fig. 5.18 b)) by plotting the TES power at R/R_N=0.75 as a function of bath temperature. From the IV-data the steepness of the transition α_{tot} that incorporates both the current and temperature sensitivity were calculated as a function of bias points [31]. The values for α_{tot} were slightly below our design value of 100 and from the values that have been typical for Ti/Au Corbino devices [74] (Fig. 5.19 a)). The inset at Fig. 5.19 a) shows the measured complex impedance with the best fit with a three-block model discussed earlier. Fig. 5.19 b) shows

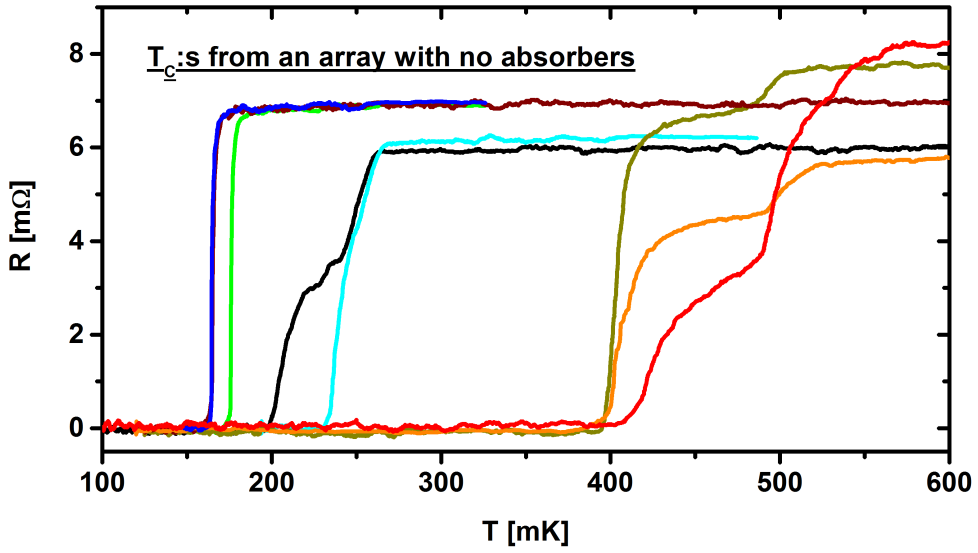

Figure 5.17: Critical temperatures measured from an array with no absorber. Some pixels show the double transition, while others don't.

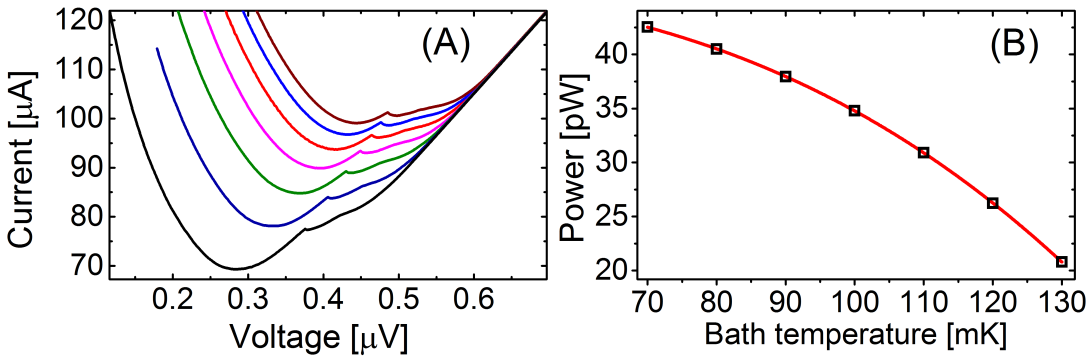

Figure 5.18: a) IVs at different bath temperatures (70–130 mK). b) $P = K(T_{TES}^n - T_{bath}^n)$ fitted to experimental data. n=3 and $K = 11$ nW/K^3.

the corresponding noise measurement at the same bias point with a fit from the three-block model fitted simultaneously with the complex impedance data. The figure also shows the different noise components, where phonon noise refers to thermal fluctuation noise between the TES and the bath, ITFN is the thermal fluctuation noise internal to the TES and Johnson refers to the nonlinear electrical noise of the TES [48]. Also the current noise calculated with a simple thermal model is plotted to show that the measured noise can not be explained with a simple model.

From the noise data the predicted energy resolution was calculated for this pixel to be $\Delta E = 9.5$ eV. This particular pixel was designed for high energy X-rays and it has an estimated saturation energy $\sim$ 68 keV (heat capacity

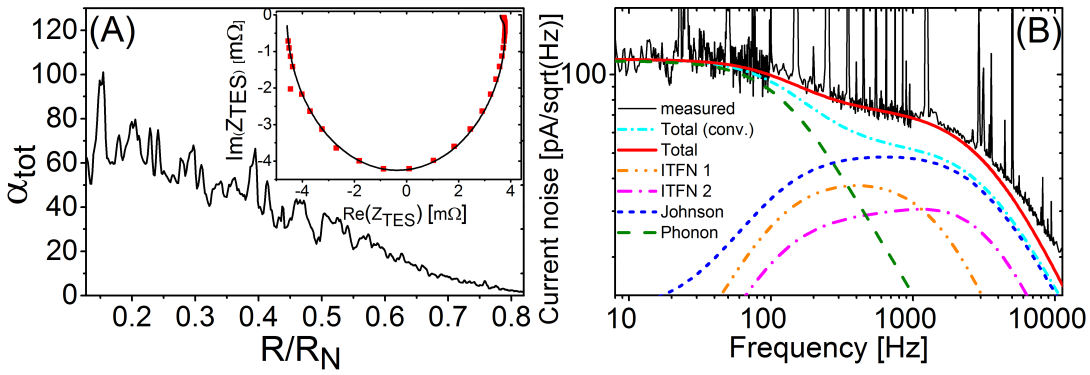

Figure 5.19: a) α_{tot} as function of bias point calculated from the 130 mK bath temperature I-V curve. The inset shows the measured complex impedance at R/R_N= 0.5 and fit to data with a three block thermal model. b) The noise spectrum at the same bias point and the three block fit with a breakdown of the noise components.

C=2.4 $\times 10^{-12}$ J/K). It also had quite a high critical temperature of 152 mK. For the smaller heat capacity devices and with a T_C of 100 mK the energy resolution should be around 3 eV.

The array that was most analyzed was also attached to the X-ray measurement system discussed more in Chapter 6 and a few pixels were bonded (this was the snout that only had readout for 12 pixels). The energy resolution for Mn Kα was above 20 eV, which is still far from the predicted. The full reason for this discrepancy is currently unknown. It might be because of read-out issues, but we also note that no collimator was used in the measurements, which can cause photons to absorb at the substrate and by so degrade the energy resolution. Nevertheless, X-rays were recorded and the pulse shapes were quite similar with a NIST detector described in Section 6.1.1 and with our Corbino detector (Fig. 5.20). The rise time and the decay time of a Corbino were slightly longer compared to a NIST detector.

X-ray measurement were done with an ^{55}Fe source at multiple bias point for one of the pixels to see how it affects the energy resolution. NIST detectors are biased low at the transition (about 10 % R/R_N). Because of the non-linearity of α as a function of bias point in the Corbino detectors, this might not be ideal for them. From Fig. 5.21 it's apparent that the Corbino detectors need to bias a bit higher at the transition to achieve the best energy resolution.

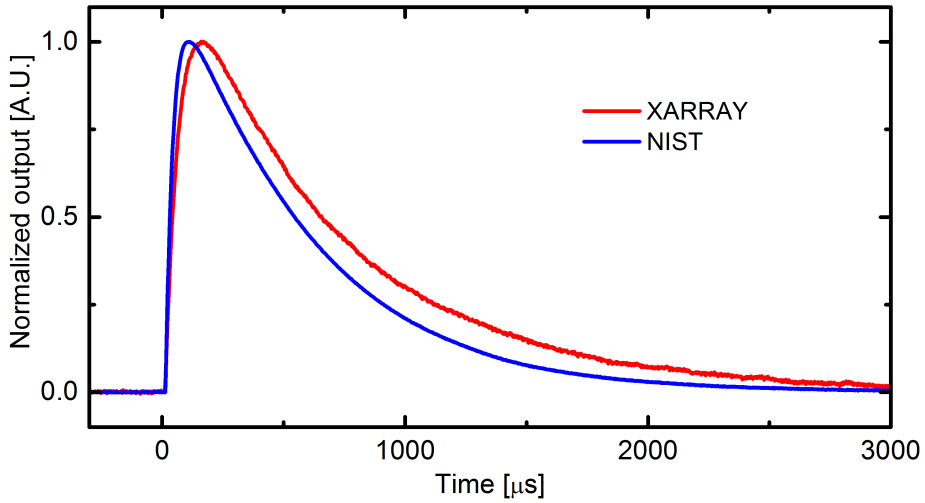

Figure 5.20: Pulse comparison between a NIST TES and a Corbino TES for 5.9 keV photons. The effective time constants were 710 μs and 860 μs respectively.

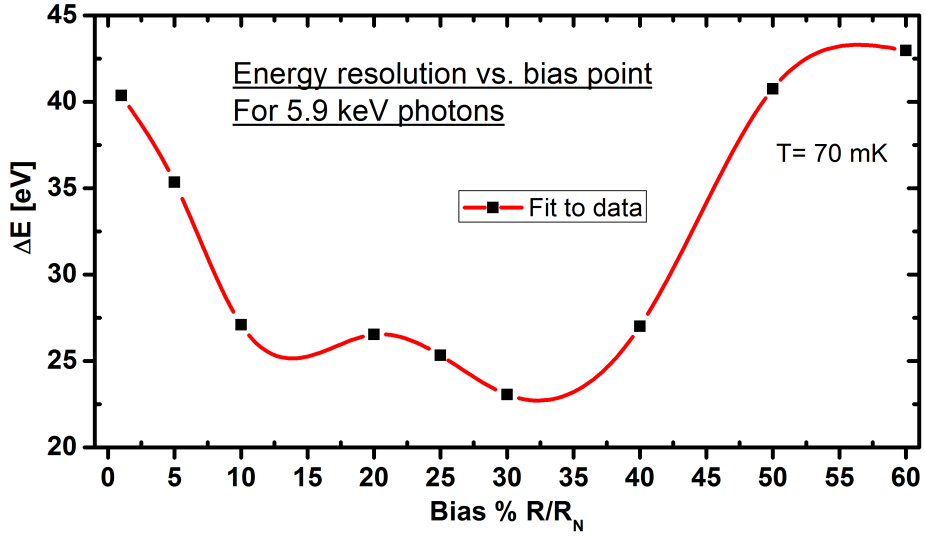

Figure 5.21: The energy resolution of a Corbino detector as a function of bias point.

Chapter 6

Particle Induced X-ray Emission Measurements

6.1 PIXE in Jyväskylä

The main tool of the Accelerator based materials physics group is the 1.7 MeV Pelletron accelerator (Fig. 6.1). It has beamlines for Rutherford Backscattering Spectrometry (RBS) [93], Time-of-Flight Elastic Recoil Detection Analysis (ToF-ERDA) [94], Ion Beam Lithography (IBL) [95] and one for PIXE. The energy range for ions that can be used start from less than 200 eV for H, He and O and for the multiply charged heavy ions goes up to 20 MeV.

The main results of the TES-PIXE experiments are reported in articles A.II and A.IV.

Figure 6.1: Photograph of the accelerator lab. On the left is the Pelletron accelerator. In center of the frame are the different beamlines and on the right is the TES setup connected to the target chamber.

6.1.1 The Measurement Setup

The TES array

The 160 pixel TES detector array used in all PIXE measurements was fabricated at NIST Boulder. The superconducting thin film is a Mo/Cu bilayer with a critical temperature of about 100 mK. The absorbing material is a $350\times350\times2.5$ μm^3 Bi and the collimator sits on top of the detector separated by 20 μm distance and it has a 320 μm $\times$ 305 μm aperture size for each pixel. The purpose of the collimator is to prevent photons from hitting the substrate. The sides of the superconducting Mo/Cu bilayer perpendicular to the bias leads have thick 500 nm Cu banks to suppress the T_C fully at the edges. This is done to prevent local T_C variation at the edges due to imperfect contact between the layers [75]. A finger structure with 500 nm thick Cu fingers is deposited on top of the Mo/Cu film to make the supercurrent travel in a zig-zag pattern inside the bilayer. This has been shown to decrease the unexplained noise [47] by reducing the α of the detector[82].

Demonstration of combining a single TES detector pixel with PIXE have been published before [96], but the energy resolution achieved (18 eV at 1.7 keV) has been much worse than in the work presented in this thesis.

Silicon Drift Detector

As a Silicon Drift Detector (SDD) is used as a reference detector in the measurements its basic working principle is presented here. The device was first introduced in 1984 by Gatti and Rehak [97]. The operation of the detector is based on collecting ionized electrons generated by photons. Radiation absorbed in the detector's sensitive area creates mobile electron-hole pairs [98]. The electrons are then drifted with an electric field to the anode, after which the signal is amplified [99].

The energy of the photon is proportional to the charge collected at the anode. Typically the devices are peltier cooled to around –60°C to minimize thermally excited electrons that degrade the resolution [100]. Commercial cooled SDDs have a FWHM at Mn Kα (5.9 keV) typically around 130 eV with a count rate up to 100 kHz. These merits also hold true for the Amptek X-123SDD Silicon drift detector that we used as a reference detector.

Adiabatic Demagnetization Refrigerator (ADR)

The cryogenic cooling of the TES array was achieved with an ADR (Denali Model 102 by High Precision Devices, Inc.) (Fig. 6.2). The pre-cooling of the ADR's two stages (60 K and 3 K) was done with a Cryomech pulse-tube refrigerator (model no. PT407 RM). This makes the whole system cryogen free, meaning that no liquid nitrogen or helium is needed to cool down the system. The system uses two types of paramagnetic salts: Gadolinium Gallium Garnet

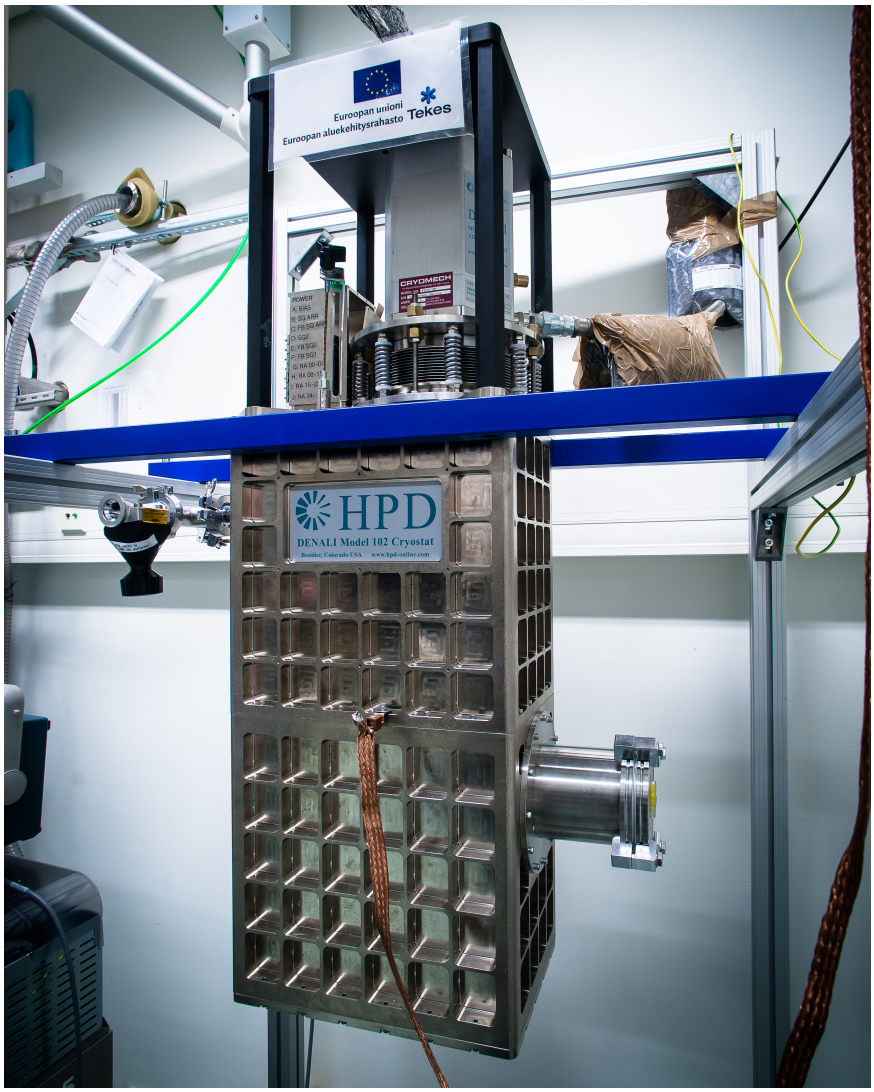

Figure 6.2: A photograph of the ADR

(GGG) and a Ferric Ammonium Alum (FAA). A 4 T magnet that is used to align the spins of the salt pills is controlled by software and hardware made by STAR Cryoelectronics LLC. The current to the magnet is fed by a Kepco BOP bipolar power supply (BOP 20-10M). All of the critical electronics are behind an Uninterruptible Power Supply (UPS) to prevent uncontrolled magnet ramp down and a possible quench of the superconducting magnet during a power outage. To minimize vibrations to the cold part of the ADR the pulse tube is equipped with a remote valve system and flexible bellows between the pulse tube and the cryostat body. Sandbags and lead weights are also placed in strategic places of the ADR system and the table where the ADR sits on is damped with foam and rubber feet to minimize any vibrations from the building.

Before the pulse tube is turned on the inner parts of the ADR are carefully

pumped to vacuum. Caution is required as the outer AP3.3 vacuum window is quite fragile and quick pressure changes can break it. Same holds true for the IR filters. To ensure slow enough pumping rate the pumping is done in the beginning through a valve where the gas flow impedance can be controlled. After the pressure inside the ADR has reached below 10^{-2} mbar the valve is slowly opened more to speed up the pumping. This initial pumping can last over a day depending how much out gassing from the insides occur. When the pressure is below 5×10^{-4} mbar the pulse tube is switched on and the cooling starts. After the 3 K stage of the ADR reaches 50 K, the pumping is closed as the cryopumping of the ADR itself becomes more sufficient. When warming up the cryostat, pumping has to be started at temperatures around 77 K to check that there is not a pressure build up due to a leak. Again this is done to protect the vacuum window, which can not withstand an overpressure above 1 bar. One additional precaution is done when pumping the measurement chamber that is connected to the end of the ADR snout when *e.g.* changing samples. The whole pumping system is vented (the turbo pump is closed from front and back) to ensure that the pumping starts from atmosphere, instead of leaving a low pressure at the backing pump that is also used as a rough pump for the chamber.

When the base temperature of the pulse tube coolers have been reached the cool down to the base temperature of the ADR can be done. First the magnet current is ramped up to about 8.5 A in a time of 30–45 minutes, while the mechanical heat switch that contacts the 50 mK stage to the 3 K stage is closed. After the maximum current has been reached the current is held there for about 60–120 minutes to dump the heat generated during the ramp up from the 50 mK stage to the 3 K stage. After this soak time when the 50 mK stage temperature has saturated, the heat switch between the 50 mK stage and the 3 K stage is opened. Then the magnet current is ramped down between 30–45 minutes decreasing the 50 mK stage temperature below 40 mK. During a temperature controlled measurement, a small current is fed through the magnets that is PID controlled to hold a specific temperature. In normal operation hold times at *e.g.* 70 mK are longer than 15 hours, after which another regeneration cycle is needed. Typical behavior of the ADR at different times of operation is shown in Fig. 6.3.

During the first measurements low frequency (30 – 60 mHz) vibrations caused a lot of headache and ruined many measurement hours. The vibrations seemed to start at random times and would last up to 18 hours. It caused the temperature to oscillate between 0.1–0.3 mK from the set value, which ruins the energy resolution of the detectors. The cause of the problem was searched all over the lab and the building from air conditioning to pump stations but in the end it turned out that an electronics board inside the ADR, where the SQUID array sits, was attached poorly (Fig. 6.4). After tightening the board the vibration issue was solved.

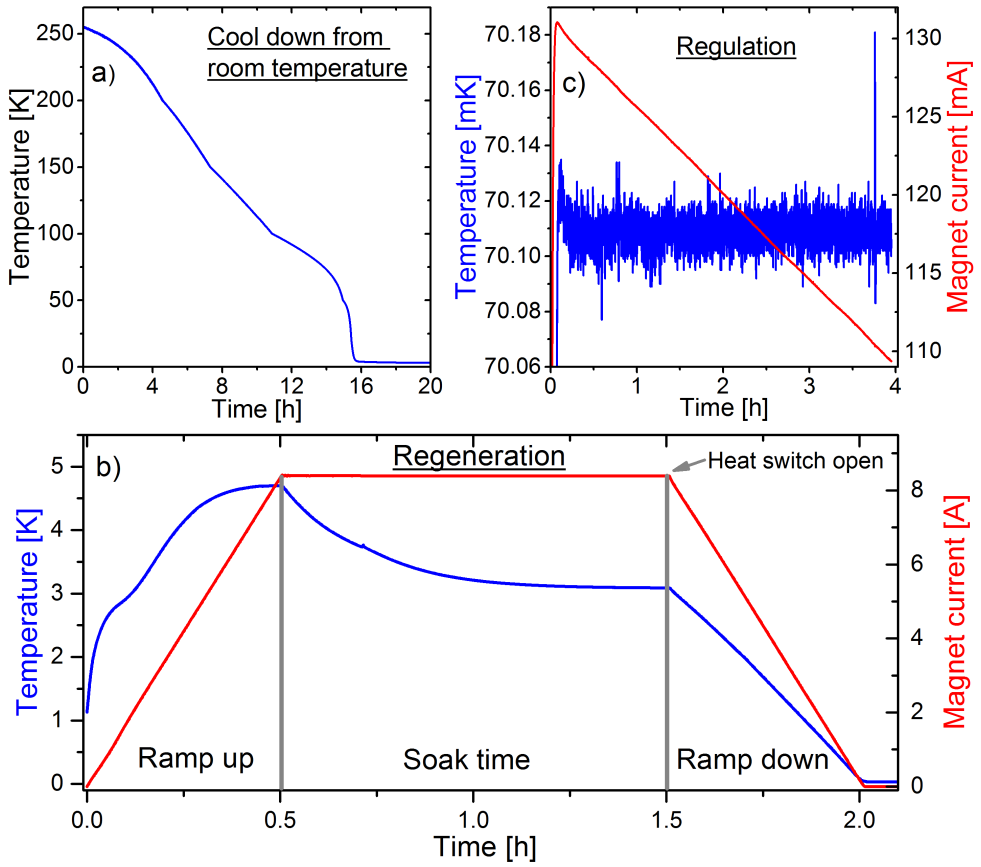

Figure 6.3: a) The cool down from room temperature. b) The current through the magnet and the 50 mK stage temperature during a regeneration cycle. c) The PID controlled temperature of the 50 mK stage and the current through the magnet during a typical measurement showing a standard deviation for temperature of less than 20 μK. The spikes in the temperature are due to external vibrations like someone bumping into the cryostat or a valve being closed at the beam line.

6.1.2 First Round of Measurements

In the first proof of principle measurements with TES-PIXE only 12 pixels were connected out of which 9 operated optimally. One of the pixels had major problems with SQUID locking, and two pixels had very small count rates during the measurements and they were omitted from the analyzed data. The outer 300 K snout of the ADR was connected to the measurement chamber with a plastic coupler to separate the grounds of the two pieces of apparatus (Fig. 6.5). The ADR and the chamber had separated vacuums. The vacuum window used at the end of the 300 K snout was a AP3.3 ultra-thin polymer/Al silicon grid X-ray window by Moxtek Inc. The backscattered incident ions were stopped with an 80 μm Polyethylene terephtalate (PET) film inside the sample chamber, that

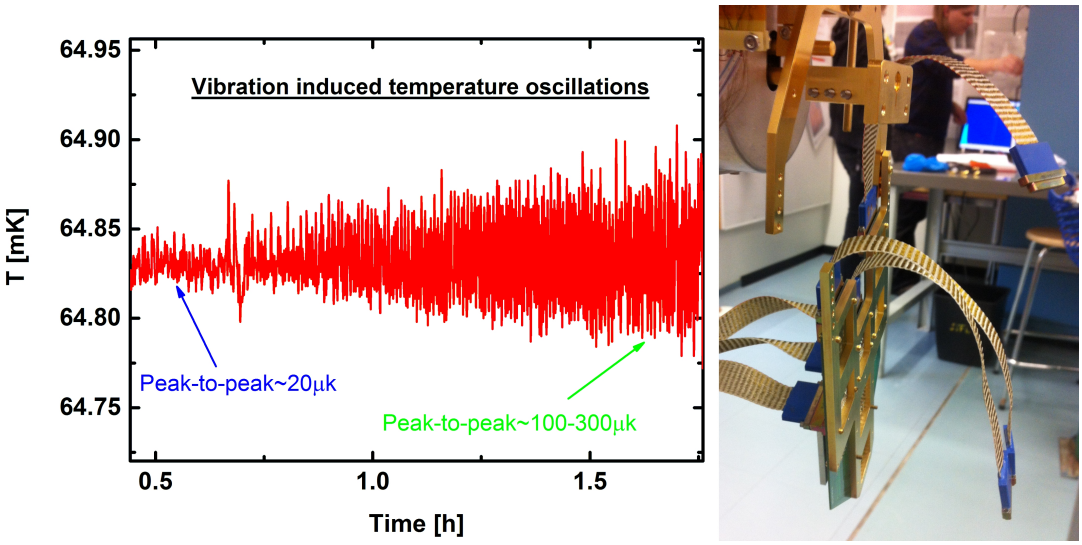

Figure 6.4: The plot on the left shows the behavior of the vibration and how it increases as a function of time. On the right is a photograph of the cause.

Figure 6.5: Left: The 300 K snout of the ADR connected to the measurement chamber with a plastic coupler. The separation of the grounds was later found to be unnecessary. Right: The second version of the coupling between the measurement chamber and the cryostat to shorten the distance from the sample to the detector.

also filters out low energy X-rays. The three cooling stages of the cryostat (60 K, 3 K and 50 mK) all had a 1 μm PET film with 1 μm Al coating at the end of each stages snout to block infrared radiation, which would otherwise saturate the detectors.

The SDD was positioned to an angle of 135° with respect to the ion beam

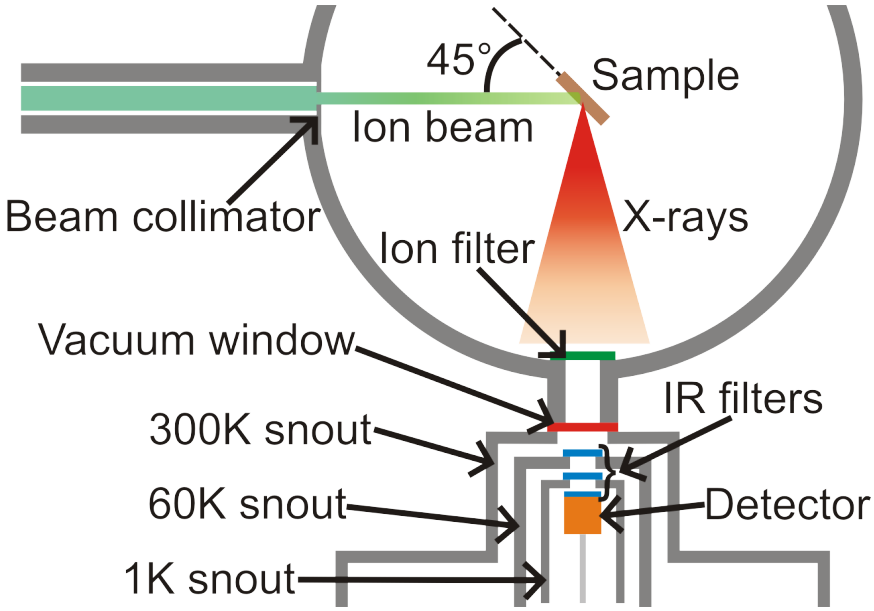

Figure 6.6: Schematic image of the target chamber and the ADR snout separated by a vacuum window. The distance from the sample to the detector was 30 cm. The dimensions are not in scale. The SDD measurements were done in a different target chamber.

and the TES X-ray detector to an angle of 90° and the sample was tilted 45° towards the detector (Fig. 6.6).

6.1.3 Second Round of Measurements

After the first set of measurements the detector unit was shipped to NIST for an upgrade. The detector chip was mounted on a new snout with a new multiplexer (MUX) and interface chips and all of the 160 pixels were bonded (Fig. 6.7). The old detector unit was left for testing purposes for our own detector arrays.

During the first iteration of measurements it became clear that the X-ray flux at the detector needed to be increased in order to measure thin film samples with reasonable measurement times and ion beam currents. This was done in three ways. Firstly, the number of pixels was increased. Secondly, the IR filters were replaced from the PET sheets with Al coating to homemade Si_3N_4 windows with Al coating, increasing the transmission. Thirdly, the coupling between the ADR and the measurement chamber was redesigned so that the 300 K snout goes into the chamber decreasing the distance between the source and the detector to 15 cm. This increases the flux by a factor of four, see Fig. 6.8.

The new IR-filters were fabricated at the NSC by wet etching the silicon substrate with KOH leaving a 280 nm thick Si_3N_4 membrane with 14 mm × 14 mm horizontal dimensions and evaporating 100 nm of Al on both sides of the chip

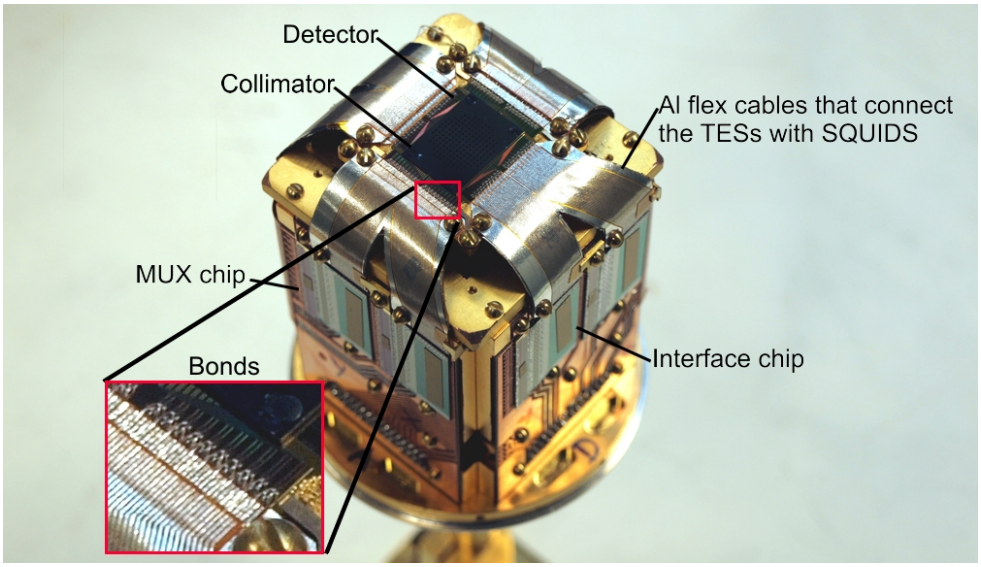

Figure 6.7: Photograph of the detector unit without the Al shield.

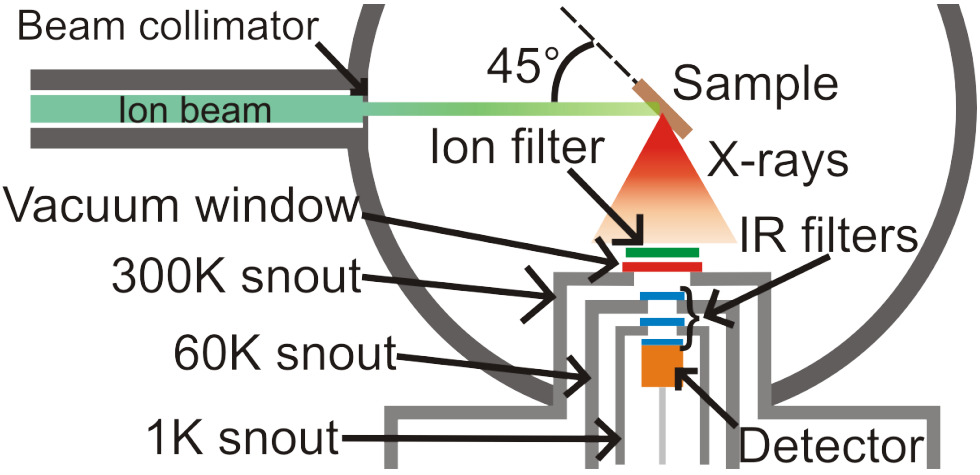

Figure 6.8: Schematic image of the target chamber and the ADR snout separated by a vacuum window after moving the setup closer.

to prevent pin holes (Fig. 6.9). The Si_3N_4-Al filters were tested with a Fourier Transform Infra-Red (FTIR) spectrometer[1] to ensure that they actually block IR and that they are pinhole free. The outcome of the measurement was that the filter transmission was (0.0 ± 0.2) % between 1.7 μm – 20 μm wavelengths. This was the range that FTIR instrument was able to analyze. The intensity maximum for a 300 K blackbody object has about 10 μm wavelength calculated with the Wien displacement law [101].

[1]Dr. Pasi Myllyperkiö ran the FTIR experiment at the NSC.

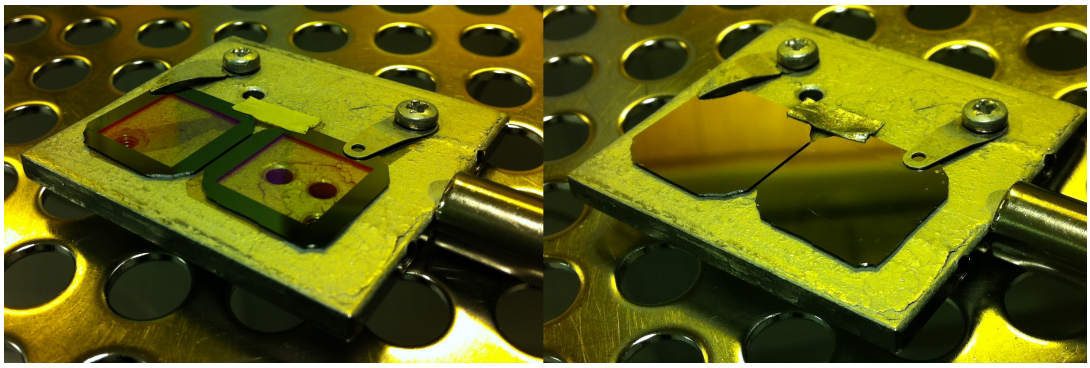

Figure 6.9: Before and after evaporating Al on the Si_3N_4 membranes.

To get quantitative data out of a PIXE measurement for the elemental composition of a sample, the X-ray transmission from the source to detector needs to be known. The manufacturer (Moxtec Inc.) of the vacuum window (AP3.3) for the ADR vacuum window doesn't provide the chemical composition of their window, so some reverse-engineering was needed. They provide a graph of the X-ray transmission at low energies out of which the composition of the polymer could be concluded by looking at the absorbtion edges. From the high energy data the thickness of the Si grid that fills 23 % of the filter area could also be deduced. Putting together these pieces of information we could calculate their X-ray transmission data by using the X-ray transmission calculator from [81]. To replicate the vacuum window transmission from 500 eV to 30 keV we used a polymer with a chemical composition of $BC_6O_2NAl_{0.6}$ with a thickness of 200 nm and a 200 µm thick silicon frame. The actual thickness of the filter might be different as the amount of hydrogen in the polymer is not known, but this does not affect the X-ray transmission in the energy range of interest. The gridded silicon support in a filter is not the best option for a detector that consists of pixels. It might explain why some of the detectors have slightly lower count rates than others.

When changing the PET-Al foils to Si_3N_4-Al thin films and the 80 µm PET foil that blocks the ions to a 125 µm Be sheet the transmission at *e.g.* 3 keV goes up from 9 % to 40 % (Fig. 6.10). After the changes elements P, Si and Al become all detectable. In the next update the ion beam will be taken out to atmosphere at the TES beam-line, the Be sheet that blocks the ions from entering the cryostat can be omitted with a help of polycapillary X-ray optics. This will make the detection of elements lighter than Al possible (Mg, Na, F). The use of the polycapillary optics will also increase the flux at the detector by focusing the emitted X-rays and basically circumventing the $1/r^2$ X-ray flux decrease.

A general purpose calibration sample was also fabricated in the NSC cleanroom. The materials were electron beam evaporated and the chosen materials were Ge (300nm), Cu (147 nm), Cr (72 nm) and Ti (65 nm) on a Si substrate,

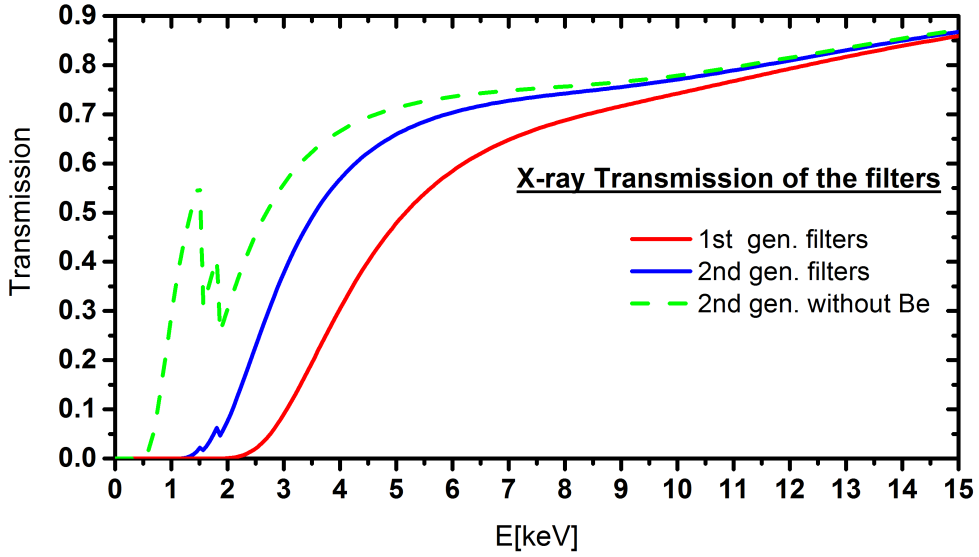

Figure 6.10: Comparison between 1st generation (red) and 2nd generation (blue) filters. Also the 2nd gen. filter without the Be sheet is plotted (green).

so that their characteristic X-rays would cover a wide energy range (1–11 keV). The thickness' of the elements were chosen so that the X-ray production from each element would be on the same order of magnitude for each element. The fluorescence yields and X-ray production cross sections to calculate the thicknesses were taken from Ref. [102]. In Fig. 6.11 we show the peak height spectrum of the calibration sample.

Also a retractable radioactive ^{55}Fe source holder was build inside the measurement chamber. The purpose of this source is to act as a reference during a measurement. Later in the analysis the Mn Kα can be used as a gain drift correction reference as well as a calibration point. The source can be turned away from outside of the chamber by pulling it inside an Al cage. This way the tuning of the SQUIDs and the noise measurements that are needed for each detector prior a measurement can be done without the radioactive source interfering with them. In Fig. 6.12 some details of the measurement system are shown.

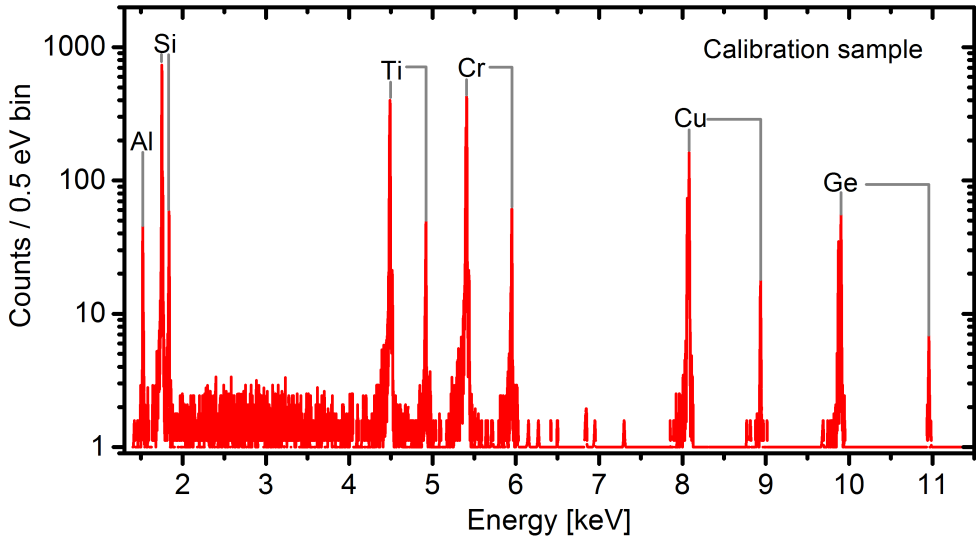

Figure 6.11: Energy spectrum of the calibration sample. Data from one pixel and with 2 MeV protons. The Al excitation is probably from the IR-filters coating.

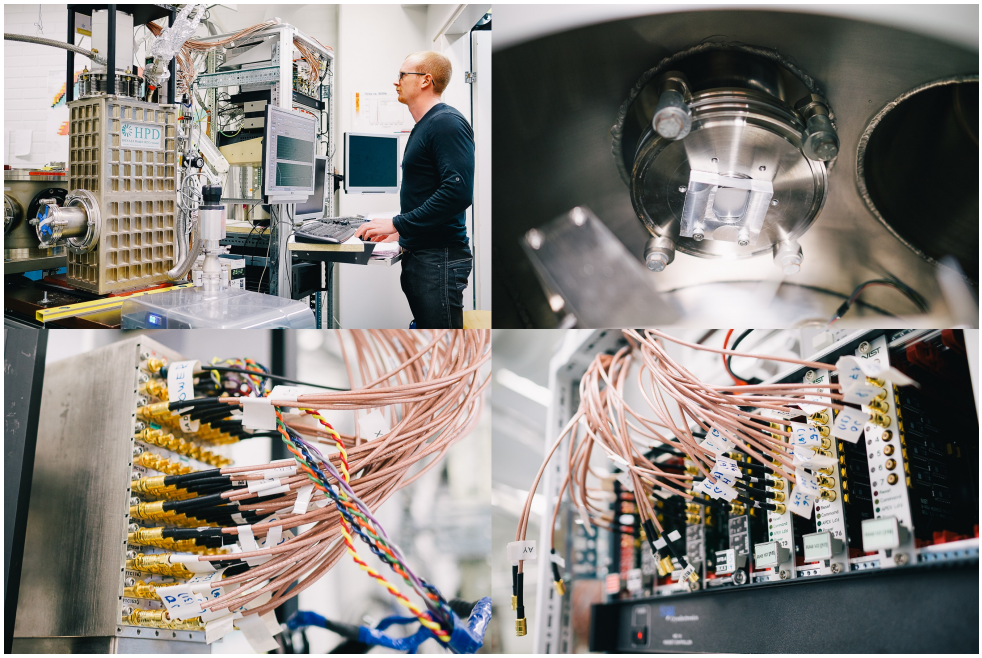

Figure 6.12: Top-left: measurement setup being operated. Top-right: a photograph from inside the measurement chamber showing also the Be-filter at the end of the snout. Bottom-left: The readout tower and its SMB cables. Bottom-right: A photograph of the electronics crate and the magnet controller unit.

6.2 Data Collection and Analysis

6.2.1 The Read Out

The SQUID system used in our detector setup is TDM based and it is designed and constructed at NIST Boulder in the Quantum Devices Group [103]. The basic working principle is that the circuit for each pixel is inductively coupled to a first stage SQUID that can be switched on or off. A second stage SQUID is inductively coupled to summing circuit of all the first stage SQUIDs. By turning the first stage SQUIDS on sequentially, each pixel is read one by one during one time frame. The signal from the second stage SQUID is then amplified by a SQUID array that sits at 3 K, after which the signal is sent to room temperature electronics through more amplification. The digitized data is finally written at the CPU.

6.2.2 Analysis of the Data

For the analysis of the data produced by the TES readout we have used two methods. A commercial Igor Pro technical graphing and data analysis software by Wavemetrics inc. was used. It has macros developed at NIST Boulder that are suitable for analysis and graphing of the digitized data. This method is suitable for analyzing data from a single pixel, but it becomes exhaustively tedious to analyze data from multiple pixels. For this reason a Python based software called Mass has been developed at NIST by Dr. Joe Fowler. Mass removes the need for doing all the steps by hand and lets the computer do the work. During the analysis of the data presented in this thesis, both methods were used in parallel to ensure that the analysis had been done correctly. As the number of pixels will be increased to full 160 pixels and now that we are comfortable using the Mass, we will be shifting solely to it in the future. The analysis procedure for both methods is nevertheless quite the same and the main steps in the analysis will be covered next.

First, non-ideal events need to be cut from the data. These events might be pile-up pulses, pulses that have had a pulse in the pre-trigger or pulses that are distorted for some other reason due to SQUID readout problems, for example. There are many ways to single out the good data. These include checking that the prepulse is stable and has low enough standard deviation, removing all pulses that have abnormally high peak time in the event window meaning a pile-up. One way is to plot the pulse height vs. the pulse area as in Fig. 6.13.

After the cuts, usually about 20–50% of the data is omitted, mostly depending on the number of pile-up events. Of course, there still is information in the pile-up pulses and work is being done and algorithms being coded to analyze heavy pile-up data [104]. The amount of pile-up can be controlled by tuning the X-ray flux and the record length, which is the time that is recorded when a event is registered. By increasing the record length also the energy resolution

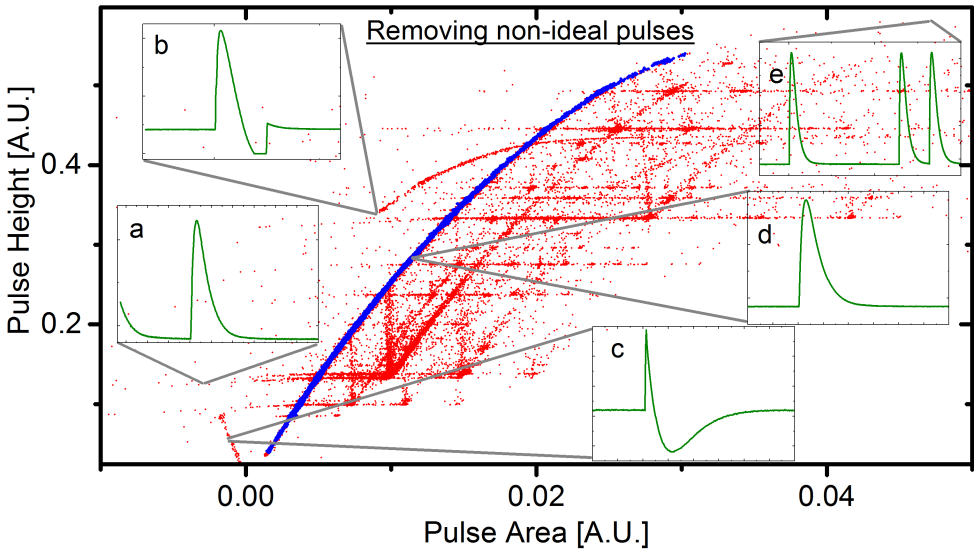

Figure 6.13: Pulse height as a function of pulse area. The good data lies in the main blue line and the red events outside it are cut off. The insets show examples of non-ideal pulses: a) previous event still visible in the prepulse, b) and c) show problems with SQUID locking, d) is a good pulse and e) shows three pulses in the event window – a pile-up. For a linear detector the blue line would be straight.

gets better in a multiplexed system [105], but there always is a trade-off between data collection time and number of pile-up events. In Igor software, these cuts are done by hand, but in Mass these are done by algorithms meaning a lot faster analysis time. For the NIST 160 pixel X-ray array the highest count rate for a single pixel for 10 keV photons is around 9 Hz meaning a total maximum count rate above 1 kHz. A total count rate for a 256 pixel γ-ray TES array of 1.25 kHz has been reported [106].

After the cuts have been made, an average pulse shape is calculated from the collected data. Next, optimal filtering is applied to the raw pulses by using the calculated average pulse and a noise spectrum that has been obtained during the measurement, but without any pulses. Optimal (or Wiener) filter theory presupposes that a signal obeys scaling such that [107] $S = Ha(t)$, where S is the signal, $a(t)$ is an energy independent pulse shape of unit height (or integral), and H is proportional to the pulse height (or integral of the signal). The filter is optimal as long as the signal shape is not a function of energy and both the signal and the noise don't vary in time. If the pulse shape is a function of energy the filtering has to be made in steps [107]. The optimal filtering minimizes the mean square error between the estimated random process and the desired process. An optimal template function is computed from the noise spectrum and the pulse average and this template is convolved with each X-ray pulse record. The maximum of this convolution is the best estimate of the pulse

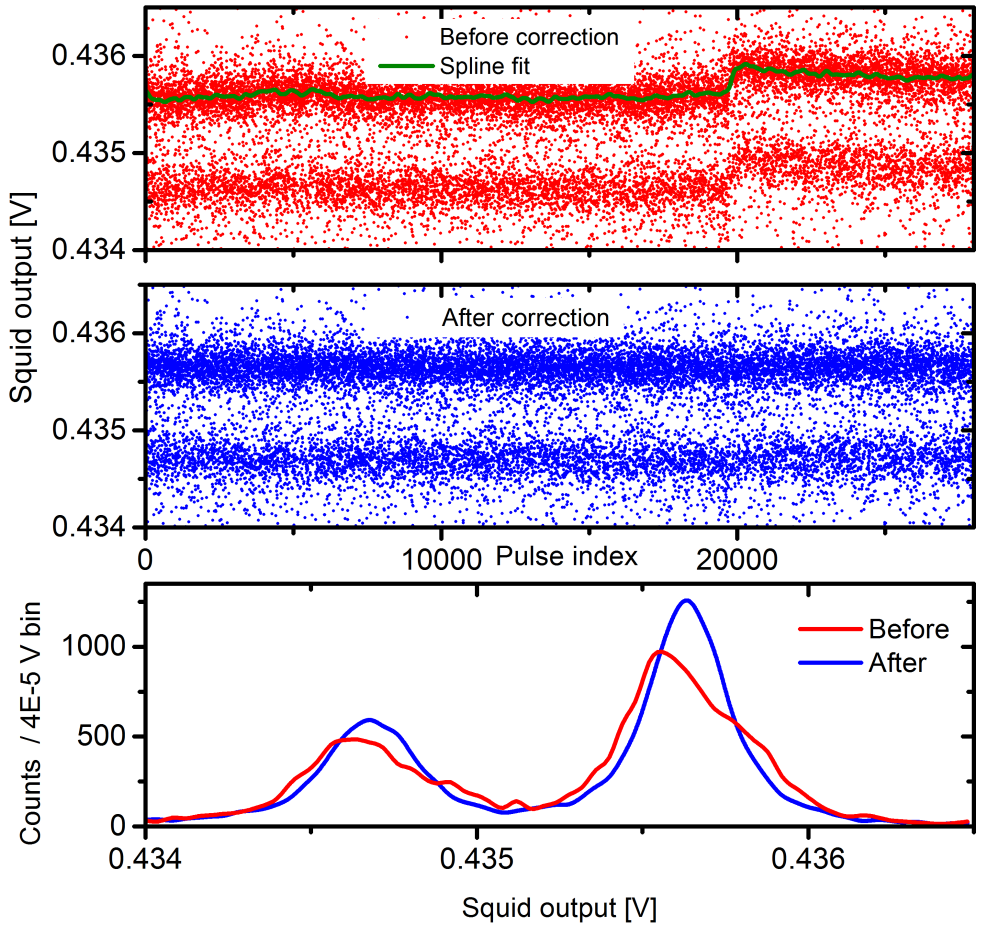

Figure 6.14: Drift correction after optimal filtering and its effect on uncalibrated Cu Kα (around 8 keV) complex histogram.

height [108], which corresponds to the energy of the incident photon.

After the optimal filtering, a drift correction is often needed for some of the pixels. This means that sudden jumps or overall creep as a function of time are corrected (Fig. 6.14). This gain correction is usually done to a monochromatic X-ray line near the center of the dynamic range.

When the drift correction has been done, the SQUID output voltage is converted into energy. This energy calibration needs to be done to each pixel separately as the calibration differs for each measurement, due to the non-linear nature of the TES, the biasing of the detector and the SQUID readout, as can be seen in Fig. 6.15. A polynomial energy calibration is not sufficient because even less than 1 eV energy differences in the peak position will produce distortions to the peak shapes and it will also degrade the energy resolution. A cubic spline calibration is needed.

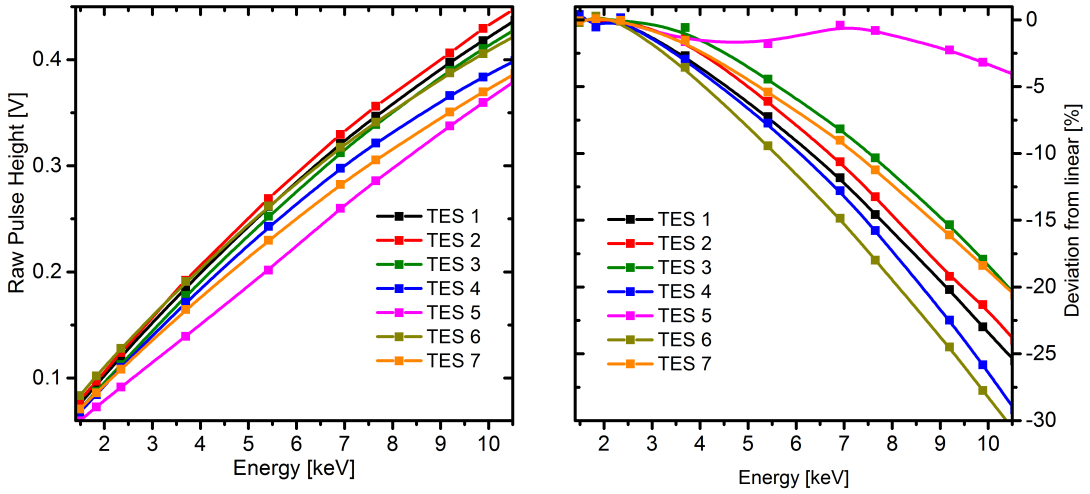

Figure 6.15: Measured non-linear behavior of few TES detectors. Left: Raw pulse height as a function of photon energy. Right: amount of non-linearity compared to a line fitted at low energy.

6.3 PIXE Experiments and Results

In article A.II. the main results of the first proof of principle measurements are reported. The resolution of the detectors were tested with a radioactive ^{55}Fe source. ^{55}Fe decays via electron capture, where a nucleus absorbs an inner atomic electron changing a nuclear proton to a neutron and emitting an electron neutrino [109]. The Fe decays into Mn in an ionized state that will then emit characteristic X-rays of Mn. The instrumental FWHM energy resolution after subtraction of the natural line shape and width of the emission for the best detector was 3.06 eV. This is within a few percent of the expected resolution calculated from the measured average signal and noise. From the nine pixels that gave good data the arithmetic mean resolution was 3.8 $\pm$ 0.6 eV. Under the TES detector there is a coil that could be used to optimize the magnetic field at the array, but no such field optimization was done.

To compare how the spectrum from the radioactive source differs from a spectrum obtained with PIXE, a thin sheet of Mn was measured with 2 MeV protons (The same energy for protons was used in all of the measurements unless stated otherwise). The count rate in both measurements was about 8 Hz. The comparison of the spectra is in Fig. 6.16. The inset of the graph shows the spectra in logarithmic scale, where a satellite peak next to Kα_1 on higher energy side can be seen. This is produced by multiple ionization during proton bombardment of the sample [110]. The FWHM energy resolution of the combined ^{55}Fe spectrum was 3.75 eV compared to the 4.45 eV in the Mn PIXE spectrum. So there was almost 1 eV broadening of the FWHM in the PIXE case. The cause of the broadening is not yet fully understood and it needs more investigation and

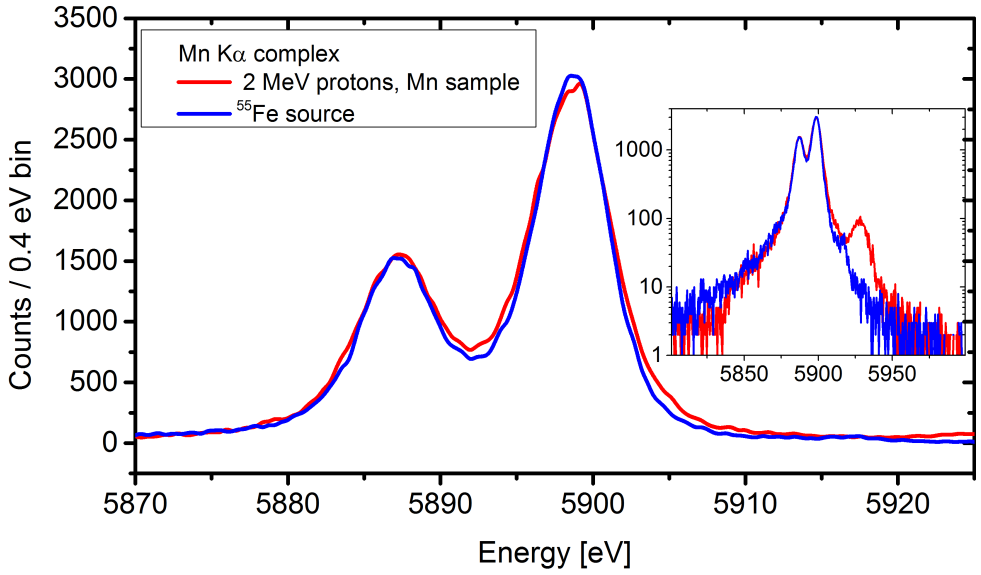

Figure 6.16: A comparison of the Mn Kα complex spectrum produced by PIXE and the ^{55}Fe source. Data from 9 pixels in both spectra.

modeling.

To compare the SDD and TES detectors a bulk copper sample was measured. The results are shown in Fig. 6.17. The improvement in energy resolution is obvious.

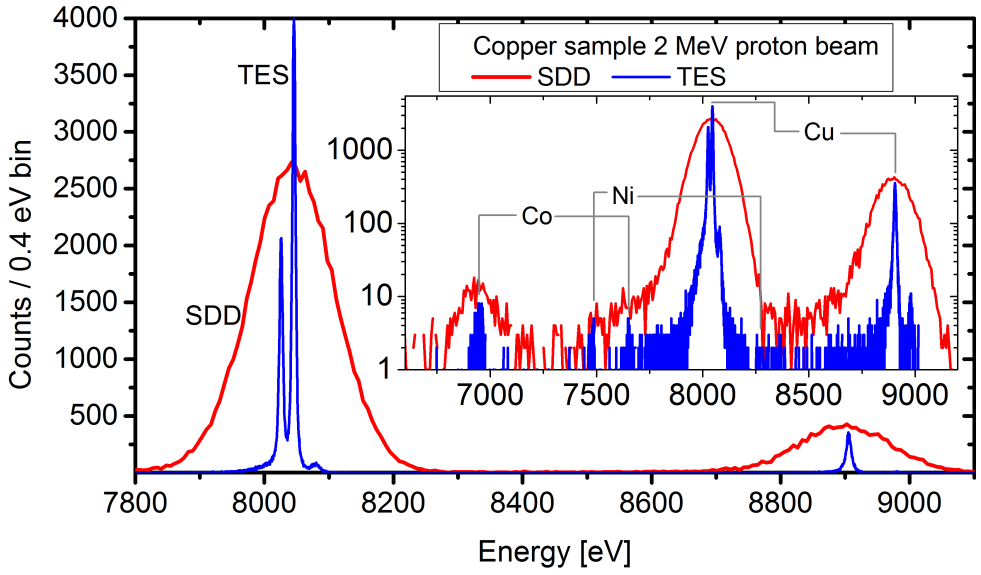

Figure 6.17: A comparison of SDD and TES spectra from a Cu sample. Bin width for TES histogram was 0.4 eV and for SDD 7 eV.

A bulk stainless steel sample was also measured to demonstrate the TES ability to distinguish peaks that are close in energy (Fig. 6.18).

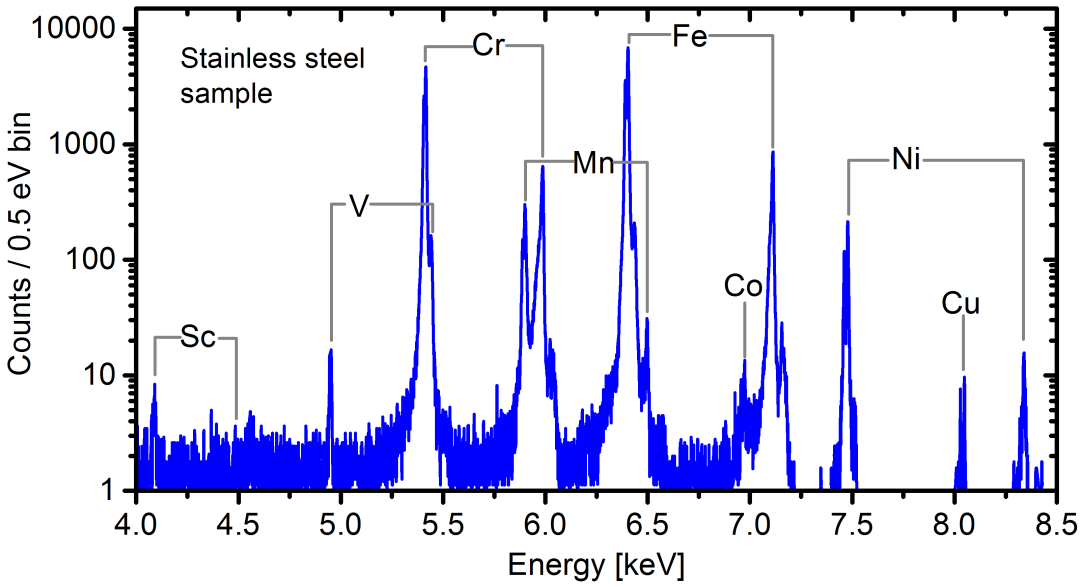

Figure 6.18: Measured spectrum for first multi element sample with TES-PIXE.

After the changes made to the measurement setup described in section 6.1.3 it was soon realized that due to the finicky nature of our outdated power supply for the crate that controls all the feedback and row address cards the system could only be run stably with 3×20 rows meaning 60 pixels in total. In article A.IV. the main results done with the upgraded setup are reported. Since then, we have received an updated readout room temperature electronics from NIST and the system will be in full scale 160 pixel operation in the near future.

6.3.1 Efficiency of the Detectors

A NIST reference sample SRM-611 (impurities in glass) and SRM-1157 (stainless steel) were measured in order to calibrate the efficiency of the TES detector as a function of energy. The spectrum of the SRM-611 is in Fig. 6.19.

As we know the composition of the reference samples, we could find out the detector efficiency from the measured spectra. The efficiency is crucial to know, if quantitative data is required from a PIXE analysis. To find out the detector efficiency, the measured data was analyzed using GUPIXwin software, which calculates the elemental concentrations based on the known physical parameters of the setup, after converting it from digital pulses to channel data. In GUPIXwin analysis, external filters were taken into account but the to-be-determined intrinsic detector efficiency was temporarily set to 1. For the SRM 611 sample, the nominal matrix composition in mass percentage was 72 % SiO_2, 14 % Na_2O,

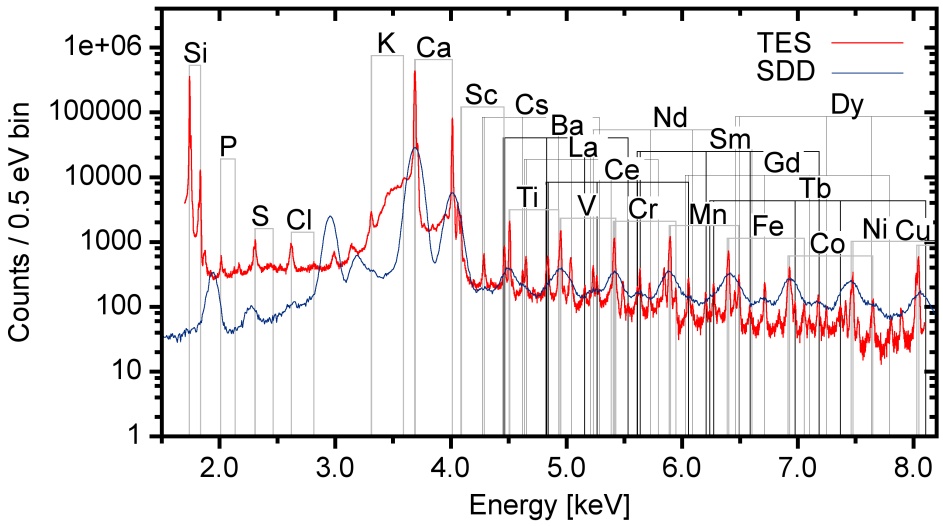

Figure 6.19: Measured peak height spectrum with TES and SDD of the NIST SRM-611 reference sample.

12 % CaO and 2 % Al_2O_3 according to the NIST certificate and it was used in the GUPIXwin analysis. For the SRM 1157 sample, the matrix composition (consisting mostly of iron) was iterated by the GUPIXwin.

We did not use the standard fitting procedures of the program; instead, the peak areas were integrated after the continuous background was removed by a visual fit. Then, the concentrations (without the TES efficiency) were calculated using the X-ray yields that GUPIXwin had calculated. Finally, the detector efficiency was calculated as the ratio between the measured concentration without the detector efficiency, and the known reference concentration, for all reference energies. In the analysis, statistical uncertainties and uncertainties in the ionization cross-sections for K-lines (17 %) [111] and L-lines (5%) [112] were taken into account. The reference values for the concentrations and energies of the analyzed elements were taken from Ref. [113] for SRM 611 and from the NIST certificate for the SRM 1157 sample.

In Fig. 6.20 we also show the simulated efficiency curve consisting of vacuum window transmission and bismuth absorption (calculated using reference [114]). The red and blue dots represent the analyzed efficiency values for SRM 611 and SRM 1157 references, respectively. It can be noted that the experimental values agree well with the theory with a few exceptions. Firstly at the lowest energy, the Al Kα peak deviated clearly from the theoretical curve and it is not shown in the graph. The efficiency value for the Al was 258 % $\pm$ 28%. This can be explained by the fact that the reference sample consisted mostly of SiO_2 and thus there are plenty of Si Kα X-rays hitting the Al filters in front of the detector. Since Si Kα is very efficient in causing fluorescence X-rays in Al, we will see a lot more Al X-rays than would be expected to come just from the

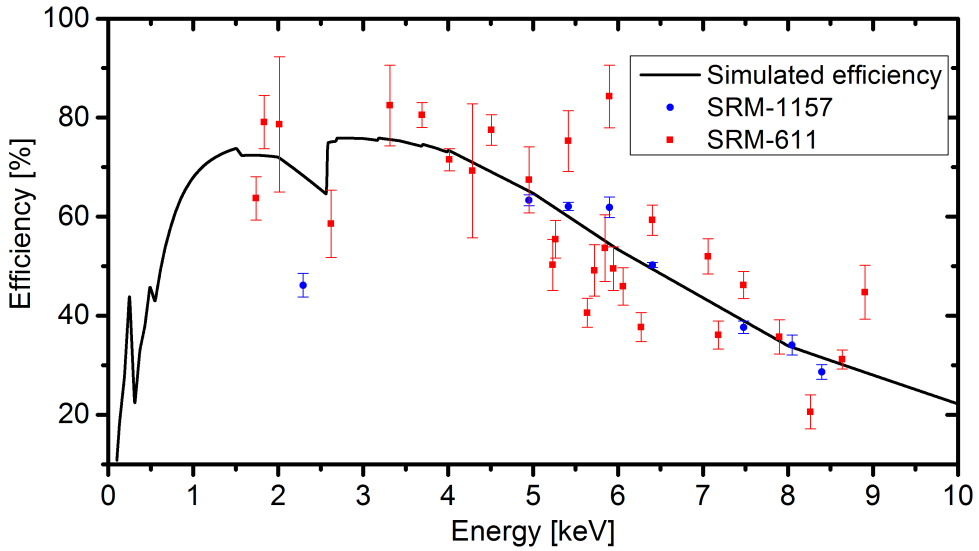

Figure 6.20: Measured and simulated efficiency of the TES-array. The efficiency curve was calibrated using a known reference materials (NIST SRM 611 and NIST SRM 1157). The absorber material in our TES-detector is bismuth, and the vacuum window used in the front of the detector is AP3.3 window that is included in the simulated efficiency. The nominal thickness of Bi absorber is 2.5 µm. The statistical error bars for the SRM 611 data points are greater, because there were fewer events per element as the sample has many more elements than the SRM 1157 sample. The total number of events in both spectra were similar.

sample. Another deviating peak is the Cu Kα. The efficiency value for Cu was (135 $\pm$ 8) %. The expected concentration of Cu in the sample is small, only (430.3 $\pm$ 23.6) ppm so the flux of the Cu Kα X-rays originated from the sample is very small. Thus it can be easily deducted that even a small alternative source of Cu Kα will interfere the analysis. This alternative source of Cu X-rays is very likely the Cu layer that is in TES underneath the Bi absorber. It should be also noted that the theoretical efficiency never reaches level higher than 77 % below 10 keV energies. This is due to the fact that a thick silicon grid with 77 % hole area is under the polymer that holds the vacuum.

A simple measurement to probe the origin of the excess measured Al and Cu X-rays is planned for near future. A broadband X-ray tube source is going to be used as an X-ray source. If we then see characteristic Al and Cu excitations we know that they originate from the detector and the IR-filters, which is the assumption.

6.3.2 Pigment Measurements

Three different pigment samples (lead red, lead white, and cobalt blue) were also studied to see how much impurities there are in commercial pigments. Studying

pigments in art is one application for PIXE when detecting possible forgeries [115]. The pigment powders were pressed into pellets that could be mounted in the sample chamber. A bulk lead sample was also used as a reference for the Pb pigments (Fig. 6.21). The lead white pigment has much more impurities than lead red (Ca, Ti, Ba, Fe, Ni,). Again, with a TES *e.g.* Ba L-shell excitations can be resolved that are not resolved with a SDD.

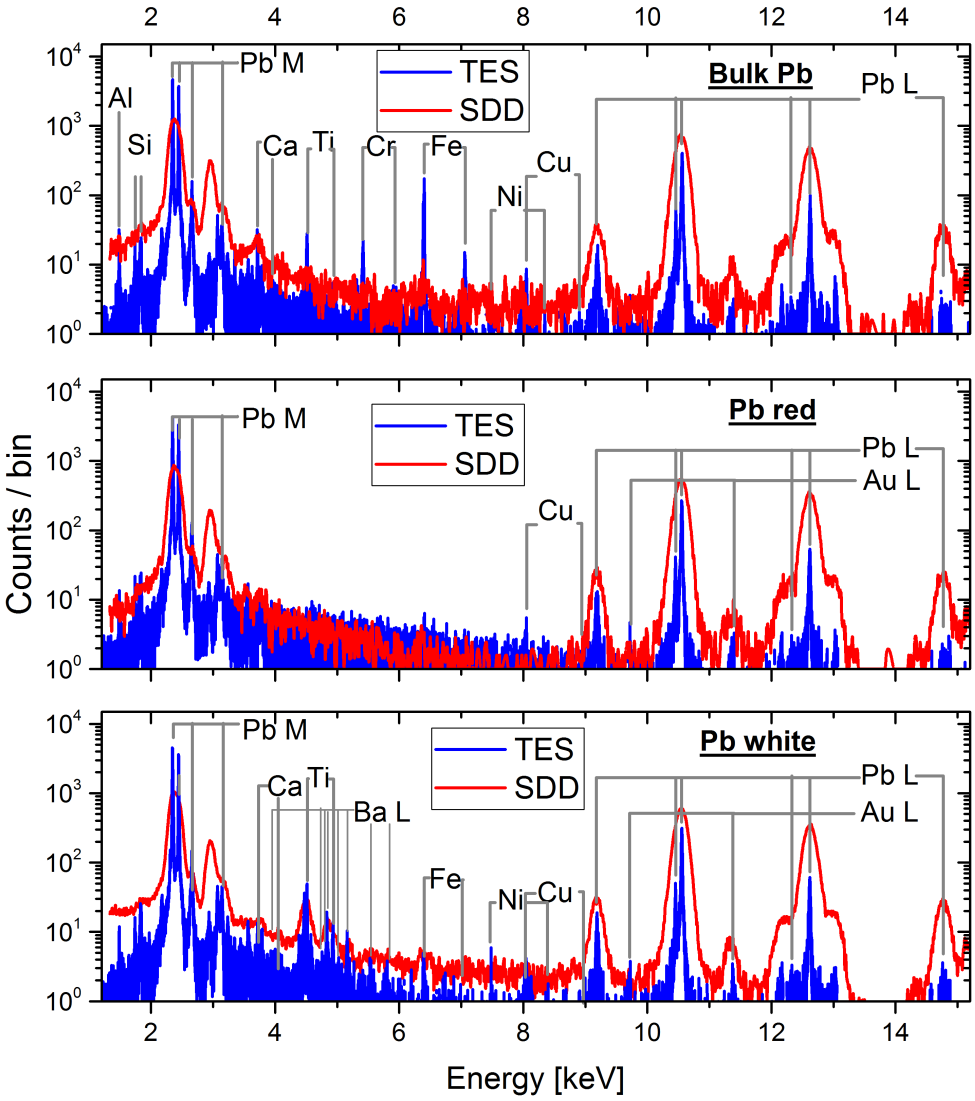

Figure 6.21: Lead pigments. Bin width for TES was 0.5 eV and 5 eV for SDD.

A pressed cobalt blue pigment sample was also measured to demonstrate the power of a TES detector over a SDD. Spectra of the cobalt blue is in Fig. 6.22, where the two detectors are compared. In the TES spectrum *e.g.* the Fe impurity can be differentiated from the Mn unlike with the SDD. By using the obtained efficiency curve the concentrations for impurities could be estimated.

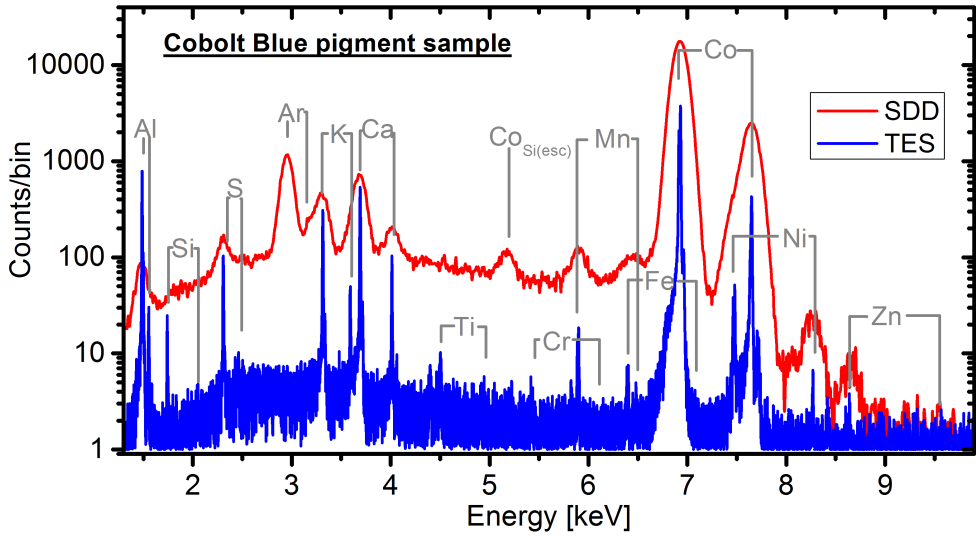

Figure 6.22: Spectra from the SDD (dotted red line) and TES (solid blue line) detectors. The bin width for TES was 0.5 eV and for the SDD 7 eV.

The level of impurities in the Co sample were measured to be (290 ± 60) ppm of Ti and (110 ± 40) ppm of Cr for example.

6.3.3 Chemical Shifts

The chemical state of an element (oxidation number, chemical bonding) influences its electronic transitions and atomic energy levels, even those of the inner shells of the atoms. Four kinds of effects have been observed that influence X-ray transitions: energy shifts of the characteristic X-ray lines, the alteration of X-ray relative intensity ratios and line shapes, and satellite peak formation [116]. The size of the chemical shift is usually in the eV range. For example for Fe compounds the amount of the shifts measured is between –2 eV to +2 eV depending on the ligand and the biggest shift is for halogen compounds [117].

To test if we can see the chemical environment of a sample, three titanium compounds were fabricated. A 500 nm TiN sample and a 450 nm TiO_2 sample were fabricated with ALD[2] and a 400 nm Ti was electron-beam evaporated in ultra-high vacuum conditions. All of the samples had a Si substrate. The samples were measured in an order of Ti–TiN–Ti–TiO_2–Ti, and the energy calibration of the spectra was done on the combined Ti spectrum through the whole measurement time. The reason why the Ti sample was measured before and after both TiN and TiO_2 was to ensure that the calibration stayed the same during the whole measurement. A possible energy drift was corrected on the Si Kα line that was common in all of the samples.

A Gaussian function was fitted to the spectra of the Ti samples Kα complex

[2]Dr. Jari Malm fabricated the ALD samples.

for each pixel. A standard deviation of 0.3 eV for the position of the complex was obtained across the pixels. In Fig. 6.23 we show parts of the spectra from the three samples. A chemical shift of 1.1 eV was seen on the Kα complex of the TiO_2 sample compared to the pure Ti sample and a 1.0 eV shift was seen in the Kβ. No shifts were seen in the TiN spectrum. The shifts were determined by fitting a Gaussian function on the Kα and Kβ peaks. X-ray photoelectron spectroscopy measurements [118] and wave dispersion spectrometer measurements [119] agree with these results.

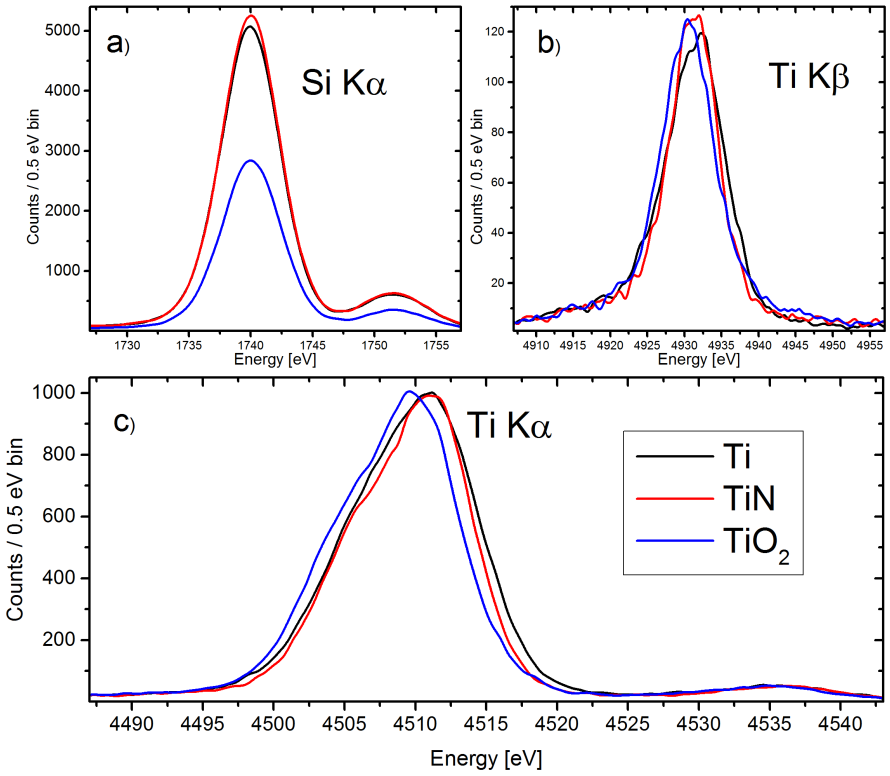

Figure 6.23: Spectra from the three different Ti-samples normalized for the Ti Kα peak area. The spectra are split to three regions for visual reasons. a) the Si Kα, b) The Ti Kβ, c) the Ti Kα .

The Kβ/Kα intensity ratios were (12.5 $\pm$ 0.1) % for Ti, (13.1 $\pm$ 0.2) % for TiN, and (13.31 $\pm$ 0.2) % for TiO_2. The Kα satellite intensity compared to the total Ti emission was (4.9 $\pm$ 0.1) % for Ti, (5.0 $\pm$ 0.1) % for TiN and (4.8 $\pm$ 0.1) % for TiO_2. The satellite peak next to the Kα emission is generated during the ion bombardment when 1s and 2p vacancies are created simultaneously and a shake process occurs [120]. The 2p vacancy has a relatively long life-time compared to that of the 1s vacancy. When the inner vacancy de-excites in the presence of this spectator hole, there is a change in the electrostatic potential leading to shifts in the energy levels, affecting as a result to the energy of the photon emitted [110].

Chapter 7

Summary and Future Prospects

In this thesis the development of a TES array from design to characterization has been presented. Also the thermal models describing the detectors have been probed theoretically and experimentally.

A working fabrication procedure for 256 pixel TES array was developed for detectors to be used in X-ray material characterization. This information can be used in possible future projects, where fabrication of superconducting X-ray detector arrays are needed. The uniformity of the arrays left some room for improvement for possible next fabrication iterations. Work is still to be done in the characterization as only one array with the biggest heat capacity was used in X-ray measurements.

The development of the measurement setup, where TES detectors are used in PIXE experiments was also presented. From the initial 12 pixel proof of principle setup to the 60 pixel setup with better filters capable of actual measurements with reasonable measurement times was shown. The TES setup is unique in the field of PIXE and it has raised much curiosity in the field, mainly because of its energy dispersive nature and the excellent energy resolution reported also in this thesis.

TES-PIXE has only just seen its daylight and actual measurements in the field of material science and art restoration are just starting. The new setup also opens possibilities to study new physics in the field of ion beam X-ray science.

Upgrade for the outdated power supply that was limiting the number of pixels will be installed shortly. Then we will have a full scale operation finally at hand. With count rates near the kHz range the TES becomes competitive with the SDD detector in regards of measurement times. This is also crucial for sensitive samples when the exposure to the ion beam needs to be minimized. A new beam line is also under development that will have the option to use external ion beam with TES-PIXE. This will make the analysis of big or vacuum delicate samples possible. New X-ray optics that will be installed soon will not only make smaller ion doses possible, but it will also act as an ion filter. This will make lighter than Al elements detectable.

References

[1] Röntgen, W. C. *Ueber eine neue art von strahlen.* Annalen der Physik, **300**, 1 (1898).

[2] Warren, B. *X-ray Diffraction.* Addison-Wesley series in metallurgy and materials engineering. Dover Publications (1969).

[3] Filipponi, A., Di Cicco, A., and Natoli, C. R. *X-ray-absorption spectroscopy and n-body distribution functions in condensed matter. i. theory.* Phys. Rev. B, **52**, 15122 (1995).

[4] Moseley, H. G. J. *The high frequency spectra of the elements.* Phil. Mag. p. 1024 (1913).

[5] Johansson, T., Akselsson, R., and Johansson, S. *X-ray analysis: Elemental trace analysis at the 10^{-12} g level.* Nuclear Instruments and Methods, **84**, 141 (1970).

[6] Yu, K. M., Walukiewicz, W., Wojtowicz, T., Kuryliszyn, I., Liu, X., Sasaki, Y., and Furdyna, J. K. *Effect of the location of Mn sites in ferromagnetic $Ga_{1-x}Mn_xAs$ on its curie temperature.* Phys. Rev. B, **65**, 201303 (2002).

[7] Moretto, P., Llabador, Y., Simonoff, M., Razafindrabe, L., Bara, M., and Guiet-Bara, A. *Quantitative mapping of intracellular cations in the human amniotic membrane.* Nuclear Instruments and Methods in Physics Research Section B: Beam Interactions with Materials and Atoms, **77**, 275 (1993).

[8] Murao, S., Sie, S. H., Hamasaki, S., Maglambayan, V. B., and Hu, X. *Application of micro-PIXE method to ore geology.* AIP Conference Proceedings, **475**, 464 (1999).

[9] Tang, S. M., Tang, S. H., Tay, T. S., and Retty, A. T. *Analysis of Burmese and Thai rubies by PIXE.* Appl. Spectrosc., **42**, 44 (1988).

[10] Grassi, N., Bonanni, P., Mazzotta, C., Migliori, A., and Mand, P. A. *PIXE analysis of a painting by Giorgio Vasari.* X-Ray Spectrometry, **38**, 301 (2009).

[11] Johansson, S. A. *PIXE: a novel technique for elemental analysis.* Endeavour, **13**, 48 (1989).

[12] Kamerlingh-Onnes, H. *The superconductivity of mercury.* Comm. Phys. Lab. Univ. Leiden, pp. 48 – 53 (1911).

[13] Meissner, W. and Ochsenfeld, R. *Ein neuer effekt bei eintritt der supraleitfhigkeit.* Naturwissenschaften, **21**, 787 (1933).

[14] Andrews, D. H., Brucksch, W. F., Ziegler, W. T., and Blanchard, E. R. *Attenuated superconductors i. for measuring infra-red radiation.* Review of Scientific Instruments, **13**, 281 (1942).

[15] Ade, P. A. R., Aikin, R. W., Barkats, D., Benton, S. J., Bischoff, C. A., Bock, J. J., Brevik, J. A., Buder, I., Bullock, E., Dowell, C. D., Duband, L., Filippini, J. P., Fliescher, S., Golwala, S. R., Halpern, M., Hasselfield, M., Hildebrandt, S. R., Hilton, G. C., Hristov, V. V., Irwin, K. D., Karkare, K. S., Kaufman, J. P., Keating, B. G., Kernasovskiy, S. A., Kovac, J. M., Kuo, C. L., Leitch, E. M., Lueker, M., Mason, P., Netterfield, C. B., Nguyen, H. T., O'Brient, R., Ogburn, R. W., Orlando, A., Pryke, C., Reintsema, C. D., Richter, S., Schwarz, R., Sheehy, C. D., Staniszewski, Z. K., Sudiwala, R. V., Teply, G. P., Tolan, J. E., Turner, A. D., Vieregg, A. G., Wong, C. L., and Yoon, K. W. *Detection of b-mode polarization at degree angular scales by BICEP2.* Phys. Rev. Lett., **112**, 241101 (2014).

[16] Ahmed, Z., Amiri, M., Benton, S. J., Bock, J. J., Bowens-Rubin, R., Buder, I., Bullock, E., Connors, J., Filippini, J. P., Grayson, J. A., Halpern, M., Hilton, G. C., Hristov, V. V., Hui, H., Irwin, K. D., Kang, J., Karkare, K. S., Karpel, E., Kovac, J. M., Kuo, C. L., Netterfield, C. B., Nguyen, H. T., O'Brient, R., Ogburn, R. W., Pryke, C., Reintsema, C. D., Richter, S., Thompson, K. L., Turner, A. D., Vieregg, A. G., Wu, W. L. K., and Yoon, K. W. *BICEP3: a 95ghz refracting telescope for degree-scale CMB polarization.* Proc. SPIE, **9153**, 91531N (2014).

[17] Tomaru, T., Hazumi, M., Lee, A. T., Ade, P., Arnold, K., Barron, D., Borrill, J., Chapman, S., Chinone, Y., Dobbs, M., Errard, J., Fabbian, G., Ghribi, A., Grainger, W., Halverson, N., Hasegawa, M., Hattori, K., Holzapfel, W. L., Inoue, Y., Ishii, S., Kaneko, Y., Keating, B., Kermish, Z., Kimura, N., Kisner, T., Kranz, W., Matsuda, F., Matsumura, T., Morii, H., Myers, M. J., Nishino, H., Okamura, T., Quealy, E., Reichardt, C. L., Richards, P. L., Rosen, D., Ross, C., Shimizu, A., Sholl, M.,

Siritanasak, P., Smith, P., Stebor, N., Stompor, R., Suzuki, A., Suzuki, J.-i., Takada, S., Tanaka, K.-i., and Zahn, O. *The POLARBEAR-2 experiment.* Proc. SPIE, **8452**, 84521H (2012).

[18] Holland, W. S., Bintley, D., Chapin, E. L., Chrysostomou, A., Davis, G. R., Dempsey, J. T., Duncan, W. D., Fich, M., Friberg, P., Halpern, M., Irwin, K. D., Jenness, T., Kelly, B. D., MacIntosh, M. J., Robson, E. I., Scott, D., Ade, P. A. R., Atad-Ettedgui, E., Berry, D. S., Craig, S. C., Gao, X., Gibb, A. G., Hilton, G. C., Hollister, M. I., Kycia, J. B., Lunney, D. W., McGregor, H., Montgomery, D., Parkes, W., Tilanus, R. P. J., Ullom, J. N., Walther, C. A., Walton, A. J., Woodcraft, A. L., Amiri, M., Atkinson, D., Burger, B., Chuter, T., Coulson, I. M., Doriese, W. B., Dunare, C., Economou, F., Niemack, M. D., Parsons, H. A. L., Reintsema, C. D., Sibthorpe, B., Smail, I., Sudiwala, R., and Thomas, H. S. *SCUBA-2: the 10 000 pixel bolometer camera on the James Clerk Maxwell Telescope.* Monthly Notices of the Royal Astronomical Society, **430**, 2513 (2013).

[19] WOLLMAN, D. A., IRWIN, K. D., HILTON, G. C., DULCIE, L. L., NEWBURY, D. E., and MARTINIS, J. M. *High-resolution, energy-dispersive microcalorimeter spectrometer for X-ray microanalysis.* Journal of Microscopy, **188**, 196 (1997).

[20] Miller, A. J., Nam, S. W., Martinis, J. M., and Sergienko, A. V. *Demonstration of a low-noise near-infrared photon counter with multiphoton discrimination.* Applied Physics Letters, **83**, 791 (2003).

[21] Hoover, A., Winkler, R., Rabin, M., Vo, D., Ullom, J., Bennett, D., Doriese, W., Fowler, J., Horansky, R., Schmidt, D., Vale, L., and Schaffer, K. *Determination of plutonium isotopic content by microcalorimeter gamma-ray spectroscopy.* Nuclear Science, IEEE Transactions on, **60**, 681 (2013).

[22] Engle, J., Birnbaum, E., Trellue, H., John, K., Rabin, M., and Nortier, F. *Evaluation of ^{163}Ho production options for neutrino mass measurements with microcalorimeter detectors.* Nuclear Instruments and Methods in Physics Research Section B: Beam Interactions with Materials and Atoms, **311**, 131 (2013).

[23] Uhlig, J., Fullagar, W., Ullom, J. N., Doriese, W. B., Fowler, J. W., Swetz, D. S., Gador, N., Canton, S. E., Kinnunen, K., Maasilta, I. J., Reintsema, C. D., Bennett, D. A., Vale, L. R., Hilton, G. C., Irwin, K. D., Schmidt, D. R., and Sundström, V. *Table-top ultrafast X-ray microcalorimeter spectrometry for molecular structure.* Phys. Rev. Lett., **110**, 138302 (2013).

[24] Enss, C. *Cryogenic Particle Detection.* Topics in Applied Physics. Springer (2005).

[25] Irwin, K. D., Hilton, G. C., Wollman, D. A., and Martinis, J. M. *Thermal-response time of superconducting transition-edge microcalorimeters.* Journal of Applied Physics, **83**, 3978 (1998).

[26] Figueroa-Feliciano, E. *Theory and development of position-sensitive quantum calorimeters.* Ph.D. thesis, Stanford University (2001).

[27] Peebles, P. and Giuma, T. *Principles of electrical engineering.* McGraw-Hill series in electrical engineering: Introductory. McGraw-Hill (1991).

[28] Irwin, K. D. *Phonon–mediated particle detection using superconducting tungsten transition–edge sensors.* Ph.D. thesis, Stanford University (1995).

[29] Lindeman, M. A. *Microcalorimetry and the transition–edge sensor.* Ph.D. thesis, University of California at Davis (2000).

[30] Lindeman, M. A., Bandler, S., Brekosky, R. P., Chervenak, J. A., Figueroa-Feliciano, E., Finkbeiner, F. M., Li, M. J., and Kilbourne, C. A. *Impedance measurements and modeling of a transition-edge-sensor calorimeter.* Review of Scientific Instruments, **75**, 1283 (2004).

[31] Kinnunen, K. *Studies of transition-edge sensor physics: noise and thermal models.* Ph.D. thesis, University of Jyväskylä (2011).

[32] Irwin, K. *Thermodynamics of nonlinear bolometers near equilibrium.* Nuclear Instruments and Methods in Physics Research Section A: Accelerators, Spectrometers, Detectors and Associated Equipment, **559**, 718 (2006).

[33] Bandler, S., Brekosky, R., Brown, A.-D., Chervenak, J., Figueroa-Feliciano, E., Finkbeiner, F., Iyomoto, N., Kelley, R., Kilbourne, C., Porter, F., Sadleir, J., and Smith, S. *Performance of TES X-ray microcalorimeters with a novel absorber sesign.* Journal of Low Temperature Physics, **151**, 400 (2008).

[34] Tinkham, M. *Introduction to Superconductivity.* McGraw-Hill (1996).

[35] Day, P. K., LeDuc, H. G., Mazin, B. A., Vayonakis, A., and Zmuidzinas, J. *A broadband superconducting detector suitable for use in large arrays.* Nature, **425**, 817 (2003).

[36] Mazin, B. A. *Microwave kinetic inductance detectors: The first decade.* AIP Conference Proceedings, **1185**, 135 (2009).

[37] Mazin, B. A., Day, P. K., Zmuidzinas, J., and Leduc, H. G. *Multiplexable kinetic inductance detectors.* AIP Conference Proceedings, **605**, 309 (2002).

[38] Mazin, B. A., Day, P. K., Irwin, K. D., Reintsema, C. D., and Zmuidzinas, J. *Digital readouts for large microwave low-temperature detector arrays.* Nuclear Instruments and Methods in Physics Research Section A: Accelerators, Spectrometers, Detectors and Associated Equipment, **559**, 799 (2006).

[39] Josephson, B. D. *The discovery of tunnelling supercurrents.* Rev. Mod. Phys., **46**, 251 (1974).

[40] Ohkubo, M. *Current status of non–equilibrium superconducting detectors for photons and molecules.* AIP Conference Proceedings, **1185**, 381 (2009).

[41] Friedrich, S. *Cryogenic X-ray detectors for synchrotron science.* Journal of Synchrotron Radiation, **13**, 159 (2006).

[42] Porst, J.-P. *Towards MARE: Development of a metallic magnetic calorimeter with superconducting rhenium absorber.* Ph.D. thesis, University of Heidelberg (2007).

[43] Pies, C., Schäfer, S., Heuser, S., Kempf, S., Pabinger, A., Porst, J.-P., Ranitsch, P., Foerster, N., Hengstler, D., Kampkötter, A., Wolf, T., Gastaldo, L., Fleischmann, A., and Enss, C. *maxs: Microcalorimeter arrays for high-resolution X-ray spectroscopy at GSI/FAIR.* Journal of Low Temperature Physics, **167**, 269 (2012).

[44] Hoevers, H. F. C., Bento, A. C., Bruijn, M. P., Gottardi, L., Korevaar, M. A. N., Mels, W. A., and de Korte, P. A. J. *Thermal fluctuation noise in a voltage biased superconducting transition edge thermometer.* Applied Physics Letters, **77**, 4422 (2000).

[45] Maasilta, I. J. and Kinnunen, K. M. *New analysis method for I-V and complex impedance data of transition-edge sensors.* AIP Conference Proceedings, **1185**, 38 (2009).

[46] Zhao, Y., Appel, J., Chervenak, J., Doriese, W., and Staggs, S. *Study of excess heat capacity and suppressed Kapitza conductance in TES devices.* Applied Superconductivity, IEEE Transactions on, **21**, 227 (2011).

[47] Ullom, J., Doriese, W., Hilton, G., Beall, J.-A., Deiker, S., Duncan, W., Ferreira, L., Irwin, K., Reintsema, C., and Vale, L. *Characterization and reduction of unexplained noise in superconducting transition-edge sensors.* Applied Physics Letters, **84**, 4206 (2004).

[48] Maasilta, I. J. *Complex impedance, responsivity and noise of transition-edge sensors: Analytical solutions for two- and three-block thermal models.* AIP Advances, **2**, 042110 (2012).

[49] Bailey, C. A. *Advanced Cryogenics.* Plenum (1971).

[50] London, H., Clarke, G. R., and Mendoza, E. *Osmotic pressure of He^3 in liquid He^4, with proposals for a refrigerator to work below 1°K.* Phys. Rev., **128**, 1992 (1962).

[51] Pobell, F. *Matter and Methods at Low Temperatures.* Springer-Verlag (1996).

[52] Vermeulen, G. and Frossati, G. *Powerful dilution refrigerator for use in the study of polarized liquid ^3He and nuclear cooling.* Cryogenics, **27**, 139 (1987).

[53] Debye, P. *Einige bemerkungen zur magnetisierung bei tiefer temperatur.* Annalen der Physik, **386**, 1154 (1926).

[54] Giauque, W. F. *A thermodynamic treatment of certain magnetic effects. a proposed method of producing temperatures considerably below 1° K absolute.* Journal of the American Chemical Society, **49**, 1864 (1927).

[55] Cohen, D., Edelsack, E. A., and Zimmerman, J. E. *Magnetocardiograms taken inside a shielded room with a superconducting point-contact magnetometer.* Applied Physics Letters, **16**, 278 (1970).

[56] Deaver, B. S. and Fairbank, W. M. *Experimental evidence for quantized flux in superconducting cylinders.* Phys. Rev. Lett., **7**, 43 (1961).

[57] Doll, R. and Näbauer, M. *Experimental proof of magnetic flux quantization in a superconducting ring.* Phys. Rev. Lett., **7**, 51 (1961).

[58] Clarke, J. and Braginski, A. *The SQUID Handbook: Fundamentals and Technology of SQUIDs and SQUID Systems.* nid. 1. Wiley (2006).

[59] Maul, M. K., Strandberg, M. W. P., and Kyhl, R. L. *Excess noise in superconducting bolometers.* Phys. Rev., **182**, 522 (1969).

[60] Clarke, J., Richards, P. L., and Yeh, N.-H. *Composite superconducting transition edge bolometer.* Applied Physics Letters, **30**, 664 (1977).

[61] Young, B., Cabrera, B., Lee, A., Martoff, C., Neuhauser, B., and McVittie, J. *Phonon-mediated detection of X-rays in silicon crystals using superconducting transition edge phonon sensors.* Magnetics, IEEE Transactions on, **25**, 1347 (1989).

[62] Range, S. K. *Investigating Einsteins Spacetime with Gyroscopes*. NASA (2004).

[63] Mussett, A. and Khan, A. *Looking Into the Earth: An Introduction to Geological Geophysics*. Cambridge University Press (2000).

[64] Chervenak, J., Grossman, E., Irwin, K., Martinis, J. M., Reintsema, C., Allen, C., Bergman, D., Moseley, S., and Shafer, R. *Performance of multiplexed SQUID readout for cryogenic sensor arrays*. Nuclear Instruments and Methods in Physics Research Section A: Accelerators, Spectrometers, Detectors and Associated Equipment, **444**, 107 (2000).

[65] Holland, W. S., Duncan, W., Kelly, B. D., Irwin, K. D., Walton, A. J., Ade, P. A. R., and Robson, E. I. *SCUBA-2: a large format submillimeter camera on the James Clerk Maxwell Telescope*. Proc. SPIE, **4855**, 1 (2003).

[66] Bennett, D. A., Horansky, R. D., Schmidt, D. R., Hoover, A. S., Winkler, R., Alpert, B. K., Beall, J. A., Doriese, W. B., Fowler, J. W., Fitzgerald, C. P., Hilton, G. C., Irwin, K. D., Kotsubo, V., Mates, J. A. B., ONeil, G. C., Rabin, M. W., Reintsema, C. D., Schima, F. J., Swetz, D. S., Vale, L. R., and Ullom, J. N. *A high resolution gamma-ray spectrometer based on superconducting microcalorimeters*. Review of Scientific Instruments, **83**, 093113 (2012).

[67] Niemack, M. D., Beyer, J., Cho, H. M., Doriese, W. B., Hilton, G. C., Irwin, K. D., Reintsema, C. D., Schmidt, D. R., Ullom, J. N., and Vale, L. R. *Code-division squid multiplexing*. Applied Physics Letters, **96**, 163509 (2010).

[68] Fowler, J., Doriese, W., Hilton, G., Irwin, K., Schmidt, D., Stiehl, G., Swetz, D., Ullom, J., and Vale, L. *Optimization and analysis of code-division multiplexed TES microcalorimeters*. Journal of Low Temperature Physics, **167**, 713 (2012).

[69] Cunningham, M. F., Ullom, J. N., Miyazaki, T., Labov, S. E., Clarke, J., Lanting, T. M., Lee, A. T., Richards, P. L., Yoon, J., and Spieler, H. *High-resolution operation of frequency-multiplexed transition-edge photon sensors*. Applied Physics Letters, **81**, 159 (2002).

[70] Doriese, W. B., Beall, J. A., Deiker, S., Duncan, W. D., Ferreira, L., Hilton, G. C., Irwin, K. D., Reintsema, C. D., Ullom, J. N., Vale, L. R., and Xu, Y. *Time-division multiplexing of high-resolution X-ray microcalorimeters: Four pixels and beyond*. Applied Physics Letters, **85**, 4762 (2004).

[71] Johansson, S., Campbell, J., and Malmqvist, K. *Particle-Induced X-Ray Emission Spectrometry (PIXE).* Chemical Analysis: A Series of Monographs on Analytical Chemistry and Its Applications. Wiley (1995).

[72] Jenkins, R., Manne, R., Robin, R., and Senemaud, C. *Nomenclature, symbols, units and their usage in spectrochemical analysis - viii. nomenclature system for X-ray spectroscopy (recommendations 1991).* Pure and Applied Chemistry, **63**, 734 (1991).

[73] Debertin, K. and Helmer, R. *Gamma- and X-ray spectrometry with semiconductor detectors.* North-Holland (1988).

[74] Kinnunen, K. M., Palosaari, M. R. J., and Maasilta, I. J. *Normal metal-superconductor decoupling as a source of thermal fluctuation noise in transition-edge sensors.* Journal of Applied Physics, **112** (2012).

[75] Hilton, G., Martinis, J. M., Irwin, K., Bergren, N., Wollman, D., Huber, M., Deiker, S., and Nam, S. *Microfabricated transition-edge X-ray detectors.* Applied Superconductivity, IEEE Transactions on, **11**, 739 (2001).

[76] Franssila, S. *Introduction to Microfabrication.* Wiley (2004).

[77] Madou, M. *Fundamentals of Microfabrication: The Science of Miniaturization, Second Edition.* Taylor & Francis (2002).

[78] Menz, W., Mohr, J., and Paul, O. *Microsystem Technology.* Wiley (2008).

[79] Kittel, C. *Introduction to Solid State Physics.* 7th edition. John Wiley (1996).

[80] de Gennes, P. G. *Superconductivity of Metals and Alloys.* Addison-Wesley (1994).

[81] Gullikson, E. *Filter transmission* (2015). `http://henke.lbl.gov/optical_constants/`.

[82] Ullom, J. N., Beall, J. A., Doriese, W. B., Duncan, W. D., Ferreira, L., Hilton, G. C., Irwin, K. D., Reintsema, C. D., and Vale, L. R. *Optimized transition-edge X-ray microcalorimeter with 2.4 eV energy resolution at 5.9 keV.* Applied Physics Letters, **87**, 194103 (2005).

[83] Martinis, J. M., Hilton, G., Irwin, K., and Wollman, D. *Calculation of T_C in a normal-superconductor bilayer using the microscopic-based usadel theory.* Nuclear Instruments and Methods in Physics Research Section A: Accelerators, Spectrometers, Detectors and Associated Equipment, **444**, 23 (2000).

[84] Wang, S.-Q., Suthar, S., Hoeflich, C., and Burrow, B. J. *Diffusion barrier properties of TiW between Si and Cu.* Journal of Applied Physics, **73**, 2301 (1993).

[85] Luukanen, A., Kinnunen, K. M., Nuottajärvi, A. K., Hoevers, H. F. C., Bergmann Tiest, W. M., and Pekola, J. P. *Fluctuation-limited noise in a superconducting transition-edge sensor.* Phys. Rev. Lett., **90**, 238306 (2003).

[86] Kinnunen, K., Nuottajärvi, A., and Maasilta, I. *A transition-edge sensor with two excess noise mechanisms.* Journal of Low Temperature Physics, **151**, 144 (2008).

[87] Puurunen, R. L. *Surface chemistry of atomic layer deposition: A case study for the trimethylaluminum/water process.* Journal of Applied Physics, **97**, 121301 (2005).

[88] Brodie, I. and Muray, J. J. *The Physics of Micro/Nano-Fabrication.* Plenum Press (1995).

[89] Gloersen, P. G. *Ion-beam etching.* Journal of Vacuum Science and Technology, **12**, 28 (1975).

[90] Sadleir, J., Bandler, S., Brekosky, R., Chervenak, J., Figueroa-Feliciano, E., Finkbeiner, F., Iyomoto, N., Kelley, R., Kilbourne, C., King, J., Porter, F., Robinson, I., Saab, T., and Talley, D. *Bismuth X-ray absorber studies for TES microcalorimeters.* Nuclear Instruments and Methods in Physics Research Section A: Accelerators, Spectrometers, Detectors and Associated Equipment, **559**, 447 (2006).

[91] Pekola, J. and Kauppinen, J. *Insertable dilution refrigerator for characterization of mesoscopic samples.* Cryogenics, **34**, 843 (1994).

[92] Sadleir, J. E., Smith, S. J., Bandler, S. R., Chervenak, J. A., and Clem, J. R. *Longitudinal proximity effects in superconducting transition-edge sensors.* Phys. Rev. Lett., **104**, 047003 (2010).

[93] Bird, R. and Williams, J. *Ion Beams for Materials Analysis.* Elsevier Science (1990).

[94] Laitinen, M., Rossi, M., Julin, J., and Sajavaara, T. *Time-of-flight - energy spectrometer for elemental depth profiling - Jyväskylä design.* Nuclear Instruments and Methods in Physics Research Section B: Beam Interactions with Materials and Atoms, **337**, 55 (2014).

[95] Puttaraksa, N., Gorelick, S., Sajavaara, T., Laitinen, M., Singkarat, S., and Whitlow, H. J. *Programmable proximity aperture lithography with Mev ion beams.* Journal of Vacuum Science & Technology B, **26**, 1732 (2008).

[96] Reis, M. A., Chaves, P. C., and Taborda, A. *Radiative auger emission satellites observed by microcalorimeter-based energy-dispersive high-resolution PIXE.* X-Ray Spectrometry, **40**, 141 (2011).

[97] Gatti, E. and Rehak, P. *Semiconductor drift chamber an application of a novel charge transport scheme.* Nuclear Instruments and Methods in Physics Research, **225**, 608 (1984).

[98] Spieler, H. *Semiconductor Detector Systems.* Series on Semiconductor Science and Technology. OUP Oxford (2005).

[99] Lechner, P., Fiorini, C., Hartmann, R., Kemmer, J., Krause, N., Leutenegger, P., Longoni, A., Soltau, H., Sttter, D., Stter, R., Strder, L., and Weber, U. *Silicon drift detectors for high count rate X-ray spectroscopy at room temperature.* Nuclear Instruments and Methods in Physics Research Section A: Accelerators, Spectrometers, Detectors and Associated Equipment, **458**, 281 (2001).

[100] Lechner, P., Eckbauer, S., Hartmann, R., Krisch, S., Hauff, D., Richter, R., Soltau, H., Strder, L., Fiorini, C., Gatti, E., Longoni, A., and Sampietro, M. *Silicon drift detectors for high resolution room temperature X-ray spectroscopy.* Nuclear Instruments and Methods in Physics Research Section A: Accelerators, Spectrometers, Detectors and Associated Equipment, **377**, 346 (1996).

[101] Griffiths, D. *Introduction to Quantum Mechanics.* Pearson international edition. Pearson Prentice Hall (2005).

[102] Lapicki, G. *Cross sections for K-shell X-ray production by hydrogen and helium ions in elements from beryllium to uranium.* Journal of Physical and Chemical Reference Data, **18** (1989).

[103] Reintsema, C. D., Adams, J. S., Baker, R., Bandler, S. R., Doriese, W. R., Figueroa-Feliciano, E., Hilton, G. C., Irwin, K. D., Kelly, R. L., Kilbourne, C. A., Krinsky, J. W., Porter, F. S., and Wikus, P. *Electronics for a next-generation SQUID-based time-domain multiplexing system.* AIP Conference Proceedings, **1185**, 237 (2009).

[104] Tan, H., Breus, D., Hennig, W., Sabourov, K., Warburton, W. K., Doriese, W., Ullom, J. N., Bacrania, M. K., Hoover,

A. S., and Rabin, M. W. *High rate pulse processing algorithms for microcalorimeters* (2008).

[105] Doriese, W. B., Adams, J. S., Hilton, G. C., Irwin, K. D., Kilbourne, C. A., Schima, F. J., and Ullom, J. N. *Optimal filtering, record length, and count rate in transition-edge sensor microcalorimeters.* AIP Conference Proceedings, **1185**, 450 (2009).

[106] Winkler, R., Hoover, A., Rabin, M., Bennett, D., Doriese, W., Fowler, J., Hays-Wehle, J., Horansky, R., Reintsema, C., Schmidt, D., Vale, L., and Ullom, J. *256-pixel microcalorimeter array for high-resolution γ-ray spectroscopy of mixed-actinide materials.* Nuclear Instruments and Methods in Physics Research Section A: Accelerators, Spectrometers, Detectors and Associated Equipment, **770**, 203 (2015).

[107] Figueroa-Feliciano, E., Cabrera, B., Miller, A., Powell, S., Saab, T., and Walker, A. *Optimal filter analysis of energy-dependent pulse shapes and its application to TES detectors.* Nuclear Instruments and Methods in Physics Research Section A: Accelerators, Spectrometers, Detectors and Associated Equipment, **444**, 453 (2000).

[108] Moseley, S., Kelley, R., Schoelkopf, R., Szymkowiak, A., McCammon, D., and Zhang, J. *Advances toward high spectral resolution quantum X-ray calorimetry.* Nuclear Science, IEEE Transactions on, **35**, 59 (1988).

[109] Hussein, E. *Handbook on Radiation Probing, Gauging, Imaging and Analysis: Volume I: Basics and Techniques.* Basics and techniques. Springer (2003).

[110] Jun, K. *Chemical effects in the satellites of X-ray emission spectra.* Nuclear Instruments and Methods in Physics Research Section B: Beam Interactions with Materials and Atoms, **75**, 3 (1993).

[111] Paul, H. and Sacher, J. *Fitted empirical reference cross sections for K-shell ionization by protons.* Atomic Data and Nuclear Data Tables, **42**, 105 (1989).

[112] Orlic, I., Sow, C., and Tang, S. *Experimental L-shell X-ray production and ionization cross sections for proton impact.* Atomic Data and Nuclear Data Tables, **56**, 159 (1994).

[113] Pearce, N., Perkins, W., Westgate, J., Gorton, M., Jackson, S., Neal, C., and Cheney, S. *A compilation of new and published major and trace element data for NIST SRM 610 and NIST SRM 612 glass reference materials.* Geostandards Newsletter, **21**, 115 (1997).

[114] Hubbell, J. H. and Seltzer, S. M. *Tables of X-ray mass attenuation coefficients and mass energy- absorption coefficients (version 1.4)* (2015). http://physics.nist.gov/xaamdi.

[115] Demortier, G. *Review of the recent applications of high energy microprobes in arts and archaeology.* Nuclear Instruments and Methods in Physics Research Section B: Beam Interactions with Materials and Atoms, **54**, 334 (1991).

[116] Kallithrakas-Kontos, N. *X-ray chemical shift determination by energy dispersive detection.* Spectrochimica Acta Part B, **51**, 1655 (1996).

[117] Bayda, E. and z, E. *Chemical effects in the Kα and Kβ$_{1,3}$ of X-ray emission spectra of Fe.* Journal of Electron Spectroscopy and Related Phenomena, **185**, 27 (2012).

[118] Contarini, S., van der Heide, P., Prakash, A., and Kevan, L. *Titanium coordination in microporous and mesoporous oxide materials by monochromated X-ray photoelectron spectroscopy and X-ray auger electron spectroscopy.* Journal of Electron Spectroscopy and Related Phenomena, **125**, 25 (2002).

[119] Fukushima, S., Kimura, T., Nishida, K., Mihai, V. A., Yoshikawa, H., Kimura, M., Fujii, T., Oohashi, H., Ito, Y., and Yamashita, M. *The valence state analysis of Ti in $FeTiO_3$ by soft X-ray spectroscopy.* Microchimica Acta, **155**, 141 (2006).

[120] Mauron, O., Dousse, J.-C., Hoszowska, J., Marques, J. P., Parente, F., and Polasik, M. *L-shell shake processes resulting from 1s photoionization in elements 11<Z<17.* Phys. Rev. A, **62**, 062508 (2000).

Appendix A

Included publications

Article I

I

J Low Temp Phys (2012) 167:129–134
DOI 10.1007/s10909-012-0471-4

Analysis of Impedance and Noise Data of an X-Ray Transition-Edge Sensor Using Complex Thermal Models

M.R.J. Palosaari · K.M. Kinnunen · M.L. Ridder · J. van der Kuur · H.F.C. Hoevers · I.J. Maasilta

Received: 15 July 2011 / Accepted: 2 January 2012 / Published online: 11 January 2012

Abstract The so-called excess noise limits the energy resolution of transition-edge sensor (TES) detectors, and its physical origin has been unclear, with many competing models proposed. Here we present the noise and impedance data analysis of a rectangular X-ray Ti/Au TES fabricated at SRON. To account for all the major features in the impedance and noise data simultaneously, we have used a thermal model consisting of three blocks of heat capacities, whereas a two-block model is clearly insufficient. The implication is that, for these detectors, the excess noise is simply thermal fluctuation noise of the internal parts of the device. Equations for the impedance and noise for a three-block model are also given.

Keywords TES · Thermal model · Impedance · Noise

1 Introduction

Calorimeters and bolometers based on superconducting transition-edge sensors (TES) have proven to be valuable tools in a number of applications in a broad energy range [1]. The number of pixels in TES detector arrays are constantly increasing and the limits of single pixel performance are being pushed closer to the theoretical limits. However, the lack of understanding of some of the noise components ("excess noise") has plagued the field in recent years [2, 3]. One source for the excess noise, in addition to the recently introduced non-equilibrium Johnson noise [4], could be

M.R.J. Palosaari (✉) · K.M. Kinnunen · I.J. Maasilta
Nanoscience Center, Department of Physics, University of Jyväskylä, P.O. Box 35, 40014 Jyväskylä, Finland
e-mail: mikko.palosaari@jyu.fi

M.L. Ridder · J. van der Kuur · H.F.C. Hoevers
SRON Netherlands Institute for Space Research, Sorbonnelaan 2, 3584 Utrecht, The Netherlands

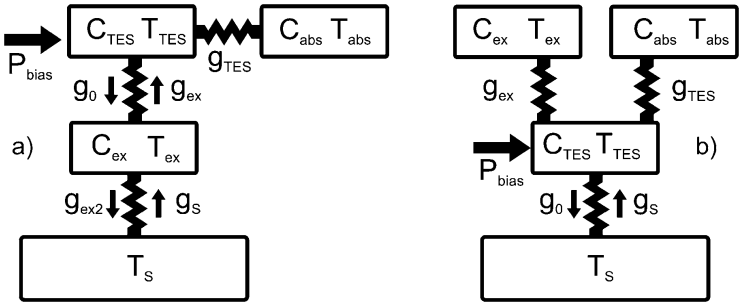

Fig. 1 (**a**) A model with one hanging and an intermediate block between the TES and the bath (IH model). (**b**) A model with two hanging thermal blocks (2H model)

a complex thermal circuit of the device: if the device consists of several blocks of heat capacity, more thermal fluctuation noise will exist [5, 6]. To determine unambiguously the thermal noise components of the device, the thermal circuit should be determined independently. This can be done by measuring the complex impedance in addition to the noise [7]. For the device discussed here, the impedance data is fit well by a three-block thermal model, and the model simultaneously explains all the noise of the device. Thus, all noise sources are fully understood in the detector types presented here.

2 Theoretical Models

To fully characterize the thermal and electrical properties of many TES devices, the conventional thermal model of one heat capacity connected to a heat bath is too simple. Even the model with one additional thermal block does not always fully fit the measured noise and impedance [8, 9]. Here we have used a system of three thermal blocks. We have analyzed the measured data with two different variations: one with both a hanging and an extra intermediate block between the TES and the heat bath, and another with two hanging thermal blocks (Fig. 1). The derivation and full theoretical discussion of the impedance and noise of the three-block models will be presented elsewhere [10], here we only cite the results for the IH model (Fig. 1a). Equations for 2H model (Fig. 1b) are similar. The IH model assumes that heat flows first from the TES to the "intermediate" or excess heat capacity C_{ex}, and only then to the heat bath, therefore the steady state temperatures of the TES and the excess heat capacity are not equal. The hanging heat capacity C_{abs} could represent the absorber, but does not in general need to do so, and in steady state it has the same temperature as the TES. There are now five different dynamical thermal conductances that need to be defined, one between the TES and the "absorber", two between the TES and the excess heat capacity and two between the excess heat capacity and the bath: $g_{TES} = nAT_{TES}^{n-1}$, $g_0 = mBT_{TES}^{m-1}$, $g_{ex} = mBT_{ex}^{m-1}$, $g_{ex2} = pCT_{ex}^{p-1}$, $g_s = pCT_s^{p-1}$, where the power between the TES and the absorber, the TES and the excess heat capacity, and the excess heat capacity and the bath are given by $P = A(T_{TES}^n - T_{abs}^n)$, $P = B(T_{TES}^m - T_{ex}^m)$ and $P = C(T_{ex}^p - T_s^p)$, respectively (see Fig. 1).

2.1 Complex Impedance

The complex impedance of the model (Fig. 1a) is

$$Z_{TES} = R_0(1+\beta) + \frac{\mathcal{L}}{1-\mathcal{L}} \frac{R_0(2+\beta)}{1+i\omega\tau_I - A(\omega) - B(\omega)}, \tag{1}$$

where $A(\omega) = \frac{1}{1-\mathcal{L}} \frac{g_{tes}}{(g_{tes}+g_0)} \frac{1}{1+i\omega\tau_{abs}}$, $B(\omega) = \frac{1}{1-\mathcal{L}} \frac{g_0 g_{ex}}{(g_{tes}+g_0)(g_{ex}+g_{ex2})} \frac{1}{1+i\omega\tau_{ex}}$, $\mathcal{L} = P_0\alpha/[(g_{tes}+g_0)T_0]$, $\tau_I = C_{tes}/[(g_{tes}+g_0)(1-\mathcal{L})]$, $\tau_{abs} = C_{abs}/g_{tes}$ and $\tau_{ex} = C_{ex}/(g_{ex}+g_{ex2})$, and the transition steepness parameters are $\alpha = \partial\log(R)/\partial\log(T)$, $\beta = \partial\log(R)/\partial\log(I)$ at the bias point R_0 (with power P_0 and temperature T_0).

2.2 Noise

Three major classes of unavoidable noise sources are included: the power fluctuations in the thermal circuit, the electrical thermal noise of the detector (Johnson noise), and the Johnson noise of the shunt resistor. We disregard correlations between fluctuations in the thermal conductances.

The frequency dependent current responsivity, $s_I(\omega) = I_\omega/P_\omega$, for power input in the TES heat capacity C_{tes} can be written [10] as

$$s_I(\omega) = -\frac{1}{Z_{circ} I_0} \frac{Z_{TES} - R_0(1+\beta)}{R_0(2+\beta)}, \tag{2}$$

where $Z_{circ} = Z_{TES} + R_L + i\omega L$, R_L is the Thevenin equivalent circuit resistance (shunt + parasitic) and L is the circuit inductance.

Now the thermal fluctuation current noise terms (one phonon noise term and two internal thermal fluctuation noise (ITFN) terms) are

$$|I|^2_{ph} = P^2_{ph}|s_I(\omega)|^2 \frac{g^2_{ex}}{(g_{ex}+g_{ex2})^2} \frac{1}{1+\omega^2\tau^2_{ex}}, \tag{3}$$

$$|I|^2_{ITFN,1} = P^2_{tes}|s_I(\omega)|^2 \frac{\omega^2\tau^2_{abs}}{1+\omega^2\tau^2_{abs}}, \tag{4}$$

$$|I|^2_{ITFN,2} = P^2_{ex}|s_I(\omega)|^2 \frac{g^2_{ex2}/(g_{ex2}+g_{ex})^2 + \omega^2\tau^2_{ex}}{1+\omega^2\tau^2_{ex}}, \tag{5}$$

where $P^2_{ph} = 2k_B(T^2_{ex}g_{ex2} + T^2_s g_s)$, $P^2_{tes} = 4k_B T^2_0 g_{tes}$ and $P^2_{ex} = 2k_B(T^2_0 g_0 + T^2_{ex} g_{ex})$.

The non-equilibrium Johnson current noise in the TES film is given by

$$|I|^2_J = \frac{V^2_\omega}{|Z_{circ,\infty} + \frac{\mathcal{L}(R_0 - R_L - i\omega L)}{1+i\omega\tau_{tes} - (1-\mathcal{L})(A(\omega)+B(\omega))}|^2}, \tag{6}$$

where [4] $V^2_\omega = 4k_B T_0 R_0(1+2\beta)$ and $Z_{circ,\infty} = R_0(1+\beta) + R_L + i\omega L$. The Johnson noise due to the shunt and parasitic resistances is simply $|I|^2_{sh} = V^2_{\omega,sh}/|Z_{circ}|^2$, with $V^2_{\omega,sh} = 4k_B T_{sh} R_L$ if both the parasitic resistance and the actual shunt are at temperature T_{sh}.

Fig. 2 (Color online) *Left*: schematic cross-sectional view of the device. *Orange*: Cu absorber and dots, *blue*: SiOx insulator, *gray*: Ti layers, *yellow*: Au layer, *black*: Nb contacts. *Right*: optical micrograph of the TES. The size of the Ti/Au TES is 186×150 μm^2 and it is on a 1 μm thick SiN membrane fabricated on Si (110) surface

3 Experiments and Analysis

The measured TES was a pixel from an X-ray array fabricated at SRON (Fig. 2). It features a $206 \times 162 \times 1$ μm^3 Cu absorber on top of a SiOx insulator that is coupled to the TES through seven rectangular vias at the center of the TES. There are also 10×7 Cu dots of 10 μm diameter on top of the TES film (but not in contact with the absorber) to tune the transition properties. The critical temperature, T_C, is 125.5 mK and normal state resistance $R_N \sim 300$ mΩ. Measurements were performed in a compact plastic dilution refrigerator at Jyväskylä, with an old NIST SQUID readout [11] and a FLL electronics unit designed at SRON. The complex impedance was measured up to 100 kHz, taking into account of the transfer function of the readout circuit [12].

In the analysis, the measured complex impedance and noise were fitted simultaneously by eye with the equations described above, as high-dimensional non-linear least-squares fitting would be demanding to implement. The heat capacities, g_0, g_{TES} and T_{ex} were free parameters. The other thermal conductances were calculated using the constraint that the total thermal conductance to the bath is fixed by the I–V data and that the links on both sides of the intermediate block have the same thermal exponent $p = m$. This is physically reasonable if all the conductances are dominated by the SiN membrane. During the fitting four curves were plotted on top of the experimental data: The noise as a function of frequency, the complex impedance and also the real and imaginary parts of the impedance as a function of frequency. White noise of 4 pA/$\sqrt{\text{Hz}}$ for the SQUID was included in the noise analysis.

4 Results and Discussion

One can fit all the major noise and impedance features with both three-block models (IH and 2H, Fig. 1), whereas a simpler two-block model (TES + hanging C) cannot produce an adequate fit, as can be seen in Fig. 3. In Fig. 4 the measured data and fitted theoretical curves for the IH model are presented. In the noise data, one can see that there is some deviation with the measured and the fitted data above 100 kHz. This is likely because the transfer function of the circuit was not corrected for in the noise data. We also analyzed the measured data with the two hanging (2H) block

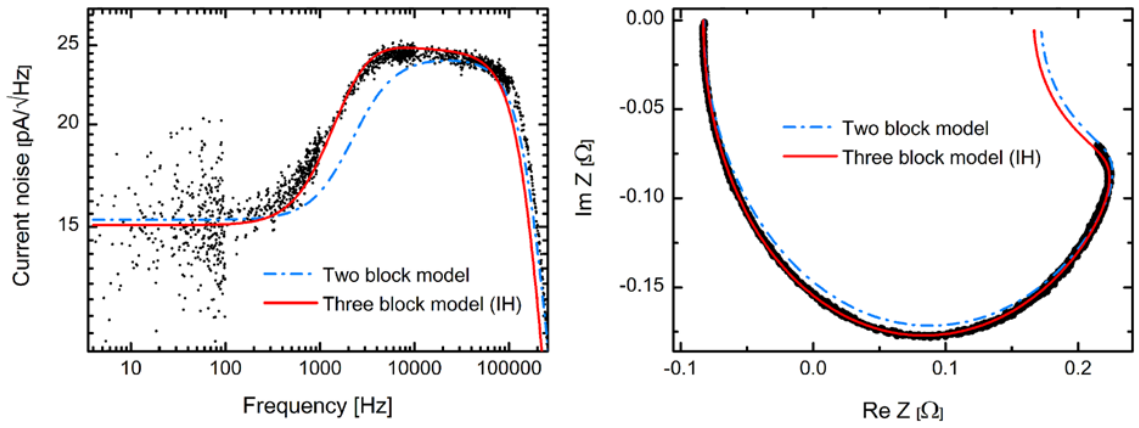

Fig. 3 (Color online) Comparison between a two-block model and the IH three-block model at 20% R/R_N

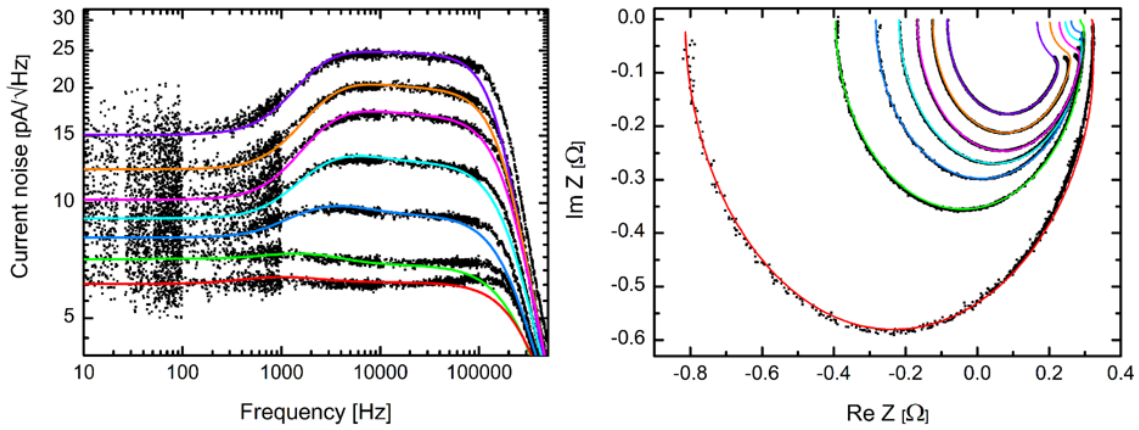

Fig. 4 (Color online) *Left*: the measured and fitted current noise of the device. *Right*: the measured and fitted complex impedance of the TES. Bias points between 20–80% R_N in 10% intervals are presented. The higher bias points correspond to the lower noise levels and bigger semicircles. Only IH model fits are shown, 2H fits look identical

model of Fig. 1b and obtained qualitatively identical goodness of fit results with the IH model. The fitted parameter values for both models are plotted in Fig. 5, except for C_{ex} in the 2H model which was approximately constant $C_{ex} \approx 0.08$ pJ/K. We also estimated the theoretical heat capacity of the Cu absorber, $C_{abs} = \gamma T_{TES}$, to be around 0.40 pJ/K, which is quite close to the fitted C_{abs}, as shown in Fig. 5a. The TES film heat capacity C_{TES} was also calculated with a correction [13] to the BCS heat capacity jump for bilayer films, to get values around 0.08 pJ/K, which again agrees with our results. We see that the two model variants do not produce significant differences, and cannot be easily differentiated from each other. We do not want to draw conclusions from the bias dependence of the parameters yet, because we have evidence that the IH model is required even in devices without an absorber [6].

In conclusion, good simultaneous fit to complex impedance and noise can only be achieved with a three-block model in these devices. The fitting parameter values are consistent with the heat capacities being the TES film, the absorber and a third

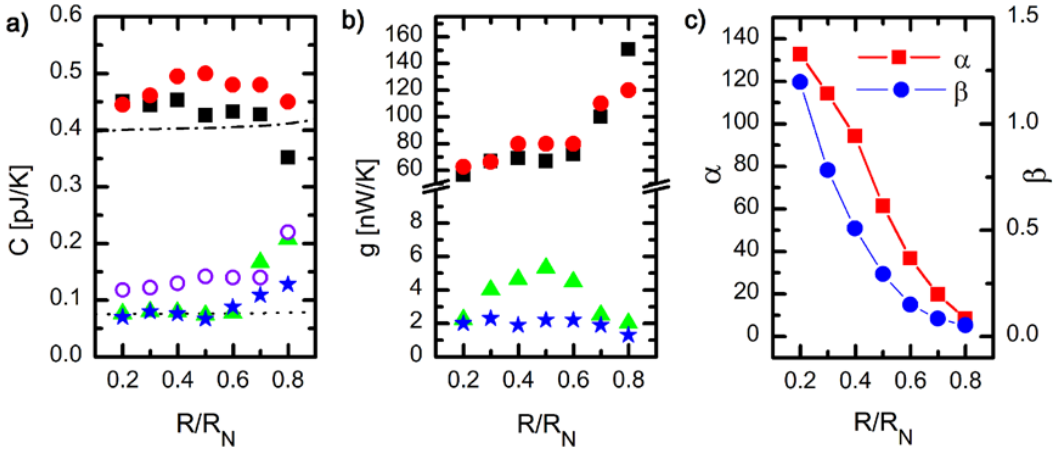

Fig. 5 (Color online) Some of the parameters from both IH and 2H models vs. bias point. (**a**) C_{TES} (IH: *triangles*, 2H: *stars*), C_{abs} (IH: *squares*, 2H: *circles*) and C_{ex} (IH: *open circles*) and the estimated theoretical values as dashed lines. (**b**) g_{TES} (IH: *squares*, 2H: *circles*), g_0 (IH: *triangles*) and g_{Ex} (2H: *stars*). (**c**) α and β

unknown heat capacity of the order of 0.1 pJ/K. No unexplained excess noise remains after the three-block fit.

Acknowledgements This work was supported by ESA contract no. AO/1-4005/01/NL/HB, the Finnish Funding Agency for Technology and Innovation TEKES and EU through the regional funds, and the Finnish Academy project no. 128532. M. P. would like to thank the National Graduate School in Materials Physics for funding.

References

1. K. Irwin, G. Hilton, in *Cryogenic Particle Detection*, ed. by Ch. Enss (Springer, Berlin, 2005), p. 63
2. J.N. Ullom et al., Appl. Phys. Lett. **84**, 4206 (2004)
3. K.M. Kinnunen, A.K. Nuottajärvi, J. Leppäniemi, I.J. Maasilta, J. Low Temp. Phys. **151**, 119 (2008)
4. K.D. Irwin, Nucl. Instrum. Methods Phys. Res., Sect. A, Accel. Spectrom. Detect. Assoc. Equip. **559**, 718 (2006)
5. H.F.C. Hoevers, A.C. Bento, M.P. Bruijn, L. Gottardi, M.A.N. Korevaar, W.A. Mels, P.A.J. de Korte, Appl. Phys. Lett. **77**, 4422 (2000)
6. K.M. Kinnunen, M.R.J. Palosaari, I.J. Maasilta (submitted for publication). arXiv:1111.4098v1
7. M. Lindeman et al., Rev. Sci. Instrum. **75**, 1283 (2004)
8. I.J. Maasilta, K.M. Kinnunen, AIP Conf. Proc. **1185**, 38 (2009)
9. Y. Zhao et al., IEEE Trans. Appl. Supercond. **21**, 227 (2011)
10. I.J. Maasilta, to be published
11. J.A. Chervenak et al., Appl. Phys. Lett. **74**, 4043 (1999)
12. Y. Takei et al., J. Low Temp. Phys. **151**, 161 (2008)
13. A. Kozorezov et al., AIP Conf. Proc. **1185**, 27 (2009)

Article II

II

J Low Temp Phys (2014) 176:285–290
DOI 10.1007/s10909-013-1004-5

Transition-Edge Sensors for Particle Induced X-ray Emission Measurements

M. R. J. Palosaari · K. M. Kinnunen · J. Julin · M. Laitinen · M. Napari · T. Sajavaara · W. B. Doriese · J. Fowler · C. Reintsema · D. Swetz · D. Schmidt · J. Ullom · I. J. Maasilta

Received: 12 July 2013 / Accepted: 2 December 2013 / Published online: 15 December 2013

Abstract In this paper we present a new measurement setup, where a transition-edge sensor detector array is used to detect X-rays in particle induced X-ray emission (PIXE) measurements with a 2 MeV proton beam. Transition-edge sensors offer orders of magnitude improvement in energy resolution compared to conventional silicon or germanium detectors, making it possible to recognize spectral lines in materials analysis that have previously been impossible to resolve, and to get chemical information from the elements. Our sensors are cooled to the operation temperature (∼65 mK) with a cryogen-free adiabatic demagnetization refrigerator, which houses a specially designed X-ray snout that has a vacuum tight window to couple in the radiation. For the best pixel, the measured instrumental energy resolution was 3.06 eV full width at half maximum at 5.9 keV. We discuss the current status of the project, benefits of transition-edge sensors when used in PIXE spectroscopy, and the results from the first measurements.

Keywords Transition-edge sensor · TES · Particle induced X-ray emission (PIXE)

M. R. J. Palosaari ( ) · K. M. Kinnunen · I. J. Maasilta
Department of Physics, Nanoscience Center, University of Jyväskylä,
P.O. Box 35, 40014 Jyväskylä, Finland
e-mail: mikko.palosaari@jyu.fi

J. Julin · M. Laitinen · M. Napari · T. Sajavaara
Accelerator Laboratory, Department of Physics, University of Jyväskylä,
P.O. Box 35, 40014 Jyväskylä, Finland

W. B. Doriese · J. Fowler · C. Reintsema · D. Swetz · D. Schmidt · J. Ullom
National Institute of Standards and Technology,
Boulder, CO 80305, USA

1 Introduction

In particle induced X-ray emission (PIXE) measurements an energetic ion beam, normally a 1–4 MeV hydrogen or helium ion-beam, is directed to the sample to be analyzed, and sample composition for elements typically heavier than Na or Mg can be determined by means of characteristic X-ray emission [1]. Over the last four decades PIXE has developed to become a standard tool for elemental analysis in many fields of science. In geology, art restoration and medical diagnostic, to name a few, PIXE has been used to determine the elemental composition of samples [2–4].

The development of micro-PIXE, where the particle beam is focused to about 1 μm diameter spot, has opened the possibility to raster the target in order to get the positional elemental information of the sample. One interesting special feature of PIXE is that it is possible to irradiate samples with ion beams in ambient conditions, thus making the analysis of biological and large specimens, like paintings, possible. In addition, compared to electron beam excitement, the bremsstrahlung from protons is negligible because of their higher mass [1]. This means that the continuum X-ray background is orders of magnitude smaller compared to scanning electron microscope energy-dispersive X-ray spectroscopy (SEM-EDX).

Traditionally, reverse biased silicon or germanium detectors have been the work horse for PIXE because of their wide dynamic range in energy, ease of use and reasonable cost. These properties have so far compensated the limited energy resolution. On the other hand, wavelength dispersive detectors with their great energy resolution have been successfully used with PIXE [5], but their intrinsically low throughput makes the measurements cumbersome and time consuming.

By using transition-edge sensor (TES) microcalorimeters operating at cryogenic temperatures, one combines the benefits of energy dispersive detectors (efficiency, wide energy range) and wavelength dispersive detectors (resolution) [6]. TES detectors have matured to the state where they are used in number of applications, thanks to their superior energy resolution and sensitivity. A TES is a device that operates between the superconducting and the normal state of a metallic thin film with a coupled absorber [7].

Within the superconducting transition region, the resistance of a TES is very sensitive to changes in temperature. The device is connected to a heat bath via a weak thermal link so that when a photon hits the absorber and is converted into heat, due to the small heat capacity of the detector, a relatively large temperature excursion and change in the resistance of the detector is produced. The change in the current through the TES during the photon event is read out with a superconducting quantum interference device (SQUID), which acts as a highly sensitive current sensor that can be coupled to the low impedance of the TES [7]. Multiplexing is needed, when the number of detectors increases and when the number of measurement wires needs to be minimized in order to limit the thermal load to the cryostat.

Demonstrations of combining a single TES detector pixel with PIXE have been published before [8], but the energy resolution achieved (∼18 eV at 1.7 keV) has been much worse than in this work, and quite far from the expected theoretical limits of ∼1.3 eV for a typical TES detector at that energy [9].

2 Experimental Setup

A Pelletron accelerator with 1.7 MV maximum terminal voltage was used to produce 2.015 MeV incident $^{1}H^{+}$ ion beam that was used in the measurements. The TES X-ray detector array was positioned to an angle of 90° with respect to the incident ion beam. The sample was tilted 45 ° towards the detector (see Fig. 1). The backscattered incident ions were stopped before reaching the detector snout by means of 80 μm Polyethylene terephthalate (PET) film inside the sample chamber, which also filtered out low-energy X-rays. An Amptek X-123SDD silicon drift detector (SDD) (130 eV resolution for 5.9 keV X-rays from ^{55}Fe source) positioned to an angle of 135° with respect to beam line was used as a reference detector.

The microcalorimeter TES detector array consisting of 160 pixels was fabricated at NIST Boulder. The superconducting thin film is a molybdenum–copper bilayer film, where the proximity effect [10] is used to achieve a critical temperature of ∼100 mK. The absorber is made of bismuth with horizontal dimensions of 350 μm × 350 μm and with 2.5 μm thickness. A collimator with a 320 μm × 305 μm aperture size for each pixel is placed on top of the detector chip to stop photons from hitting the substrate. The separation between the detector and the collimator is 20 μm. The X-rays from the sample chamber enter through a vacuum window (AP3.3 ultra-thin polymer/Al silicon grid X-ray window by Moxtek Inc.) into the cryostat. Inside the detector snout, the X-rays still have to penetrate through three layers of IR radiation filters (each a 1 μm PET film with 1 μm aluminum coating) at three different temperature stages of the snout (60, 1 K, 50 mK), before impinging on the TES detector array.

In these first measurements only 12 pixels were connected out of which 9 gave good data. One pixel had major problems with SQUID locking and did not produce good enough data and two pixels had over an order of magnitude smaller count rates and their data was removed from the final spectra due to energy calibration problems of insufficient number of events. The read-out of the detectors was realized with NIST time-division-multiplexing (TDM) SQUID electronics [11]. In TDM, many microcalorimeters are read out in a single set of wires by turning the SQUIDs on sequentially.

The cryogenic cooling was achieved with an adiabatic demagnetization refrigerator (ADR) (Denali Model 102, High Precision Devices, Inc.). The cryostat has a special snout designed to couple the X-rays into the detectors, with two layers of cylindrical magnetic shielding from A4K material (Amuneal Corp.) at 60 and 1 K, and one

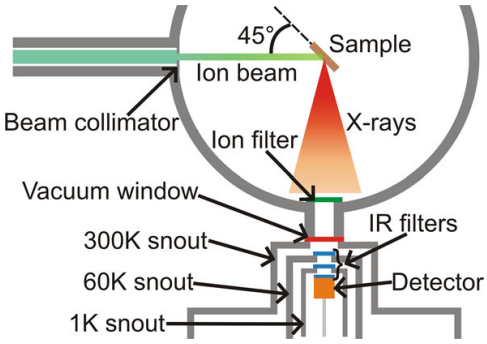

Fig. 1 Schematic image of the target chamber and the ADR snout separated by a vacuum window. The distance from the sample to the detector was 30 cm. The dimensions are not in scale. The SDD measurements were done in a different target chamber. (Color figure online)

cylindrical superconducting Al shield at 50 mK. The pre-cooling of the ADR's two stages (60 and 3 K) is done with Cryomech pulse-tube refrigerator model no. PT407 RM, making the whole system cryogen-free. Vibrations from the pulse tube are minimized by using a remote valve system and a flexible bellows between the pulse tube and cryostat body. The control software and hardware for the ADR's 4 T magnet was made by STAR Cryoelectronics LLC. The ADR has a base temperature of ∼30 mK and can be regulated at the 65 mK operation point with below 15 μK rms accuracy for about 12 hours with the read-out electronics on.

In this first proof of principle measurement, the detector array was in a location with a solid angle of only $\Omega = 1.3 \times 10^{-5}$ of 4π sr (for the 12 pixels and only the absorber area visible through the collimator) at a distance of 30 cm from the sample. The solid angle will be increased by a factor of 36 in the future by moving the detector array closer to the sample from 30 to 5 cm. Also, by connecting all of the 160 pixels the solid angle will increase by another factor of 13, leading to a total increase by a factor 468. This increase will translate straight to increase in the X-ray count rates and it gives the possibility to study thin film samples in contrast to the bulk samples discussed here.

3 Results

A spectrum of Mn Kα lines produced by a ^{55}Fe-source was measured. After the subtraction of the natural line shape and width of the emission, the instrumental energy resolution of the best pixel was 3.06 eV full width at half maximum (FWHM), which is within a few percent of the expected resolution based on the measured average signal and noise. The arithmetic mean resolution of 9 pixels was (3.8 ± 0.6) eV each having approximately the same number of events. No external magnetic field optimization was done during the measurements for any of the results.

In Fig. 2, we present the comparison between the ^{55}Fe produced Mn spectrum and spectrum from a PIXE measurement with 2 MeV protons and a Mn sample, with the

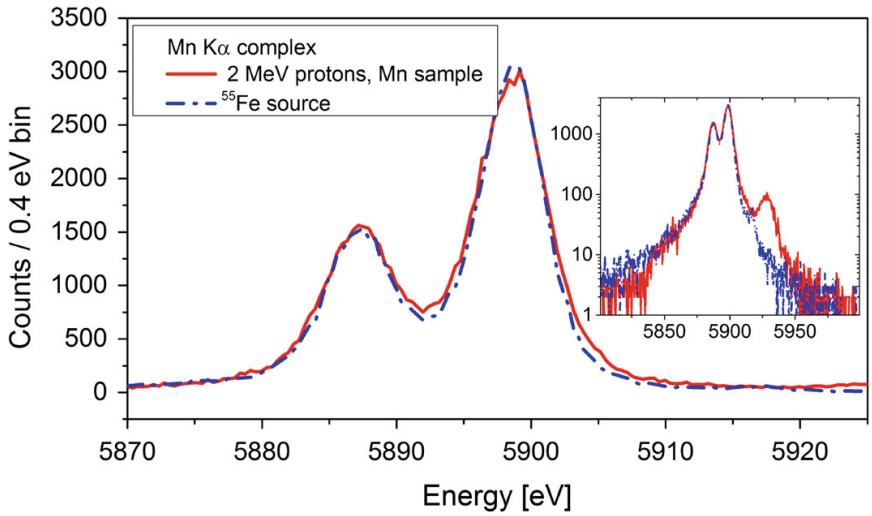

Fig. 2 Comparison of Mn Kα complex spectrum of PIXE and ^{55}Fe source. Spectra are combined from the 9 pixels. *Inset* shows a satellite peak in the PIXE spectrum discussed later. (Color figure online)

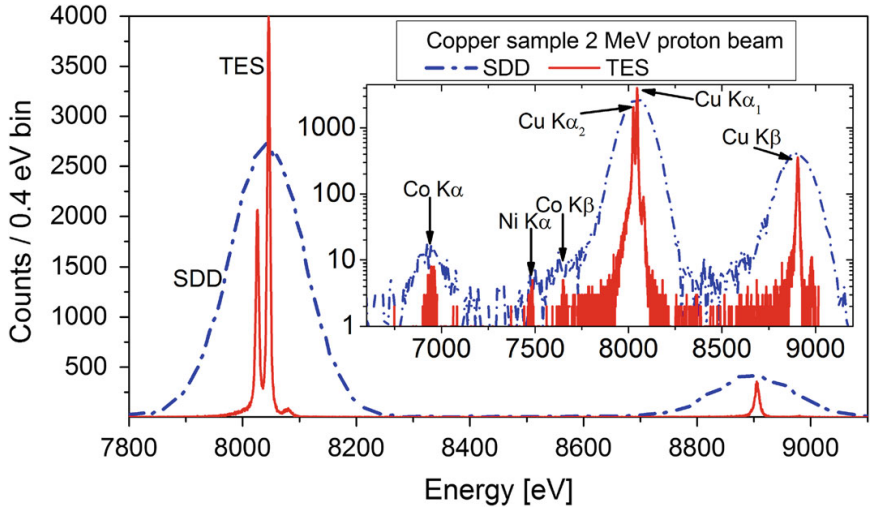

Fig. 3 Comparison of Cu-sample spectra excited with 2 MeV protons measured with TES (9 pixels) and SDD detectors. Inset shows the same data in logarithmic scale, where the Co Kα, Kβ and Ni Kα impurity lines of the sample are more visible. The theoretical energy values [13] for the impurity lines are represented with the vertical arrows. (Color figure online)

combined data from the 9 pixels. The FWHM broadens by less than 1 eV with the PIXE data compared to the ^{55}Fe measurement (4.45 vs. 3.75 eV respectively). The origin of this broadening is not yet fully understood, but there was some electrical interference present during the Mn PIXE measurement unlike in the ^{55}Fe measurement, which could affect the energy resolution.

A bulk copper sample was also measured with 2 MeV proton excitation, using both TES and SDD detectors to compare the two detector types, with the results shown in Fig. 3. The Ni impurities in the sample cannot easily be resolved with the SDD detector but they are clear in the TES data. The satellite peak on the high energy side of the Cu Kα_1 and Cu kβ emission line visible in the TES spectrum is possibly a multivacancy satellite line, where two (or more) inner shell electron vacancies are created simultaneously [12]. The same feature is also seen in the Mn spectrum in Fig. 2.

4 Conclusions

In this paper, we have demonstrated particle induced X-ray emission (PIXE) spectroscopy using a multiplexed microcalorimeter TES detector array with an unprecedented energy resolution for PIXE applications. In the future, the beam line and the target chamber will be optimized to maximize the X-ray flux for thin film analysis. This will make it possible to measure not only the elemental composition of thin films in greater detail, but also the chemical environment of the different elements in cases where the chemical shifts are large. Another very interesting future application is the study of the formation of embedded metallic clusters in insulators after implantation and annealing.

Acknowledgments This work was supported by the Finnish Funding Agency for Technology and Innovation TEKES, Academy of Finland Project no. 260880 and Academy of Finland Center of Excellence

in Nuclear and Accelerator Based Physics (ref. 251353). M. Palosaari would personally like to thank the National Graduate School in Materials Science for funding.

References

1. S.A.E. Johansson, in *Particle-Induced X-ray Emission Spectrometry (PIXE), Volume 133 in Chemical Analysis: A Series of Monographs on Analytical Chemistry and Its Applications*, ed. by S.A.E. Johansson, J.L. Campbell, K.G. Malmqvist, (Wiley, New York, 1995)
2. S.M. Tang, S.H. Tang, T.S. Tay, A.T. Retty, Appl. Spectrosc. **42**, 44 (1988)
3. N. Grassi, P. Bonanni, C. Mazzotta, A. Migliori, P.A. Mandò, X-ray Spectrom. **38**, 301 (2009)
4. Ph Moretto, Y. Llabador, M. Simonoff, L. Razafindrabe, M. Bara, A. Guiet-Bara, Nucl. Instr. Method B **77**, 275 (1993)
5. J. Hasegawa, T. Tada, Y. Oguri, M. Hayashi, T. Toriyama, T. Kawabata, K. Masai, Rev. Sci. Instrum. **78**, 073105 (2007)
6. S.H. Moseley, J. Mather, D. McCammon, J. Appl. Phys. **56**, 1257 (1984)
7. K. Irwin, G. Hilton, in *Cryogenic Particle Detection*, ed. by Ch. Enss (Springer, Berlin, 2005), p. 63
8. M.A. Reis, P.C. Chaves, A. Taborda, X-ray Spectrom. **40**, 141 (2011)
9. J.N. Ullom, J.A. Beall, W.B. Doriese, W.D. Duncan, L. Ferreira, G.C. Hilton, K.D. Irwin, C.D. Reintsema, L.R. Vale, Appl. Phys. Lett. **87**, 194103 (2005)
10. P.G. de Gennes, *Superconductivity of Metals and Alloys* (Redwood City, Addison-Wesley, 1994)
11. P.A.J. de Korte, J. Beyer, S. Deiker, G.C. Hilton, K.D. Irwin, M. MacIntosh, S. Woo Nam, C.D. Reintsema, L.R. Vale, M.E. Huber, Rev. Sci. Instrum. **74**, 8 (2003)
12. K. Jun, Nucl. Instrum. Methods B **75**, 3 (1993)
13. J.A. Bearden, Rev. Mod. Phys. **39**, 78 (1967)

Article III

III

Large 256-Pixel X-ray Transition-Edge Sensor Arrays With Mo/TiW/Cu Trilayers

Mikko R. J. Palosaari, Leif Grönberg, Kimmo M. Kinnunen, David Gunnarsson, Mika Prunnila, and Ilari J. Maasilta

***Abstract*—We describe the fabrication and electrical characterization of 256-pixel X-ray transition-edge sensor (TES) arrays intended for materials analysis applications. The processing is done on 6-in wafers, providing capabilities on a commercial scale. TES films were novel proximity coupled Mo/TiW/Cu trilayers, where the thin TiW layer in between aims to improve the stability of the devices by preventing unwanted effects such as Mo/Cu interdiffusion. The absorber elements were electrodeposited gold of thickness 2 μm. The single-pixel design discussed here is the so-called Corbino geometry. Most design goals were successfully met, such as the critical temperature, thermal time constant, and transition steepness.**

***Index Terms*—Large format arrays, transition-edge sensors, X-ray spectroscopy.**

I. Introduction

LARGE format arrays of sensitive radiation detectors are important in nearly all applications where the detectors find use. That is also the case with transition-edge sensors (TES) [1], which have been applied in large array format from the detection of gamma-rays [2] to sub-mm radiation [3]. For the X-ray energy band, TES detector arrays have mostly been developed for their eventual use in future astrophysics satellite missions, and large 240–1024 pixel arrays have successfully been fabricated for example in Refs. [4]–[6].

Here, we report the first results on our new large-format X-ray Mo/TiW/Cu TES arrays containing 256 pixels, fabricated on 6-in wafers at VTT's (Technical Research Centre of Finland) Micronova clean room facilities. The single-pixel design is based on the circular Corbino geometry, which was previously fabricated from Ti/Au bilayers as single pixels at Jyväskylä, using electron-beam lithography [7], [8]. Mo/TiW/Cu was chosen here over Ti/Au to lower the film resistivity, which is needed for proper impedance matching to the readout. The design and its implementation will be explained in detail, in addition to some examples of electrical characterization on some pixels.

Manuscript received August 10, 2014; accepted October 16, 2014. Date of publication November 4, 2014; date of current version December 15, 2014. This work was supported in part by the Finnish Funding Agency for Innovation (TEKES) and in part by the Academy of Finland under Project 260880.

M. R. J. Palosaari, K. M. Kinnunen, and I. J. Maasilta are with the Nanoscience Center, Department of Physics, University of Jyväskylä, 40014 Jyväskylä, Finland (e-mail: mikko.palosaari@jyu.fi; kimmo.m.kinnunen@jyu.fi; maasilta@jyu.fi).

L. Grönberg, D. Gunnarsson, and M. Prunnila are with the VTT Technical Research Centre of Finland, 02044 Espoo, Finland (e-mail: leif.gronberg@vtt.fi; david.gunnarsson@vtt.fi; mika.prunnila@vtt.fi).

Color versions of one or more of the figures in this paper are available online at http://ieeexplore.ieee.org.

Digital Object Identifier 10.1109/TASC.2014.2366641

Here, the arrays are primarily designed for terrestrial materials science applications, like, for example, for particle-induced X-ray emission spectroscopy (PIXE) of material composition, especially impurities [9], or for time-resolved table-top extended X-ray absorption fine structure spectroscopy (EXAFS) of chemical reactions [10]. Similar arrays could also be used for synchrotron-based spectroscopies [5] or e-beam-induced X-ray spectroscopy [11].

II. Design Guidelines

The major design guidelines we used are as follows:

i) In astrophysics applications, dense packing of the individual pixels is essential for efficient photon collection from dim sources [4]. As our design is to be used for materials science applications, where the X-ray flux is not necessarily small and can perhaps be adjusted by a control parameter (such as laser power in table-top EXAFS [10] or ion beam current in PIXE [9]), we do not need a complete coverage of the detector area. This has the big advantage that mushroom-type complex absorber designs [4] are not necessary.

ii) State-of-the-art SQUID multiplexing electronics [12] currently limits the number of pixels that can be read out to around a few hundred. For this reason, we have decided to limit ourselves to 256 pixels in the first generation arrays.

iii) The diameter of the active detector area (12.5 mm) was chosen to match the X-ray window size in the ADR setup at Jyväskylä [9].

iv) To facilitate a larger yield from a single fabrication round and to conform to Micronova instrumentation, 6-in wafer size was chosen. This means that 36 chips can be fabricated on each wafer.

v) We chose the circular Corbino geometry [7], [13] for the single-pixel design, where the current in the TES film flows radially, unlike in a square TES design, from a center contact to an annular outer edge contact. One benefit of the Corbino design is the lack of edge effects. This means that we do not have to use any normal metal edge banks, as is typically done with square designs, to suppress superconductivity at the edges to overcome critical temperature variation or etching problems [1], [14], which simplifies the fabrication. Also, the absorber contacts the TES film only at the center, which stays in the normal state anyways in the Corbino design, due to the higher current density there [13]. Thus, we do not have to worry about any added direct proximity effect from the absorber. Another reason for using Corbino geometry is

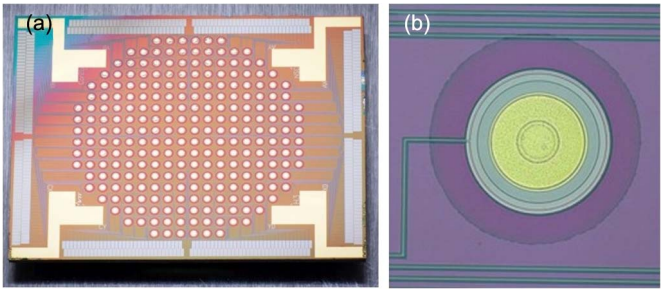

Fig. 1. (a) Two-hundred-fifty-six-pixel X-ray TES array chip. The size of the chip is 15 mm × 19 mm. Visible in the image: Nb bonding pads and leads, Au absorbers, and thermalization pads. (b) Micrograph of a single pixel. The center area is covered by a Au absorber that contacts the TES film in the inner circle area. The outer annular Nb contact is visible at the outside edge of the TES (diameter 360 μm), as is the released SiN membrane edge (diameter 500 μm) outside the pixel. The lines are Nb microstrip leads.

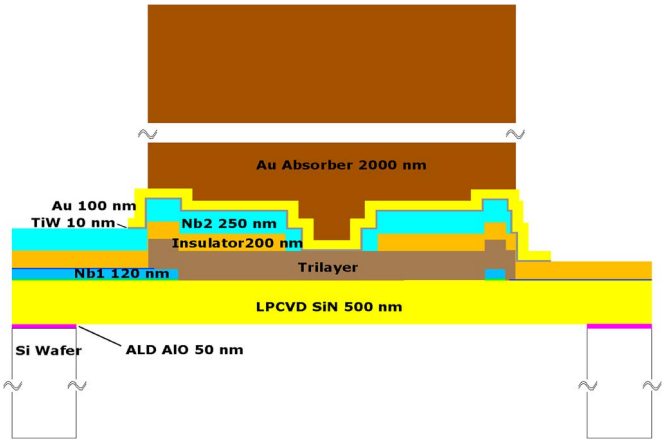

Fig. 2. Schematic cross section of a pixel where the absorber covers the whole TES area.

that we have extensive experience in modeling the physics of responsivity and noise. In particular, we have shown with previous Ti/Au Corbino devices that typically all noise can be understood based on the appropriate thermal model of the device [7]. So even if there is thermal fluctuation noise beyond the simplest one-block thermal model, we can still expect to be able to control it to some extent. Finally, the top superconducting lead acts naturally as a local magnetic shield making the Corbino geometry quite immune to externally applied magnetic fields [13]. This can be an advantage in a measurement environment, where the external magnetic field is strong, or changes temporally or spatially during a measurement.

A photograph of a final 256-pixel array chip is shown in Fig. 1(a), with an enlargement shown in Fig. 1(b). A schematic cross section is shown in Fig. 2. The TES film in each pixel is a circular Mo/TiW/Cu trilayer of diameter 380 μm, with a 2-μm-thick circular Au absorber of diameter 245 μm at the center. Each TES pixel is mounted on top of a 500-nm-thick circular SiN membrane of diameter 500 μm, and contacted at the inner and outer radii by two Nb bias leads that arrive in a microstrip geometry on top of each other, separated by an insulator layer. Several different pixel designs have also been implemented with varying inner contact radius and absorber diameter. Varying the inner contact radius is a convenient way to tune the resistance of the device [7], [13]. As these are the first Corbino arrays made, and the process is different from the ones used for previous square array and Corbino single-pixel devices, we describe the fabrication in detail below.

III. Details of the Fabrication Process

The detectors were fabricated on double-side polished (DSP) Si wafers of 380 μm thickness. Photolithography was done using standard UV-photolithography and a contact mask aligner. Eight mask layers are required to complete the lithographic processing. The processing proceeds as follows:

First a 50-nm-thick AlO_x layer was deposited by atomic layer deposition (ALD), followed by growth of 500-nm-thick low stress silicon nitride by low-pressure chemical vapor deposition (LPCVD). The AlO_x layer acts as an etch stop layer when etching through the wafer from the wafer back side.

A second, thin ALD AlO_x layer (10 nm) is deposited on top of the LPCVD SiN layer, followed by the first superconductor layer (120 nm of Nb, layer Nb1), which is deposited by sputtering. The Nb1 layer forms the lower bias leads and the outer annular contact to the trilayer. The Nb1 layer is patterned by plasma etching, and the second AlO_x acts as an etch stop. After the patterning of the Nb1 layer, the second AlO_x layer is wet etched using the Nb1 wiring as the mask. A third, 10 nm ALD AlO_x layer was then deposited and patterned. This AlO_x layer acts as an etch stop when patterning the TES trilayer, but it was removed from the areas that will be under the trilayer.

Next, the Mo/TiW/Cu trilayer was deposited by sputtering. The top Cu layer was Ion Beam Etched (IBE) and the TiW and Mo layers were RIE etched. The third ALD AlO_x mask layer was then removed by wet etching. The insulator SiO_2 layer was then deposited by PECVD, and contact openings were patterned by wet etching. Then the second Nb superconductor layer (Nb2) was sputtered and patterned. In addition to the second bias leads, this layer forms the upper contact and the shield of the trilayer. When the Nb2 layer is patterned, the areas where the absorber will contact the trilayer are also exposed.

The Au absorber was electrodeposited to a thickness of 2 μm. Here a 10/100-nm-thick TiW/Au stack served as the seed layer. The absorbers were defined by openings in thick photoresist. After electrodeposition, new photoresist was applied to protect the absorbers, and the seed layer was etched from the areas outside the absorber.

Finally, the backside processing was performed as the last step. The LPCVD SiN film on the back side was patterned using RIE, forming circular holes at each pixel. A protective photoresist was applied on wafer front side during the following backside processing. The ALD AlO_x film on the wafer back side was patterned by wet etching with the LPCVD SiN layer as mask. Then the wafer was etched through to free the membranes, using an inductively coupled plasma (ICP) etcher. The SiN layer and AlO_x layer acted as the etching mask on the back side. The AlO_x layer under the membrane acted as etch stop layer for the Si etch, and it was removed by chlorine-based ICP plasma etching to conclude the processing.

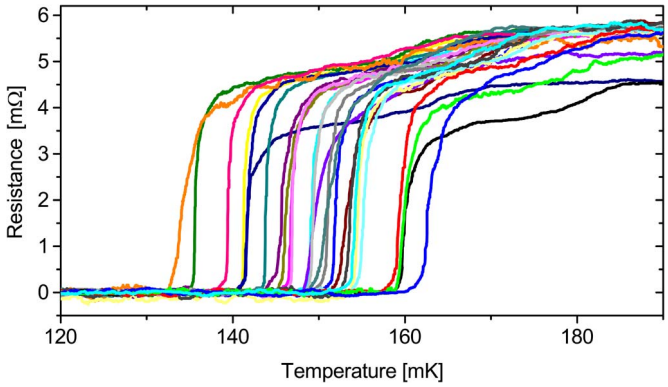

Fig. 3. Transitions measured from a single chip, all 26 pixels are Corbino devices with inner diameter 45 μm and absorber diameter 380 μm. Standard deviation for $T_{\rm C} \sim 7.5$ mK.

The purpose of the middle TiW layer in the trilayer is to act as an adhesion layer and a protective barrier against interdiffusion [15] and corrosion in the later stages of the fabrication. This layer enhances the stability of the components and, in general, enables higher processing temperatures (if needed). It can be utilized in other trilayer material combinations as well (e.g., Mo–TiW–Au).

Before final device fabrication rounds, tests were made to adjust the thicknesses of the Mo and Cu layers to obtain a critical temperature T_c of about 100 mK. In all the tests, the thicknesses of the TiW layers were kept constant at 10 nm. The final thicknesses used were 67.5 nm for the Mo layer and 220 nm for the Cu layer. However, the above thickness values are nominal as they were determined from the sputtering times. Moreover, we expect some variation across the wafer due to the nonuniformity of the sputtered films.

IV. Electrical Characterization

To study uniformity, superconducting transitions were measured from four different arrays and from two different wafers. $T_{\rm c}$ measurements were done in a four-probe lock-in measurement with a 25-μA (rms) ac current. The total variation of $T_{\rm c}$ in all the chips was between 80 and 160 mK. However, large part of that variation is from chip to chip or wafer to wafer. Within one chip, the standard deviation was typically below 10 mK. Values below a few mK are typically desired for proper multiplexing operation [2]. Fig. 3 shows all the transitions measured from a chip most extensively studied, with 26 pixels measured. The standard deviation in $T_{\rm c}$ of that dataset is 7.5 mK. No clear position dependence of $T_{\rm c}$ within a chip was observed. We see that the transitions are typically fairly sharp with widths < 2 mK, but that a curious knee structure appears above the main transition in all pixels. The origin of the knee structure is not clear presently, it has not been observed in Ti/Au Corbino devices. The normal state resistances $R_{\rm N}$ are more closely bunched around 5.5 mΩ, with a couple of outliers with slightly smaller values. These resistance values are well matched to our SQUID electronics readout. The $R_{\rm N}$ values are consistent with the separately measured trilayer film resistivities of ~ 1 $\mu\Omega$cm, which are lower than for typical Ti/Au devices ~ 3 $\mu\Omega$cm [7].

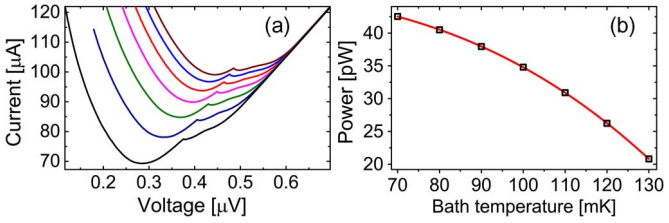

Fig. 4. (a) Set of I–V curves measured at different bath temperatures, ranging from 70 to 130 mK. (b) TES power versus bath temperature at $R/R_N = 0.75$ bias. Solid line is a fit to the equation $P = K(T_{TES}^n - T_{bath}^n)$, where n and K are sample-specific parameters. Here, $n = 3$, $K = 11$ nW/K^3.

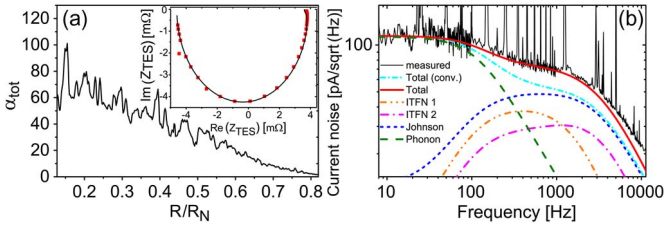

Fig. 5. (a) $\alpha_{\rm tot}$ as a function of bias, determined from the I–V curve measured at $T_{\rm bath} = 130$ mK. (Inset) The measured complex impedance at $R/R_{\rm N} = 0.5$ (points) and the best fit (line) of a complex thermal model with three blocks. (b) The corresponding noise spectrum at $R/R_{\rm N} = 0.5$ and the three block best fit (red line), with a breakdown of the different noise components. Phonon noise refers to the thermal fluctuation noise between the TES and the bath, whereas ITFN is thermal fluctuation noise internal to the TES, and Johnson refers to the nonlinear electrical noise of the TES [18]. The cyan dash-dot line (Total conv.) is the best fit using a single block model. The heat capacity and thermal conductance values in the fit were: $\rm C_{TES} = 1.2$ pJ/K, $\rm C_1 = 1$ pJ/K, $\rm C_2 = 2.1$ pJ/K and $\rm g_1 = 7$ nW/K, $\rm g_2 = 60$ nW/K, $\rm g_{bath} = 0.8$ nW/K.

A couple of pixels from the set shown in Fig. 3 were selected for more extensive electrical measurements, including current-voltage (I–V) characteristics, complex impedances [16] and noise. By measuring a set of I–V curves at different bath temperatures, one can obtain information on the exponent of thermal conduction, n, as shown in Fig. 4. For these devices we obtained a value $n = 3$.

Fig. 5(a) shows the unitless transition steepness parameter $\alpha_{\rm tot}$ [7] as a function of bias point, for a pixel with a large absorber (covering the whole area of the TES film, estimated heat capacity $\sim 2.4 \times 10^{-12}$ J/K and $T_{\rm c} = 152$ mK), measured at a bath temperature $T_{\rm bath} = 130$ mK. $\alpha_{\rm tot}$ is the logarithmic derivative of $R(T)$, and it incorporates both temperature and current dependence. The values are calculated from the I–V data. The $\alpha_{\rm tot}$ values are slightly below our intended design value $\alpha_{\rm tot} = 100$ and what we have seen before for Ti/Au Corbino devices [17]. The larger the $\alpha_{\rm tot}$, the better the energy resolution.

Fig. 5(b) shows an example of a measured noise spectrum from the same pixel, at a bias point $R/R_{\rm N} = 0.5$ and at $T_{\rm bath} = 130$ mK. The theory curves show, in addition to the simplest one heat capacity thermal model, a best fit to a model with two additional hanging heat capacities [18], which describes the noise accurately. Note that the fits were done simultaneously to the measured complex impedance, as well [inset, Fig. 4(a)]. More data are required before statements can be made about the origin of the different thermal blocks, or to see whether these devices (preferably with higher α and without absorber) have a similar phase separation as in Ti/Au devices [7].

The predicted rms energy resolution ΔE for this pixel, calculated from the noise is $\sim$9.5 eV. This particular pixel was designed for high X-ray energies having an estimated saturation energy $\sim$68 keV, predicting a high resolving power of $\sim$7 000. Also note that by choosing a pixel with a lower $T_{\rm C} \sim 100$ mK and measuring at a lower bath temperature, ΔE would go down to below 5 eV. For the smallest absorber sizes fabricated, we expect $\Delta E \sim 3$ eV. Those designs are better matched to lower energies. The effective time constant of the device was measured to be $\sim$0.9 ms (from X-ray pulse decay).

V. Conclusion

We have successfully fabricated 256-pixel X-ray Mo/TiW/Cu TES detector arrays designed for materials analysis applications, on 6-in wafer scale. Most design goals for the performance were met, namely, the critical temperature, normal state resistance, transition steepness, and the overall capability to fabricate large scale working arrays, as checked by electrical characterization of a few pixels. However, the $T_{\rm C}$ uniformity leaves some room for improvement for the future. More extensive X-ray characterization of the arrays will proceed soon.

Acknowledgment

The authors would like to thank H. Pohjonen, G. Feng, H. Heikkinen, and J. Molarius at VTT and A. Shah at Aalto University for fabrication help and R. Doriese, D. Schmidt, and J. Ullom from NIST for discussions.

References

[1] K. D. Irwin and G. C. Hilton, *Cryogenic Particle Detection*, C. Enss, Ed. Berlin, Germany: Springer-Verlag, 2005, pp. 63–149.

[2] D. A. Bennett *et al.*, "A high resolution gamma-ray spectrometer based on superconducting microcalorimeters," *Rev. Sci. Instrum.*, vol. 83, 2012, Art. ID. 093113.

[3] P. A. R. Ade *et al.*, "Detection of B-mode polarization at degree angular scales by BICEP2," *Phys. Rev. Lett.*, vol. 112, 2014, (BICEP2 Collaboration), Art. ID. 241101.

[4] M. E. Eckart *et al.*, "Kilopixel X-ray microcalorimeter arrays for astrophysics: Device performance and uniformity," *J. Low Temp. Phys.*, vol. 167, no. 5/6, pp. 732–740, Jun. 2012.

[5] J. N. Ullom *et al.*, "Transition-edge sensor microcalorimeters for X-ray beamline science," *Synchrotron Radiation News*, vol. 27, no. 4, pp. 24–27, 2014.

[6] Y. Ezoe *et al.*, "Large arrays of TES X-ray microcalorimeters for dark baryon search," in *AIP Conf. Proc.*, vol. 1185, pp. 60–63.

[7] K. M. Kinnunen, M. R. J. Palosaari, and I. J. Maasilta, "Normal metal–superconductor decoupling as a source of thermal fluctuation noise in transition-edge sensors," *J. Appl. Phys.*, vol. 112, 2012, Art. ID. 034515.

[8] K. M. Kinnunen, A. K. Nuottajärvi, J. Leppäniemi, and I. J. Maasilta, "Reducing excess noise in Au/Ti transition-edge sensors," *J. Low Temp. Phys.*, vol. 151, no. 1/2, pp. 119–124, Apr. 2008.

[9] M. R. J. Palosaari, "Transition-edge sensors for particle induced X-ray emission measurements," *J. Low Temp. Phys.*, vol. 176, pp. 285–290, 2014.

[10] J. Uhlig *et al.*, "Table-top ultrafast X-ray microcalorimeter spectrometry for molecular structure," *Phys. Rev. Lett.*, vol. 110, 2013, Art. ID. 138302.

[11] D. E. Newbury *et al.*, *Cryogenic Particle Detection*, C. Enss, Ed. Berlin, Germany: Springer-Verlag, 2005, pp. 267–312.

[12] W. B. Doriese *et al.*, "14-pixel, multiplexed array of gamma-ray microcalorimeters with 47 eV energy resolution at 103 keV," *Appl. Phys. Lett.*, vol. 90, 2007, Art. ID. 193508.

[13] A. Luukanen *et al.*, "Fluctuation-limited noise in a superconducting transition-edge sensor," *Phys. Rev. Lett.*, vol. 90, 2003, Art. ID. 238306.

[14] G. C. Hilton *et al.*, "Microfabricated transition-edge X-ray detectors," *IEEE Trans. Appl. Supercond.*, vol. 11, no. 1, pp. 739–742, Mar. 2001.

[15] S.-Q. Wang, S. Suthar, C. Hoeflich, and B. J. Burrow, "Diffusion barrier properties of TiW between Si and Cu," *J. Appl. Phys.*, vol. 73, no. 5, pp. 2301–2320, Mar. 1993.

[16] M. A. Lindeman *et al.*, "Impedance measurements and modeling of a transition-edge-sensor calorimeter," *Rev. Sci. Instrum.*, vol. 75, pp. 1283–1289, 2004.

[17] K. M. Kinnunen, "Studies of transition-edge sensor physics: Thermal models and noise," Ph.D. dissertation, Phys. Dept., Univ. Jyväskylä, Jyväskylä, Finland, 2011.

[18] I. J. Maasilta, "Complex impedance, responsivity and noise of transition-edge sensors: Analytical solutions for two- and three-block thermal models," *AIP Adv.*, vol. 2, 2012, Art. ID. 042110.

Article IV

IV

Wide-Energy-Range High-Resolution Particle Induced X-ray Emission Spectroscopy with Superconducting Microcalorimeter Arrays

M. R. J. Palosaari,[1,*] M. Käyhkö,[2] K. M. Kinnunen,[1] M. Laitinen,[2] J. Julin,[2] J. Malm,[1,2] T. Sajavaara,[2] W. B. Doriese,[3] J. Fowler,[3] C. Reintsema,[3] D. Swetz,[3] D. Schmidt,[3] J. Ullom,[3] and I. J. Maasilta[1]

[1] *University of Jyvaskyla, Nanoscience Center, Department of Physics, P. O. Box 35, FI-40014 University of Jyvaskyla, Finland*

[2] *University of Jyvaskyla, Accelerator Laboratory, Department of Physics, P. O. Box 35, FI-40014 University of Jyvaskyla, Finland*

[3] *National Institute of Standards and Technology, Boulder, Colorado 80305, USA*

(Dated: April 13, 2015)

We introduce wide energy range, energy dispersive X-ray emission spectroscopy in the particle induced mode (PIXE) using high-energy resolution superconducting cryogenic detector arrays. We demonstrate the efficiency and resolving capabilities of the instrument by spectroscopy of several complex multi-element samples in the energy range 1 - 10 keV, some of which have trace amount of impurities not detectable with standard silicon drift detectors. The ability to distinguish the chemical environment of the sample was also demonstrated with the characteristics X-rays of titanium compounds.

PACS numbers: 29.30.Kv,85.25.Oj
Keywords: Particle induced X-ray emission, PIXE, Transition-edge sensor, TES, chemical shift

I. INTRODUCTION

X-ray emission spectroscopy is an ubiquitous technique for the studies of the elemental composition of a material. Several different excitation sources, such as high-energy electrons, ions or X-rays can be used to excite inner shell transitions in materials, leading to characteristic X-ray emissions which identify the elements in the sample. The choice of the excitation source depends on many factors, with electron-beam and X-ray sources being common. Here, we focus on ion-beam excitation, or the so called Particle Induced X-ray Emission (PIXE) technique. Most often 2–3 MeV protons are used in PIXE, because they give the best X-ray yield for elements between Z = 20–40 [1]. The advantages of PIXE as compared to electron-beam excitation are: i) the accelerated particle beam in PIXE can be taken out of the vacuum to study large or delicate samples (artefacts, biological samples etc.), ii) particle beams penetrate much deeper into the bulk of the sample, whereas electron beams give information from the surface, and iii) due to the orders of magnitude heavier mass of the proton, the background *brehmsstrahlung* which can limit sensitivity, is much reduced. Compared to conventional X-ray induced fluorescence, PIXE does not suffer from the presence of characteristic peaks of the X-ray tube anode material.

In any spectroscopic experiment the ability to detect energy differences as small as possible is always thrived after, so that close lying emission lines in complex samples can be resolved. In addition, in X-ray emission measurements the energy resolution of the used detector often sets the limit on how small impurity levels can be measured, as the signal-to-background ratio improves with narrower lines. The commonly used detector in PIXE measurements is the Silicon Drift Detector (SDD), which is energy dispersive, fairly cheap, offers a high count rate beyond 100 kcps, and has a wide dynamic energy range. The energy resolution of the SDD (typically around 130 eV at 6 keV) is quite poor, and limits the detection of elements with overlapping excitations and low impurity levels. On the other hand, wavelength dispersive detectors have excellent energy resolution (around 1 eV at 6 keV) [2], but their limited energy range and small solid angle limits their use to experiments where either only a small range in energy is in interest, or where high excitation beam currents and long measurement times are possible. Here, we integrate a detector instrument into PIXE that combines the wide energy-range advantages and simplicity of the energy-dispersive detection with high energy resolution (in the best cases down to 3 eV at 6 keV [3]) and high sensitivity, by using arrays of superconducting transition-edge sensor (TES) X-ray microcalorimeters operated at 0.1 K [4]. Competitive counting rates in the kHz range are made possible by using large arrays with hundreds of individual detector elements. Similar TES arrays have also been used in table-top X-ray absorption spectroscopy experiments [5] and in synchrotron-based X-ray spectroscopy [6].

The maturation of low-temperature detector technology has enabled their use in many experiments ranging in frequency from THz bolometry [7] to γ-ray detection [8]. The detector type used here, a TES microcalorimeter, is an energy dispersive detector that is based on the sharp transition between the normal state and the superconducting state of a thin film [9]. When a photon hits an absorber material that is coupled to the superconducting thin film, the temperature of the film first quickly rises and then falls back to the steady state, causing a

* mikko.palosaari@jyu.fi

pulse-shaped change in the resistance of the device. This resistance change causes a pulse in the current, which is read out with a Superconducting QUantum Interference Device (SQUID) [9]. SQUIDs are well suited for reading out TESs thanks to their low noise, low power dissipation, and low input impedance [10, 11]. TES devices optimized for X-ray detection are relatively slow (effective time constants around 0.1 ms – 1 ms), which limits their count rate to below 10 cps, but they have high energy resolution when operated at temperatures around 0.1 K (in the best cases below 2 eV at 6 keV [12]). However, with an array of hundreds of TES detectors, the total count rate can be beyond kcps [8]. Another advantage of the array format is that the active detector area, and thus the collection efficiency, is increased to keep the irradiation times shorter, so that the possible damage to delicate samples in a PIXE measurement can be limited. The major motivation for using TES detectors are their exceptionally good energy resolution for energy dispersive detectors.

Pioneering work on using single pixel X-ray TES microcalorimeters in electron-beam induced X-ray spectroscopy of materials was performed at NIST Boulder at the turn of the millennium [13, 14], with the result that single pixel TES electron microprobe analysis is now commercially available [15]. In addition, TES measurements were recently performed with PIXE, as well [16], but only with a single pixel and with energy resolution being around 18 eV at 1.7 keV. To highlight the capabilities of our spectrometer further, we present results showing that the energy resolution is high enough to observe chemical sensitivity as shifts in the Kα peaks of Ti, while collecting data in the full energy range 1 keV–10 keV. Also, impurities with atomic concentrations in the 200 ppm level were resolvable with a measurement time of 45 min in a pigment sample. SDD based PIXE measurement could not resolve such impurities at all.

II. EXPERIMENTS

A. Detector setup

The 160 pixel TES array and the time division multiplexed SQUID read-out [11] used in the experiments were fabricated at NIST Boulder. A single TES pixel consist of about 300 nm thick superconducting Mo/Cu bilayer with a critical temperature T_C around 100 mK. 500 nm thick normal metal Cu strips were deposited on top of the bilayer to suppress local T_C variation at the edges [17] and to suppress noise [18]. The absorber, coupled directly to the superconducting film, is a $350\times350\times2.5\mu m^3$ bismuth block. Bi is used because of its advantageous combination of X-ray absorption and low heat capacity. A collimator chip with a 320 μm × 305 μm aperture size for each pixel sits on top of the array chip to prevent X-ray hits outside the absorber area.

The experiments presented in this paper were performed with a total of 60 pixels, a 65 mK bath temperature and a 2.01 MeV proton beam striking the samples in vacuum. A pulse-tube precooled cryogen-free Adiabatic Demagnetization Refrigerator (ADR) [19] was used to cool the detectors and the read-out, which are located inside a specially designed "snout" structure [3] to facilitate close proximity to the samples. The sample and the detector vacuums are separated by a AP3.3 ultra–thin polymer/Al silicon grid X-ray window from Moxtek Inc., allowing efficient X-ray transmission above 1 keV energies. In addition, to stop back-scattered protons from hitting the detector setup, an additional 125 μm thick Be foil was placed in front of the vacuum window. The snout was positioned at 90° angle with respect to the proton beam axis, and the sample surface was tilted 45° with respect to it. Thin infrared filters fabricated in-house (280 nm SiN membrane supporting a 225 nm of Al film) were used at the three shielding stages (60 K, 3 K and 50 mK) of the snout, to reduce unwanted power loading on the detectors. Further details of the measurement geometry and the setup can be found in Ref. [3], where the full-width half maximum energy resolution 3.06 eV of the best pixel in our setup is also reported. In contrast to Ref. [3], however, the distance between the detector and the samples was reduced from 30 cm to 15 cm, increasing the collection efficiency by a factor of four. Amptek X-123SDD silicon drift detector was used as a reference detector, with measurements performed in air.

B. Reference samples and efficiency calibration of the TES array

To be able to discern quantitative information on elemental concentrations, an efficiency calibration of the detector is required. Two NIST standard reference samples with known compositions, SRM 1157 (Fig. 1, stainless steel sample with seven elements V, Cr, Mn, Fe, Ni, Cu and W and SRM 611 glass sample (Fig. 2, with 61 trace elements each having nominal concentration of 500 ppm and a glass support matrix, which has a nominal composition of 72 % SiO_2, 14 % Na_2O, 12 % CaO, and 2 % Al_2O_3), were measured both with the TES-PIXE setup and with the standard PIXE with an SDD detector. The average count rate for a single TES pixel was 9.3 cps, leading to a total count rate of about 550 cps for 60 pixels, the SDD count rate was 1400 cps. The measurement times (4 h for TES, 1.13 h for SDD) were chosen such that the total number of counts was approximately the same. For the TES detector, the conversion from pulse height to energy was achieved by a spline interpolation of the known peak energies, for each pixel separately due to the intrinsic non-linearity of the TES detector. In the full energy range of 1 keV - 10 keV, the typical observed non-linearity was around 25 % at 10 keV compared to a line fitted at the lower energy range.

2). We can see from Figs. 1 and 2 the clear difference in the energy resolution between the SDD and the TES

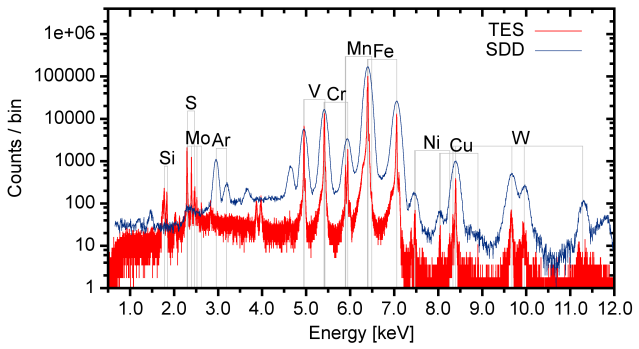

FIG. 1. SRM 1157 reference sample measured with both TES and SDD detectors. Bin width for TES was 0.5 eV and for SDD it was 7 eV. The Ar excitations from air can be seen in the SDD data around 3 keV as well as the Si escape peak from the Fe X-rays at 4.6 keV and from the Cr at 3.7 keV. In the TES data the Bi escape peaks can be seen just below 4 keV.

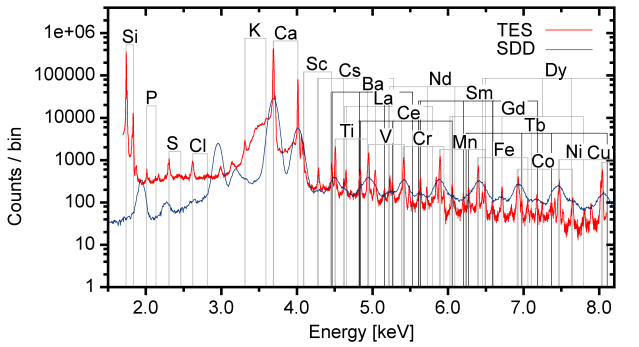

FIG. 2. SRM 611 reference sample measured with both TES and SDD detectors. Bin width for TES was 0.5 eV and for SDD it was 7 eV. The Ar excitations from air can be seen in the SDD data, as well as the Si escape peak from the Ca X-rays at 2 keV.

setup. In particular, for the more complex sample SRM 611, some of the dense peaks in the energy range 4-8 keV overlap in the SDD data, making the identification of some elements impossible or extremely challenging with SDD detectors, particularly the heavier rear earth elements (Ce, Nd, Sm, Gd, Tb, Dy) whose Lα lines are mixed in with the Kα lines of the lighter transition metals (Sc, Ti, V, Cr, Mn, Fe, Co, Ni). In contrast, all the elements in the sample are resolved with the TES detector with ease.

To determine the detector efficiency, the measured data was analyzed using the GUPIXwin program, which calculates the elemental concentrations based on the known physical parameters of the setup. In the GUPIXwin analysis, all the external filters were taken into account, but the to-be-determined intrinsic detector efficiency was temporarily set to 1. For the SRM 611 sample, the nominal matrix mass composition (72 % SiO_2, 14 % Na_2O, 12 % CaO and 2 % Al_2O_3) was used in the GUPIXwin analysis whereas for SRM 1157 sample, the matrix composition (consisting mostly of iron) was iterated by the GUPIXwin. We did not use the standard fitting procedures of the program; instead, the peak areas were integrated after the continuous background was removed by a visual fit. Then, the concentrations (without the TES efficiency) were calculated using the X-ray yields that GUPIXwin had calculated. Finally, the detector efficiency was calculated as the ratio between the measured concentration without the detector efficiency, and the known reference concentration, for all reference energies. In the analysis, statistical uncertainties and uncertainties in the ionization cross-sections for K-lines (17 %) [20] and L-lines (5%) [21] were taken into account. The reference values for the concentrations and energies of the analyzed elements were taken from Ref. [22] for SRM 611 and from the NIST certificate for the SRM 1157 sample.

Fig. 3 shows the measured efficiency data (dots), compared with the theoretical efficiency curve consisting of the known vacuum window transmission, calculated bismuth absorption for thickness 2.5 µm (using Ref. [23]). We see that the experimental values agree well with the theory, and conclude that within the accuracy of the measurement here, the calculated theoretical curve can be used to represent the efficiency of the setup. However, we do note that two observed peaks, the Al and Cu Kα peaks, had inconsistently too many events and were excluded from the analysis. In the case of Al, the extra Al emission is likely caused by fluorescence X-ray emission from the Al filters, excited by the Si Kα X-rays from the SiO_2 matrix. In the case of Cu, heavier element characteristic X-rays from the sample can give birth to Cu X-rays in the Cu layer underneath the absorber. It should be also noted that the theoretical efficiency never reaches level higher than 77 % below 10 keV energies. This is due to the fact that a thick silicon grid with 77 % hole area is under the polymer in the AP3.3 vacuum window.

C. Chemical Shifts in Ti-based Samples

Because of the excellent energy resolution of TES detectors, we expect that even chemical shifts, where the characteristic X-rays of a material is dependent on the chemical environment of a element, can be observable in our setup. The chemical state of an element (oxidation number, chemical bonding) influences its electronic transitions and atomic energy levels, even those involving the inner shells of the atoms. Different kind of effects have been observed that affect X-ray transitions: energy shifts of the characteristic X-ray lines, the alteration of X-ray relative intensity ratios and line shapes, and satellite peak formation [24]. Typically these kind of shifts can only be resolved with a wavelength dispersive and not with an energy dispersive detector, see for example

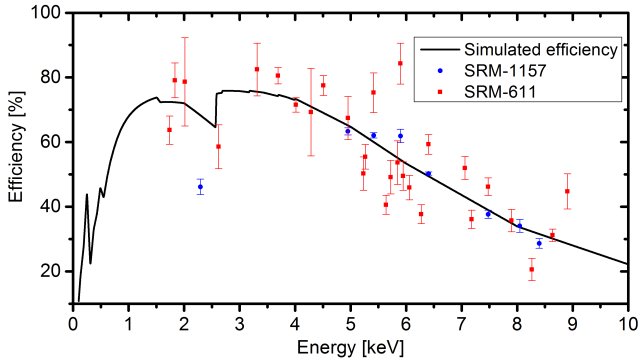

FIG. 3. The measured (dots) and simulated (line) efficiency of the TES-PIXE setup. The efficiency curve was calibrated using the known reference materials (NIST SRM 611 and NIST SRM 1157). The absorber material in our TES-detector is bismuth and the vacuum window used in front of the detector is included in the simulated efficiency. The nominal thickness of Bi absorber is 2.5 μm.

[25]. With TES detectors in the electron-probe analysis setup, evidence for Fe L-shell transition chemical shifts has been seen before [14].

We measured the X-ray spectra of three different titanium-based thin film samples (Ti (400 nm), TiN (500 nm) and TiO_2 (450 nm) all on Si substrates) with TES-PIXE, using 2 MeV proton excitation. The TiN and TiO_2 were fabricated with atomic layer deposition (ALD), the Ti film was electron-beam evaporated. The samples were measured in the order Ti–TiN–Ti–TiO_2–Ti, so that any possibility of jumps in the calibration was ruled out by comparing the Ti spectra. Any possible energy drift of a pixel was corrected on the Si Kα line, which was common in all of the samples. Each sample was measured for 1 h with an average count rate of about 8 cps per pixel. The energy calibration of the spectra was done on the Ti sample, using the Kα and Kβ peaks of Si and Ti.

Fig. 4 shows the measured Ti Kα and Kβ complexes from all the three samples. A chemical shift of 1.1 eV is seen on the Kα complex of the TiO_2 sample compared to the pure Ti sample. Also a slightly smaller shift of 1.0 eV can be seen in the Kβ. No measurable shift can be seen in the TiN spectrum. The shift was determined by fitting Gaussians to the peaks, and taking the difference between the peak centroids of the Ti and TiO_2 lines. The standard deviation of the peak position for all the lines was 0.3 eV (24 pixels in this measurement), which is well below the observed shift value, giving us confidence on the statistical significance of the result. Moreover, all the shifts had the same negative sign, strong evidence against a random process. This chemical shift result agree with X-ray photoelectron spectroscopy measurements [26] and wave dispersion spectrometer measurements [27]. Note that due to the peak fitting procedure, chemical shifts much below the FWHM energy resolution of the instrument are observable. The observed Kβ/Kα intensity ratios were (12.5 ± 0.1) % for Ti, (13.1 ± 0.2) % for TiN, and (13.31 ± 0.2) % for TiO_2. On the high energy side of the main peaks, the spectra show also smaller satellite lines, typical in PIXE measurements. The Kα satellite intensity compared to the total Ti emission was (4.9 ± 0.1) % for Ti, (5.0 ± 0.1) % for TiN and (4.8 ± 0.1) % for TiO_2. This satellite peak is most likely generated during the ion bombardment when 1s and 2p vacancies are created simultaneously. The 2p vacancy has a longer life-time than the 1s vacancy. When the inner 1s vacancy de-excites in the presence of this spectator hole, there is a change in the electrostatic potential, leading to shifts in the energy levels and thus changing the energy of the emitted photon [28].

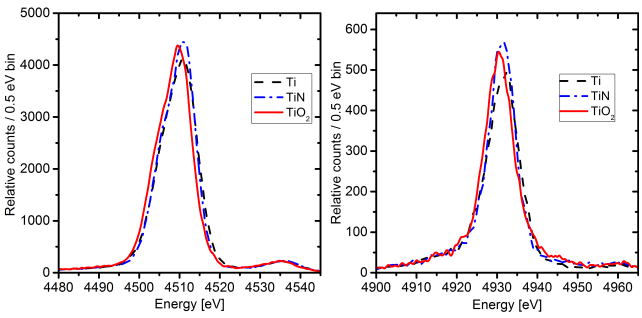

FIG. 4. Spectra from the three different Ti-compounds normalized for the Kα peak area. The spectra are divided to two plots for visual reasons. Left: The Ti K$\alpha_{1,2}$, right: The Ti K$\beta_{1,3}$. A chemical shift for the TiO_2 sample is visible.

D. Pigment measurements

As an example of a more complex real sample with trace impurities, we also studied a cobolt blue pigment sample, using both the TES and SDD detectors (Fig. 5) and a 2 MeV proton beam. The spectra were collected with a measurement time of 50 min (TES) and yy (SDD) mins. Trace impurities like Ti, and Cr are clearly observable in the TES spectrum, in contrast to the SDD spectrum. The estimate for the Ti concentration is (290 ± 60) ppm and for the Cr (110 ± 40) ppm, calculated with the efficiency curve obtained previously. This type of information can be valuable, for example, when determining the origin of a piece of art [29].

III. CONCLUSIONS

We have developed a novel and powerful X-ray spectroscopic materials analysis tool, which utilizes an array of superconducting transition-edge sensors operated at 0.1 K as the detectors, coupled with an ion beam (proton) excitation by an accelerator (TES-PIXE). The operational

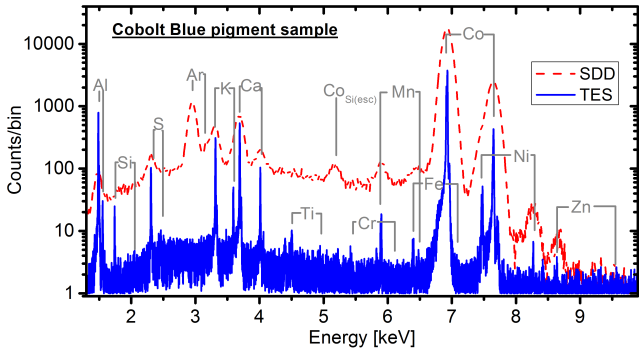

FIG. 5. PIXE spectra of a Co pigment sample using the SDD (dotted red line) and TES (solid blue line) detectors. The bin width for TES was 0.5 eV and for the SDD 7 eV. Ti, Cr, and Fe trace impurities can be resolved with the TES detectors.

capabilities of the instrument were demonstrated by measuring several complex spectra with many elements. The TES detectors clearly give a big advantage over the traditional silicon drift detectors in terms of the capabilities to identify and resolve closely lying characteristic X-ray peaks in a large energy window (1- 10 keV). Much smaller concentrations of trace impurities can be resolved, and in some cases even chemical shifts are observable (here in the Ti K-shell transitions). High energy resolution can be obtained with wavelength dispersive methods, as well, but not as efficiently and easily in a broad energy range as here. The energy dependent efficiency of the detector setup was also measured, agreeing with the calculated X-ray window attenuation and absorber stopping power.

All the measurements discussed here were performed in vacuum. In PIXE, the excitation beam can be brought to atmosphere, as well, and our cryogenic setup does allow the coupling of X-rays from air. This means that there are future prospects of studying also specimens that are large, or specimens that might not survive the vacuum with TES-PIXE. Collection efficiency will also be improved by operating the full 160 pixel array. Detector fabrication and readout electronics improvements in the future will also allow for operation of even larger arrays, possibly up to kilopixel range.

ACKNOWLEDGMENTS

This work was supported by the Finnish Funding Agency for Technology and Innovation TEKES, Academy of Finland Project no. 260880 and Academy of Finland Center of Excellence in Nuclear and Accelerator Based Physics (ref. 251353). M. Palosaari would like to thank the National Graduate School in Materials Science for funding.

[1] S. Johansson et al., *Chemical Analysis: A Series of Monographs on Analytical Chemistry and Its Applications* Wiley (1995).
[2] J. Szlachetko et al., *J. Synchrotron Rad.* **17**, 400-408 (2010).
[3] M.R.J. Palosaari et al., *J. Low. Temp.* **176**, 3-4 (2014).
[4] K. D. Irwin and G. C. Hilton, transition-edge sensors, in *Cryogenic Particle Detection*, Springer (2005), Ed. by Ch. Enss.
[5] J. Uhlig et al., *Phys. Rev. Lett.* **110**, 138302 (2013).
[6] J. N. Ullom et al., *Synchrotron Radiation News* **27**, 24, (2014).
[7] J. M. Gildemeister et al., *Appl. Phys. Lett.* **74**, 868-870 (1999).
[8] D. A. Bennett et al., *Rev. Sci. Instrum.* **83**, 093113 (2012).
[9] K. D. Irwin, *Appl. Phys. Lett.* **66**, 1998 (1995).
[10] J. Chervenak et al., *Nucl. Instr. and Meth. A* **444**, 107 (2000).
[11] W. B. Doriese et al., *Appl. Phys. Lett.* **85**, 4762 (2004).
[12] S. Bandler et al., *J. Low. Temp.* **151**, 400 (2008).
[13] D. A. Wollman et al., *J. Microsc.* **188**, 196 (1997).
[14] for a review: D. E. Newbury, K. D. Irwin, G. C. Hilton, D. A. Wollman, J. A. Small, and J. M. Martinis, Electron probe microanalysis with cryogenic detectors, in *Cryogenic Particle Detection*, Springer (2005), Ed. by Ch. Enss.
[15] Star Cryoelectronics LLC, Santa Fe, NM, USA.
[16] M.A. Reis et al., *X-ray Spectrom.* **40**, 141 (2011)
[17] G. C. Hilton et al., *IEEE Trans. Appl. Supercond.* **11**, 739-742 (2001)
[18] J. N. Ullom et al., *Appl. Phys. Lett.* **84**, 4206-4208 (2004)
[19] High Precision Devices Inc., Boulder, CO, USA.
[20] H. Paul et al. *Atomic Data and Nuclear Data Tables* **42**, 105 (1989).
[21] I. Orlic et al. *Atomic Data and Nuclear Data Tables* **56**, 159 (1994).
[22] N. J. G. Pearce et al., *Geostandards newsletter* **21**, 115133 (1996).
[23] J. H. Hubbell, and S. M. Seltzer. *Tables of x-ray mass attenuation coeffcients and mass energy- absorption coefficients (version 1.4)*, `http://physics.nist.gov/xaamdi` (2004).
[24] N. Kallithrakas-Kontos, *Spectrohim. Acta B* **51**, 1655-1659 (1996)
[25] J. Hasegawa et al., *Rev. Sci. Instrum.* **78**, 073105 (2007).
[26] S. Contarini et al. *Electr. Spectrosc. Rel. Phenom.* **125**, 2533 (2002).
[27] S. Fukushima et al. *Microchim Acta* **155**, 141 (2006).
[28] K. Jun, *Nucl. Instr. Meth. B* **75**, 3 (1993).
[29] G. Demortier, *Nucl. Instr. Meth. B* **54**, 334-345 (1991).